DISSERTATION

ANALYSIS OF CONVECTION AND PRECIPITATION IN THE WEST PACIFIC DURING THE PISTON FIELD CAMPAIGN

Submitted by

Kyle Chudler

Department of Atmospheric Science

In partial fulfillment of the requirements

For the Degree of Doctor of Philosophy

Colorado State University

Fort Collins, Colorado

Spring 2022

Doctoral Committee:

Advisor: Steven Rutledge

Michael Bell
Eric Maloney
Steven Reising

ABSTRACT

ANALYSIS OF PRECIPITATION AND CONVECTION IN THE WEST PACIFIC DURING THE PISTON FIELD CAMPAIGN

Tropical convection is a meteorological phenomenon with important impacts on the atmosphere, both locally and globally. Consequently, it has been an intensely studied topic for many years. Importantly, several ship-based field campaigns have taken place over tropical oceans. Such field campaigns are vital to the advancement of knowledge in this field, as meteorological observations over these open oceans are otherwise scant or non-existent. The latest project to examine tropical convection is the Propagation of Intraseasonal Oscillations (PISTON) field campaign, which took place in the western North Pacific in the late-summer and early-fall of 2018 and 2019. On board the PISTON ships was the SEA-POL weather radar, the first polarimetric weather radar designed specifically for deployment at sea. In addition to taking traditional radar measurements of precipitation intensity and velocity, SEA-POL's polarimetric measurements also provide insights into the size, shape, and composition of hydrometeors within precipitating systems. By combining SEA-POL's unique measurements with other meteorological datasets, this work presented in this dissertation provides new insights in tropical convection in the Pacific warm pool.

Chapter 2 of this dissertation provides an overview of the variability in convection observed during the PISTON cruises, and relates this variability to large-scale atmospheric conditions. Using an objective classification algorithm, precipitation features are identified and

labeled by their size (isolated, sub-MCS, MCS) and degree of convective organization (nonlinear, linear). It is shown that although large mesoscale convective systems (MCSs) occurred infrequently (present in 13% of radar scans), they contributed a disproportionately large portion (56%) of the total rain volume. Conversely, small isolated features were present in 91% of scans, yet these features contributed just 11% of the total rain volume, with the bulk of the rainfall owing to warm rain production. Convective rain rates and 30-dBZ echo-top heights increased with feature size and degree of organization. MCSs occurred more frequently in periods of low-level southwesterly winds, and when low-level wind shear was enhanced. By compositing radar and sounding data by phases of easterly waves (of which there were several in 2018), troughs are shown to be associated with increased precipitation and a higher relative frequency of MCS feature occurrence, while ridges are shown to be associated with decreased precipitation and a higher relative frequency of isolated convective features.

During PISTON, SEA-POL routinely measured extreme values of differential reflectivity in the cores of small, isolated convection, owing to the presence of large drops. Chapter 3 examines the structure and frequency of cells containing large drops. Cells with high differential reflectivity (> 3.5 dB) were present in 24% of all radar scans. The cells were typically small (8 km2 mean area), short lived (usually < 10 minutes), and shallow (3.7 km mean height). High differential reflectivity was more often found on the upwind side of these cells, suggesting a size sorting mechanism which establishes a low concentration of large drops on the upwind side. Differential reflectivity also tended to increase at lower altitudes, which is hypothesized to be due to continued drop growth, increasing temperature (dielectric effect), and evaporation of smaller drops. Rapid vertical cross section radar scans, as well as transects made by a Learjet aircraft with on-board particle probes, are also used to analyze these cells, and support the conclusions drawn from statistical analysis.

In Chapter 4, the observations of precipitation from spaceborne Ku-Band precipitation radar (KuPR) from the Global Precipitation Mission Dual-Frequency Precipitation Radar is compared surface observations from SEA-POL. Over the 18 instances where KuPR and SEA-POL made concurrent measurements of precipitation, the average rain rate in KuPR was 50% lower than in SEA-POL, but the raining area was 113% higher. The net effect of these two differences of opposite sign was for KUPR to have 23% more rain volume than SEA-POL. The limited resolution of KuPR (5x5 km) causes it to underestimate rain rate in small convective cores, but also over-broaden raining features beyond their true extent. It is also shown that KuPR tends to slightly overestimate rain rate below the melting layer in stratiform rain, likely due to overcorrection of attenuation below radar bright bands. Using a statistical model to simulate KuPR rain volume, it was found that KuPR would theoretically overestimate rain volume during trough phases of the easterly waves observed during PISTON (when there was more precipitating area), and underestimate rainfall during ridge phases (when there was less precipitating area).

TABLE OF CONTENTS

Chapter 1: Introduction

Tropical convection and precipitation are of critical importance to atmospheric processes both locally and globally. Columns of upward motion in convection serve as a primary mode of vertical transport of heat and momentum and alter moisture contents throughout the troposphere. The latent heating/cooling associated with the phase change of water is important in governing vertical heating profiles. Broad regions of convectively modified air can drive larger circulations which impact global heat and moisture transport. Thus, it is crucially important to accurately represent tropical precipitation in weather forecast models, and must be rigorously studied to better understand both the internal processes which control convective storms, as well as their broader impacts on the atmosphere. This dissertation will seek to build upon extensive existing research in the field by offering new insights into tropical convection using unique data collected from a state-of-the-art weather radar in an important and understudied geographic region over the western North Pacific Ocean waters.

1.1 History of Tropical Precipitation Research

For decades, tropical convection has been a source of meteorological intrigue and the topic of countless studies. To contextualize the work presented later in this dissertation, a brief review of the history of tropical convection research is presented here. Using only data from radiosondes and surface weather stations, energy budget analysis, and simple models, early studies were able to correctly hypothesize that tropical convection played an important role in global heat transport and moisture budgets (Riehl 1950; Braham 1952; Riehl and Malkus 1958). The advent of weather satellites in the 1960s, which offered unprecedented views of global convection, ushered in a new era of tropical research and allowed researchers to track the evolution of synoptic-scale systems over time, assess how patterns of cloud coverage and precipitation varied over a given region, and relate satellite pictures to ground observations (e.g., Frank 1970; Martin and Suomi 1972; Reed and Recker 1971; Grey 1973). Tropical convection research was advanced even further with the development of weather radars, which allowed for detailed observations of individual thunderstorms at high spatial and temporal resolution (e.g., Houze and Cheng 1977; Zipser et al. 1977). The introduction of spaceborne weather radars (Simpson et al. 1996; Hou et al 2014), which combined the coverage area of satellites with the detailed precipitation measurements of surface radars, allowed for even more in-depth studies of tropical convection.

As instruments became more sophisticated, so too did our understanding of tropical convection and its impacts on a more granular level. The structure, height, and organization of individual precipitating systems was found to impact vertical heating/cooling profiles (Cifelli and Rutledge 1998, Schumacher et al. 2007), as well as transport of momentum through the troposphere (LeMone 1983, LeMone et al. 1984). At the surface, convection was found to substantially influence sensible and latent heat fluxes, both by creating pockets of evaporatively-cooled air over relatively a warm sea surface (i.e., “cold pools”, Gaynor and Ropelewski 1979, Jabouille et al. 1996, Saxen and Rutledge 1998), and by forming thin stable “lenses” of buoyant freshwater deposited from precipitation, which have their own impacts on sea surface temperature (Katsaros and Buettner 1969, Clayson and Bogdanoff 2013, Drushka et al. 2016; Thompson et al. 2019).

1.1.1 PREVIOUS FIELD CAMPAIGNS AND SEAFERING RADARS

To study tropical convection, numerous field campaigns have been conducted in various locations across the globe. The projects often utilize weather radars which have been specially designed for deployment at sea. These radars provide high-resolution 3D measurements of precipitating systems. In 1974, the Global Atmospheric Research Program Atlantic Tropical Experiment (GATE) utilized C-Band radars, which could only measure reflectivity and were not stabilized for ship motion, to obtain some of the first in-situ measurements of tropical squall lines over the open ocean (Houze 1977; Houze and Cheng 1977; Houze and Betts 1981). In the 1992 Tropical Ocean and Global Atmosphere Coupled Ocean–Atmosphere Response Experiment (TOGA COARE, Webster and Lukas 1992), auto-stabilizing radars built specifically for ship-deployment (Petersen et al. 1999) were used to study convection in the West Pacific warm pool (i.e., Szoke et al. 1986, Rickenbach and Rutledge 1998; DeMott and Rutledge 1998). Other field campaigns which utilized C-Band weather radars include the Summer Monsoon Experiment (SMONEX, Krishnamurti 1985), South China Sea Monsoon Experiment (SCSMEX, Lau et al. 2005), Kwajalein Experiment (KWAJEX; Yuter et al. 2005), Joint Air–Sea Monsoon Interaction Experiment (JASMINE, Webster et al. 2002), East Pacific Investigation of Climate Processes in the Coupled Ocean–Atmosphere System (EPIC, Petersen et al. 2003), and Dynamics of the Madden–Julian Oscillation (DYNAMO, Yoneyama et al. 2013).

The next major advancement in seafaring radars was ushered in with the Colorado State University SEA-POL weather radar, which is the primary tool used in this study. In addition to providing traditional radar measurements of precipitation intensity and radial velocity, SEA-POL is the first seafaring radar capable of measuring a full suite of polarimetric variables. These polarimetric variables not only allow for insights into the microphysical properties of storms (i.e., hydrometeor size, shape, orientation, and distribution) but also allow more accurate estimations of rain rate (Thompson et al. 2018). More information on SEA-POL can be found in Rutledge et al. (2019a,b).

1.2 The PISTON Field Campaign

During the late-summer and early-fall of 2018 and 2019, the legacy of previous tropical, ship-based field campaigns was built upon with the Propagation of Intraseasonal Oscillations (PISTON) field campaign (Sobel et al. 2020, Chudler et al. 2021). Originally, this project was designed to take place in the South China Sea off the west coast of the Philippines, where the two-way interaction between large-scale oscillations and localized thunderstorms and orography would be studied. However, a denial of an international Marine Science Research agreement required that PISTON relocate to international waters east of the Philippines in the western North Pacific. In addition to this unexpected logistical challenge, the large-scale oscillation which PISTON was seeking to study [the Boreal Summer Intraseasonal Oscillation (Wang and Xie 1997; Lee et al. 2013)], was almost entirely inactive for the duration of both the 2018 and 2019 cruises. While large-scale oscillations were largely absent, a wide variety of weather conditions were still observed, from calm seas and fair-weather cumulus to intense precipitation in the outer bands of typhoons

Despite the setbacks, a fantastic dataset of measurements of tropical weather was still collected. As mentioned above, the SEA-POL radar is the first polarimetric radar designed for ship deployment, and took 3D measurements of precipitation within 120 km of the ship every 10-15 minutes for the duration of both cruises (with the exception of a few short periods where the radar was shut down for maintenance). In addition to the SEA-POL radar, a variety of other meteorological and oceanographic instrumentation was also present on the PISTON ships. A very successful radiosonde operation launched weather balloons every 3 hours, capturing high-resolution vertical profiles of temperature, relative humidity, and wind speed, as well as derived quantities such as convective instability, precipitable water, and lifted condensation level. Out of the 535 balloons launched over the duration of both cruises, only 7 failed to reach the tropopause. Additionally, other instruments on the ship made high-quality measurements of air temperature, dew point temperature, wind speed, sea surface salinity, sea surface temperature, solar radiation, and other air/ocean parameters. With these observations, energy flux measurements were calculated by the National Oceanic and Atmospheric Administration Earth System Research Lab Physical Sciences Division (Fairall et al. 1996; Fairall et al. 2003; Edson et al. 2013), providing a timeseries of sensible and latent heat exchanges between the air and ocean surface.

The uniqueness of the PISTON dataset is two-fold, both in SEA-POL's polarimetric capabilities and in the location of the project itself. Out of the campaigns listed above, only TOGA-COARE and KWAJEX were conducted in the western North Pacific, and both of these projects generally operated outside of PISTON study region (~125-138 °E, 8-22 °N). Despite the dearth of field projects in the region, the western North Pacific "warm pool" is greatly important to the global weather system. Here, broad areas of deep convection release immense amounts of latent heat and dramatically alter moisture budgets. The Asian summer monsoon brings copious amounts of moisture via strong low-level westerly winds, which interact with westward moving easterly waves (Reed and Recker 1971) and frequent tropical cyclones (Ramsay 2017). Variability of convection in the region has been shown to influence mid-latitude weather (Moon et al. 2013; Jenney et al. 2021), as well as impact global tropical cyclone activity (Kikuchi and Wang 2010). Understanding the processes which control variability in precipitation and convection in the region is thus fundamentally important, and makes the PISTON dataset a rich one to investigate.

1.3 Overview of Dissertation

From early hypothesis of "hot towers" in the equatorial zone transporting heat into the upper troposphere (Riehl and Malkus 1958), to modern spaceborne radars which make 3D measurements of global precipitation from hundreds of miles away, research on tropical thunderstorms has advanced tremendously in the past 70 years. The PISTON field campaign, which studied convection in the western North Pacific with a state-of-the-art weather radar, is the next chapter in a long list of successful field campaigns. Using the SEA-POL radar dataset, along with other data collected during PISTON, this dissertation will provide novel insights into tropical convection and how it is measured. Specifically, this work is composed of three research chapters, each of which examine a unique topic:

- Chapter 2: Using atmospheric sounding and reanalysis data, the relationship between large-scale synoptic patterns and convection and precipitation observed by SEA-POL is examined. This work also introduces an automated objective precipitation feature detection algorithm, which is used in subsequent chapters. This work is published in *Journal of Climate* (Chudler and Rutledge 2021).
- Chapter 3: During PISTON, it was noted that SEA-POL measured very high values of differential reflectivity within the cores of shallow convection. This is indicative of very large raindrops, which is a feature not typically seen in shallow, warm rain.

This chapter examines the frequency and 3D structure of these cells, as well as their microphysical aspects. This work has been submitted for review to *Monthly Weather Review*.

- Chapter 4: While satellite radars are an extremely useful tool for measuring global precipitation, their limited horizontal resolution results in precipitation measurements which differ from those of SEA-POL. In this chapter, observations of precipitation are compared and contrasted between the spaceborne Global Precipitation Mission Dual-frequency Precipitation Radar (Hou et al. 2014) and SEA-POL

Chapter 2: The Coupling Between Convective Variability and Large-scale Flow Patterns Observed During PISTON 2018-2019[1]

2.1 Introduction and Background

2.1.1 THE PISTON FIELD CAMPAIGN

Convection and precipitating cumulus in the tropics are of fundamental importance to the atmospheric system, with impacts spanning local to global scales. The structure of precipitating systems is known to directly influence the vertical distribution of latent heating (Houze 1997; Cifelli and Rutledge 1998; Schumacher et al. 2007), and the organization of mesoscale convective systems (MCS's) has been shown to impact momentum transport through the troposphere (LeMone 1983; LeMone et al. 1984). During boreal summer, the western North Pacific "warm pool" region is characterized by frequent deep convection. This region is influenced by the low-level westerlies and moisture associated with the Asian Summer Monsoon (itself a major component of the global weather system), as well as numerous westward moving disturbances in the form of easterly waves (Reed and Recker 1971) and tropical cyclones (Ramsay 2017). Also, an important phenomenon in this region is the Boreal Summer Intraseasonal Oscillation (BSISO; Wang and Xie 1997; Lee et al. 2013), marked by an envelope of pronounced convection which propagates from the Indian Ocean northeastward into the western North Pacific. The BSISO has important teleconnections to other areas in the tropics and extratropics

[1]This chapter is a slightly modified version of the work published in *Journal of Climate* as: Chudler, K., and S. A. Rutledge, 2021: The Coupling Between Convective Variability and Large-scale Flow Patterns Observed PISTON 2018-2019. Journal of Climate, 1–57, https://doi.org/10/gnc2js.

(Moon et al. 2013; Lee et al. 2017). For these reasons, the western North Pacific is an enticing region to study.

During the late-summer and early-fall of 2018 and 2019, the Propagation of Intraseasonal Oscillations (PISTON) field campaign took place in western North Pacific Ocean on board the R/V *Thomas G. Thompson* (2018, hereafter referred to as *TGT*) and R/V *Sally Ride* (2019, hereafter referred to as *SR*) (Figure 2.1). PISTON originally targeted the South China Sea near the west coast of the Philippines, but refusal of an international marine research agreement forced PISTON to relocate to international waters east of the Philippines. Although no well-defined BSISO oscillation materialized over the course of 69 operational days at sea (20 Aug – 8 Sept, 14 Sept – 12 Oct 2018; 5 - 24 Sept 2019), a wide variety of interesting weather conditions were observed.

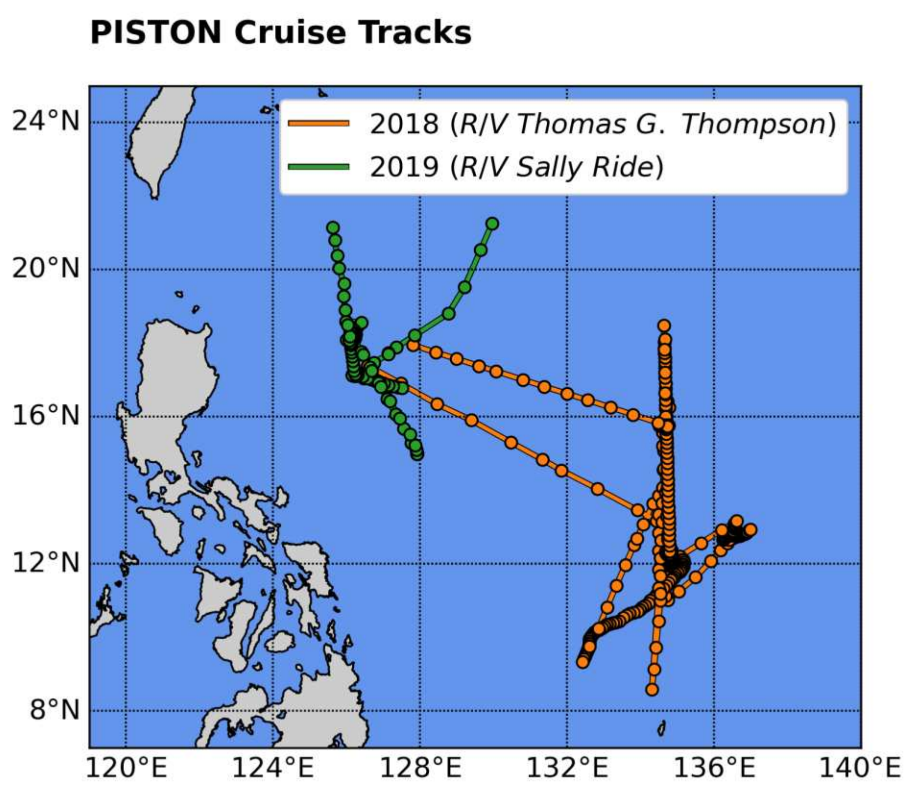

Figure 2.1: Ship tracks for the 2018 (20 Aug – 8 Sept, 14 Sept – 12 Oct 2018) and 2019 (5 - 24 Sept 2019) PISTON cruises. Outlined circles mark the location of radiosonde launches.

Conditions at the ship varied from fair-weather cumulus and calm seas to intense precipitation and disturbed sea states, the latter situation associated with mesoscale convective systems (MCS's) and the outer rainbands of typhoons overrunning the ship locations. An overview of the large-scale conditions encountered during the 2018 cruise is covered in Sobel et al. (2020).

On board the ships were a suite of scientific instruments, acquiring measurements of the ocean and atmosphere. A key instrument was the Colorado State University SEA-POL radar, a C-Band polarimetric Doppler radar designed for deployment at sea (Rutledge et al. 2019a,b). In addition to providing traditional radar measurements of precipitation intensity and radial velocity, SEA-POL measured a suite of polarimetric variables. The polarimetric variables not only allow for insights into the microphysical properties of storms, but also enable more accurate measurements of rain rate (Thompson et al. 2018). Detailed information on SEA-POL, as well some results from its first deployment at sea (SPURS-2017), can be found in Rutledge et al. (2019a,b).

2.1.2 CONVECTIVE MORPHOLOGY

The structure and morphology of precipitating systems in the tropics have important implications on the vertical distributions of heating and momentum transport. Convection in the tropics crosses a wide spectrum of sizes and organizations, from shallow, isolated cells a few kilometers in width (characterized by warm rain processes; Schumacher and Houze 2003), to MCS's hundreds of kilometers wide with organized lines of deep convection and broad areas of stratiform rain (Houze 2014). These systems drive unique latent heating profiles, with shallow convection warming the lower troposphere, deep convection warming the entire troposphere with a peak in the mid-levels, and stratiform precipitation warming the upper troposphere while cooling the lower levels (Houze 1989, Schumacher et al. 2007, Tao et al. 2010). Accurate representation of these latent heating profiles in large scale models has been shown to increase agreement with observations, through generation of a more accurate Walker Circulation (Hartmann et al. 1984). With respect to momentum transport, MCSs with linearly organized convective features tend to add momentum in the upper (lower) levels against (along) the direction of propagation (LeMone 1983, LeMone et al. 1984). By characterizing the modes of convection observed during PISTON, this study aims to provide insight which could be used to improve the representation of latent heating and momentum transport in the western North Pacific.

To begin characterizing convective modes, it is desirable to partition radar-observed precipitation into specific categories dictated by their morphology. Rickenbach and Rutledge (1998) manually classified TOGA COARE radar scans into categories by area (MCS and sub-MCS) and organization (linear and nonlinear). Xu and Rutledge (2015) (hereafter referred to as XR15) improved upon this methodology by developing an automated objective feature classification algorithm which assigned different morphology classifications to each feature within a radar scan, rather than classifying an entire scan under one group, as was done in the manual classification scheme used by Rickenbach and Rutledge (1998). The present study, as discussed in Section 2.2.2, incrementally improves the feature identification algorithm by modifying the criteria used for linear/nonlinear classification, as well as introducing an “isolated” classification for small convective features.

2.1.3 EASTERLY WAVES

Easterly waves are a leading mode of convective variability in the tropics (Chang 1970; Burpee 1972; Lau and Lau 1990). Easterly waves are often the precursors of tropical cyclones (Avila and Pasch 1992; Molinari et al. 1997; Dunkerton et al. 2009) and are in fact occasionally referred to in the literature as “tropical depression-type” disturbances. In the western North Pacific, easterly waves form from mixed Rossby-gravity waves, which originate along the equator and turn northward as they interact with the confluence zone along the monsoon trough (Dickinson and Molinari 2002, Maloney and Dickenson 2003).

As these waves primarily exist over the open ocean, in situ observations of easterly waves have been sparse, particularly over the West Pacific. Previous studies have relied primarily on satellite (e.g. Kiladis et al. 2006), sounding, or modelling (e.g. Donner et al. 1999) data to describe the 3D variability of convection across easterly waves. Easterly waves were not a focus of study during TOGA COARE (Godfrey et al. 1998) and studies of easterly wave passages during KWAJEX (Sobel et al. 2004, Schumacher et al. 2007, Wang and Zhang 2015) did not examine the vertical structure of convection associated with these waves. Petersen et al. (2003; hereafter defined as P03) used data from the C-band Doppler radar on board the R/V *Ronald H. Brown* to characterize the nature of convection and its vertical structure in different phases of the easterly waves observed during EPIC. However, EPIC took place in the East Pacific, where the source of easterly waves is different – as East Pacific easterly waves are tied to African easterly waves which re-intensify over central America (Serra et al. 2008, Whitaker et al. 2020) while the source of West Pacific easterly waves is less understood, possibly arising due to wave accumulation (a process whereby a zone of confluence, such as that in the West Pacific where trade easterlies meet monsoon westerlies, enhances wave activity, see Maloney and Dickinson 2003; Serra et al. 2008). Fortunately, during PISTON 2018, several easterly waves passed over the ship (Sobel et. al 2020). Using the method outlined in P03 (described in detail in Section 2.2.4) this study identifies easterly wave periods and analyzes the variability in atmospheric conditions and convective morphology across each wave phase.

Overall, the purpose of this study is to provide an overview of precipitation observed by SEA-POL, and to relate the variability in convection to the synoptic patterns documented during each PISTON cruise. Although the SEA-POL radar can only observe precipitation over a relatively small area, broader-scale implications can be inferred by relating this convection and its associated impact on the atmosphere to the synoptic patterns it occurred in. Although this study does not directly address the impact of West Pacific convection on the climate, it does provide a foundation for future work to build upon by linking convective morphologies to different synoptic regimes. An overview of data sources and analysis methods is given in Section 2.2. A brief summary of the large-scale conditions and significant weather events is given in Section 2.3.1. Statistics of precipitation feature morphologies and the conditions they occurred in is given in Section 2.3.2. An analysis of the easterly waves observed during 2018 is given in Section 2.3.4 and Section 2.4 summarizes the main findings and conclusions.

2.2 Data and Methodology

2.2.1 SEA-POL RADAR

During the 69 operational days of PISTON over both phases, the SEA-POL radar operated nearly continuously, with only a handful of short (2-3 hour) shut-downs needed for maintenance or due to very rough seas (the longest outage was on 24 September 2019, when SEA-POL was shut down for 24 hours for repairs). In the 2018 operations, SEA-POL obtained 360° plan position indicator (PPI) volume scans every 15 minutes, reducing to a 10-minute interval in 2019. Multiple elevation sweeps were done in each volume scan, with the exact angles depending on the type and location of echoes present. In general, scanning strategies were chosen which captured the vertical extent of echoes. For example, higher elevation angles were used when storms were closer to the ship. These scanning strategies were designed and programed prior to start of the field campaign. To avoid illuminating the ship's bridge area, a 115° (80°) sector to the aft of SEA-POL was blanked in 2018 (2019; the reason the sector size was smaller in 2019 was due to the smaller ship, *SR*, compared to the *TGT* used in 2018). Nearly 7000 volume scans were collected. Range-height indicator (RHI) scans were also performed both in both phases, however these scans are not examined in the present study. More detail on SEA-POL and its technical specifications can be found in Rutledge et al. (2019a,b).

The SEA-POL dataset was rigorously quality controlled by the CSU Radar Meteorology team prior to analysis. First, non-meteorological echoes such as sea clutter, side-lobe clutter, second-trip echoes, and other artifacts were removed. Specific differential phase (K_{DP}) calculation and attenuation correction of reflectivity (Z) and differential reflectivity (Z_{DR}) was then performed based on the process outlined in Wang and Chandrasekar (2009). Using the National Center for Atmospheric Research (NCAR) RadX software package (https://www.eol.ucar.edu/software/radx), radar data was then interpolated on to a 300x300 km cartesian grid with 15 vertical levels, with grid spacings of 1km in the horizontal and 0.5 km in the vertical. Radar data were then partitioned into convective and stratiform pixels using the method of Steiner et al. (1995).

Finally, rain rate was calculated at each grid point using Z, Z_{DR}, and K_{DP}, based on the method outlined in Thompson et al. (2018).

2.2.2 PRECIPITATION FEATURES

An improved precipitation feature identification and classification algorithm, based on the method outlined in XR15, is utilized in this study. First, using the gridded radar dataset, precipitation features were identified in each scan by grouping adjacent pixels exceeding a reflectivity threshold (17 dBZ) at a given level (2km). This threshold was chosen in XR15 to match the minimum detectable reflectivity of the NASA TRMM satellite-based radar which was also being used in that study. Although TRMM data is not used in the current work, the 17 dBZ threshold was found to capture the majority of features and was therefore retained to facilitate comparisons with the results of XR15. After grouping, the radar echo of each feature was then fit with an ellipse, based on the mass distribution tensor eigenvalues of the raining points (Medioni et al. 2000, Nesbitt et al. 2006). In the event that a feature contained multiple distinct convective elements (as detected by the Steiner et al. 1995 algorithm), each of these convective "sub-features" was fitted with its own ellipse. This differs from the work of XR15, where convective ellipses were computed to encompass *all* convective points within a feature, regardless of whether these points were connected or not. Fitting separate ellipses to each distinct convective element allows for more accurate classification of the linearity of the convection. For each feature, statistics such as area, mean rain rate, and echo top height were then calculated.

Once features were identified, a decision tree (Figure 2.2) was used to classify features by their morphology. As in XR15, features were labeled as "sub-MCS" or "MCS" based on their overall size. This study also adds the additional size category of "isolated" for features with a

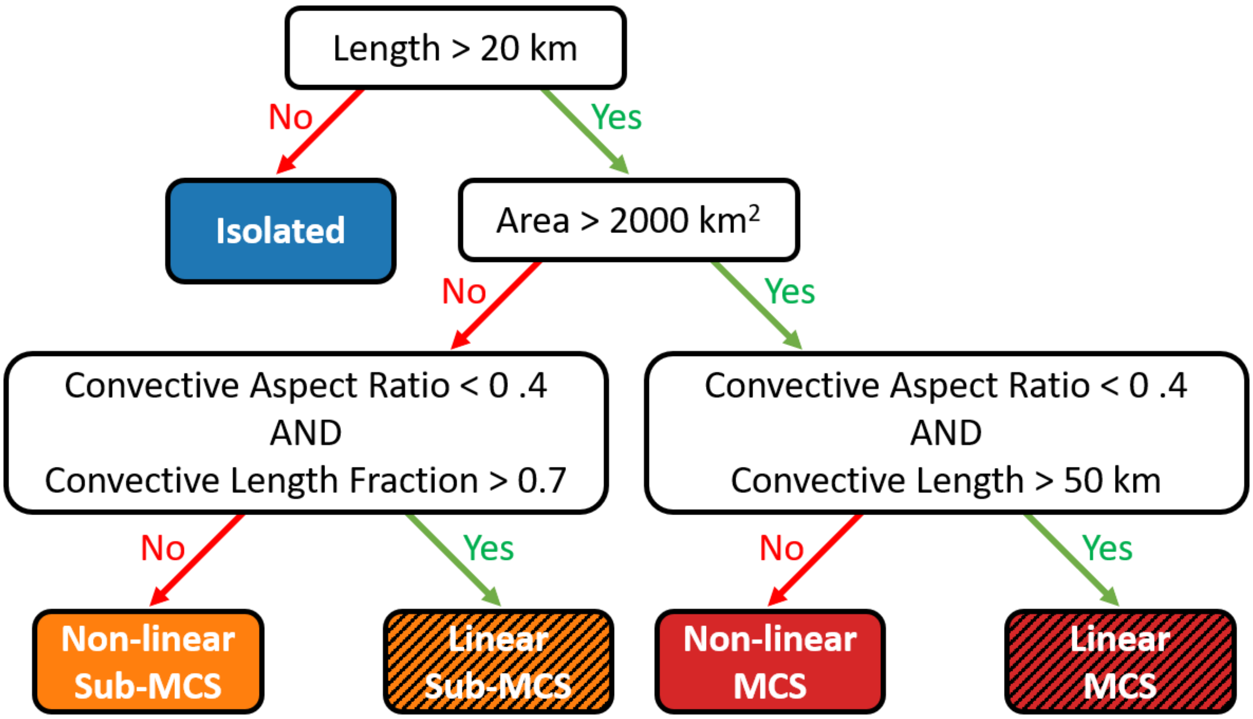

Figure 2.2: Decision tree for precipitation feature classification. Convective aspect ratios and lengths are determined by the largest convective feature within the encompassing feature. Convective length fraction is defined as the length of the largest convective feature divided by the length of the whole feature.

maximum horizontal dimension of less than 20km. Sub-MCS and MCS features were then classified further as “nonlinear” or “linear” based on the length and aspect ratio of the largest convective sub-feature contained within the broader echo pattern. Examples of the different types of precipitation features are provided in Figure 2.3. For both sub-MCS and MCS features, the aspect ratio of the largest convective feature was required to be less than 0.4 to be classified as linear. Furthermore, for the sub-MCS classification, the largest convective feature also needed to be at least 70% the length of the encompassing main feature. For the linear MCS classification, the largest feature required a length exceeding 50km. If the largest convective feature within a sub-MCS or MCS did not meet both criteria, the feature was classified as nonlinear. The linearity of isolated features, which are typically short-lived and unorganized, was not considered. The

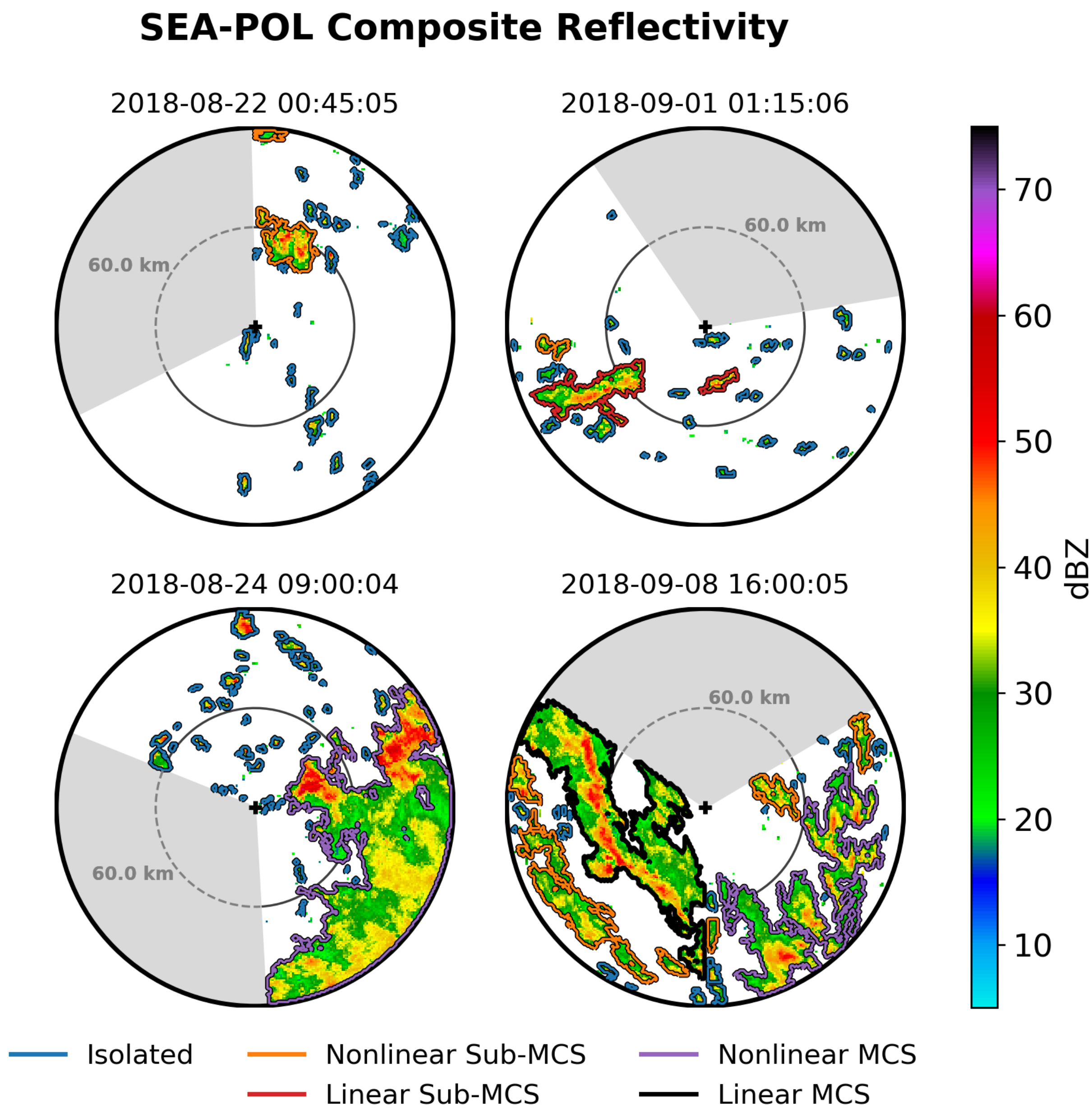

Figure 2.3: SEA-POL composite reflectivity images showcasing examples of the different types of precipitation features used in this study. Each feature is outlined with a color corresponding to its feature type, as provided in the legend on the bottom. The grey wedge indicates the portion of SEA-POL's scope which was blanked in order to avoid radiating the ship's bridge.

specific thresholds and parameters in the classification decision tree were tuned based on a manual, subjective analysis of the algorithm's performance. Sensitivity tests show that, although the specific values of the results presented hereafter do change slightly based on the thresholds and parameters used in classification, the changes are not dramatic and, more importantly, the relative relationship between different morphologies remains the same.

2.2.3 ATMOSPHERIC SOUNDINGS

Vaisala RS41-SGP radiosondes were launched from the *TGT* and *SR* every three hours during operational periods of PISTON, making measurements of atmospheric temperature, relative humidity, pressure, and wind speed with a measurement frequency of 1 Hz. Sounding data was then quality controlled as outlined in Ciesielski et al. (2014) and interpolated to 5 hPa intervals. The PISTON sounding operations were overall very successful, with 535 successful launches (375 in 2018, 160 in 2019). Only a few launches failed to reach the tropopause (balloons launched into moderate or heavy rain would occasionally get stuck/pop around the melting layer, likely due to ice accretion).

2.2.4 EASTERLY WAVE DETECTION

Following methodology of previous studies (e.g. Reed and Recker 1971; Burpee 1974; Burpee 1975; Thompson et al. 1979; P03), 700 hPa meridional wind (*v*) speed/direction was used to diagnose easterly wave phases in the PISTON 2018 sounding data. No easterly waves were observed in 2019 (the weather was primarily influenced by a monsoon depression; see Section 2.3.1.2, therefore the 2019 dataset is excluded from the easterly wave analysis. In order to isolate the easterly wave signal, a Butterworth bandpass filter was applied to the 5 hPa-interpolated sounding data to emphasize signals with periods of 3-7 days. Based on the magnitude/sign of *v,* each sounding profile was then defined as being in one of four wave phases: ridge, northerly, trough, or southerly. Ridges and troughs were defined as times when the magnitude of *v* was less than 2 m s^{-1}, with ridges being in a transition from northerly to southerly wind, and vice versa for troughs. Periods when v was less than -2 m s^{-1} were labeled as northerly, and periods when v was greater than 2 m s^{-1} were labeled as southerly. Put more succinctly:

- Ridge: transition from southerly to northerly, $|v| < 2$ m s^{-1}
- Northerly: $v < -2$ m s^{-1}
- Trough: transition from northerly to southerly, $|v| < 2$ m s^{-1}
- Southerly: $v > 2$ m s^{-1}

As this method only looks at the local meridional wind direction without context of the larger environment it was occurring in, a baseline assumption is that variation in the meridional wind is primarily due to easterly wave activity. This was largely true for the 2018 cruise (Sobel et al. 2020), with the notable exception of when tropical cyclones passed near the ship. Periods which were significantly impacted by typhoon activity (i.e. when in the "monsoon tail" of Jebi, see Sobel et al. 2020), were subjectively identified and removed.

2.2.5 OTHER DATA SOURCES

Tropical cyclone track and intensity data were obtained from the IBTrACS database (Knapp et al. 2010, Knapp et al. 2018). Gridded reanalysis of meteorological fields was obtained from the fifth-generation European Centre for Medium-Range Weather Forecasts Reanalysis product (ERA5, Hersbach et al. 2020). Gridded global precipitation estimates from the Integrated Multi-satellite Retrievals for GPM (IMERG) Version 6 dataset (Tan et al. 2019) are also used in this study. Sea surface temperature was calculated by the National Oceanic and Atmospheric Administration Physical Sciences Laboratory (NOAA PSL) using the COARE 3.6 algorithm (Edson et al. 2013, documentation on most recent version available at ftp://ftp.etl.noaa.gov/BLO/Air-Sea/bulkalg/cor3_6/), based on an infrared radiometer and towed thermistor. The COARE algorithm accounts for sharp gradients in temperature on the skin of the ocean surface which cannot be captured by the radiometer/thermistor alone.

2.3 Results

2.3.1 OVERVIEW OF CRUISES

Although a well-defined BSISO event did not occur in either the 2018 or 2019 PISTON cruises, both cruises did experience a variety of atmospheric conditions, both large-scale and locally. This section will discuss the large-scale conditions that occurred during each cruise and relate these large-scale patterns to time series of PISTON radiosonde and ship radar measurements.

2.3.1.1 2018

Sobel et al. (2020) examined the large-scale conditions during the 2018 cruise. The cruise was generally characterized by a background easterly flow, with embedded westward moving disturbances (easterly waves) which propagated over the operations area on the time scale of a few days. This was particularly true in the first leg of the 2018 cruise (late August – early September). In addition to these easterly waves, the cruise was also punctuated by six tropical cyclones, all of which passed to the north of the *TGT* with a range of intensities. The climatological number of tropical cyclones (TC) within a 20°x20° box centered at 133 °E, 15 °N during the PISTON operations period (20 August – 12 October 12 2018) is 5.9, as calculated from the IBTrACS dataset. During these TC passages, the *TGT* experienced enhanced low-level westerlies, as the monsoon flow to the west expanded eastward and merged with the inflow on the southern flanks of the cyclones. These "monsoon tails" (i.e. a belt of strong southwesterly winds and enhanced precipitation linking the monsoon region to the inflow of the storm) are discussed briefly in Sobel et al. (2020) and are a likely topic of future investigation.

A time-height plot of sounding data is shown in Figure 2.4. In mid- to late-August and in early-October, periods of 5-day oscillations between northerly and southerly winds can be seen in the meridional wind (Figure 2.4c). These signatures mark easterly wave passages, as mentioned previously (also see discussion in Section 2.2.4, Figure 15). Extended periods of low-level westerlies (e.g. 1-5 September, 23-27 September) occurred when TC's passed to the north of the TGT. During these TC periods an easterly wave signal (i.e. a 5-day oscillation of meridional winds) is not evident. An intrusion of dry air can be seen in the relative humidity field (Fig 3a) towards the end of the cruise, starting in the upper-levels around 5 October and descending to the mid- and lower- levels over the next few days. Sobel et al. (2020) attributes this period of subsidence and drying to a suppressed phase Intraseasonal Oscillation (ISO) that propagated across the study region during this time.

A time series of area-mean rain rate as observed by SEA-POL is shown in Figure 2.4d. Significant events are annotated. The highest mean rain rates generally occurred with the passage of rain bands associated with the TCs. The exception to this was an MCS which was not associated with a TC that impacted the ship on the night of 7 September. The highest area-mean rain rate values were generally in the 1-2 mm hr^{-1} range, which is similar to what was seen by the C-Band radars in TOGA-COARE (Rickenbach and Rutledge 1998) and DYNAMO (XR15). In late-September to early-October, Typhoon Kong-Rey passed within 400km of the ship. A snapshot of this event from September 30th at 21:30 UTC is shown in Figure 2.5. This passage is marked by a

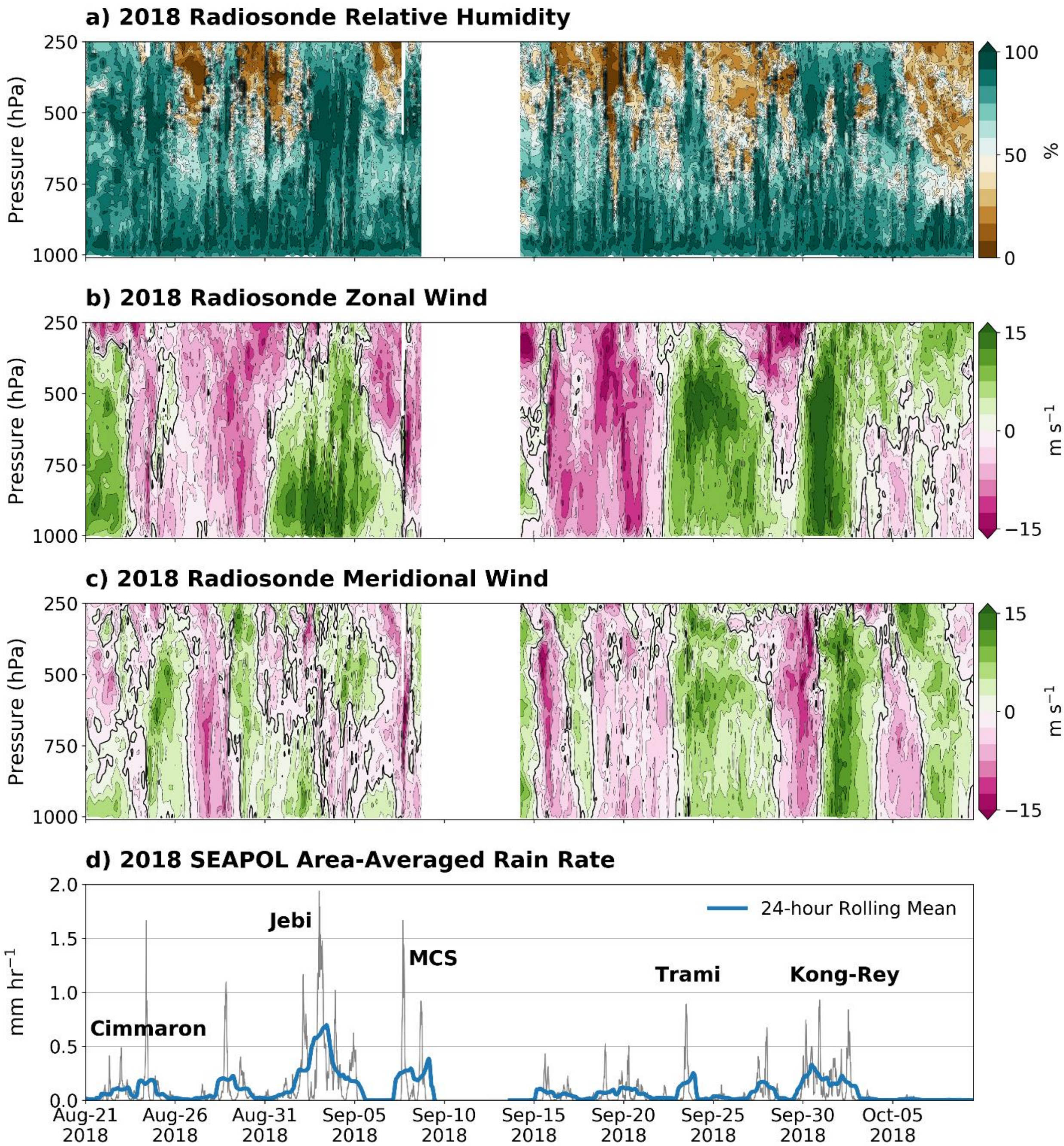

Figure 2.4: Time-height timeseries of relative humidity (a), zonal wind (b), and meridional wind (c) and unconditional area-averaged rain rate as measured by SEA-POL (d) during the 2018 cruise. The thin gray line in (d) is the mean value from every SEA-POL scan, while the thicker blue line is a 24-hour rolling mean. Notable events are annotated in the rain rate plot around the time the occurred. The blank space in mid-September coincides with when the ship was in port and not taking measurements.

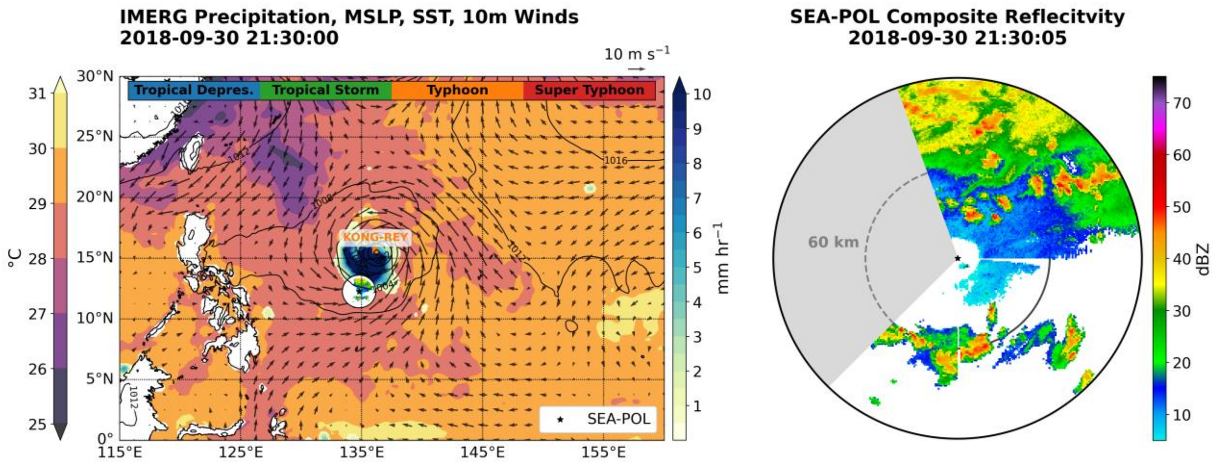

Figure 2.5: IMERG precipitation (green-blue fill), ERA5 SSTs (purple-orange fill), 10m wind speed, and MSLP (black contours) on the left, and SEA-POL reflectivity at the same time on the right. The location of Typhoon Kong-Rey is noted by the orange marker. The grey wedge indicates the portion of SEA-POL's scope which was blanked in order to avoid radiating the ship's bridge. This image is part of a movie covering the entire cruise, available at http://radarmet.atmos.colostate.edu/piston/.

period of strong westerlies and increased rain rates (Figure 2.4d). At the time of Kong-Rey's closest proximity to the *TGT,* wind gusts of 15 m s^{-1} and significant wave heights of up to 4.5 m were observed at the ship. After the passage of Kong-Rey, precipitation was almost completely absent. This period coincided with the suppressed phase ISO discussed earlier.

Figure 2.4d shows some evidence of a rainfall peak approximately every 5 days. It is tempting to link this pattern to easterly waves, which occur on similar time scales. However, because the signal in Figure 2.4d is conflated with tropical cyclone precipitation, the apparent pattern in rain rate cannot be strictly tied to easterly wave processes.

2.3.1.2 2019

Sounding time-height and SEA-POL rain rate time series plots for 2019 are given in Figure 2.6. Unlike the 2018 cruise, which featured numerous easterly waves and tropical cyclones, the "weather" during the 2019 cruise was mainly influenced by a single system. A large monsoon

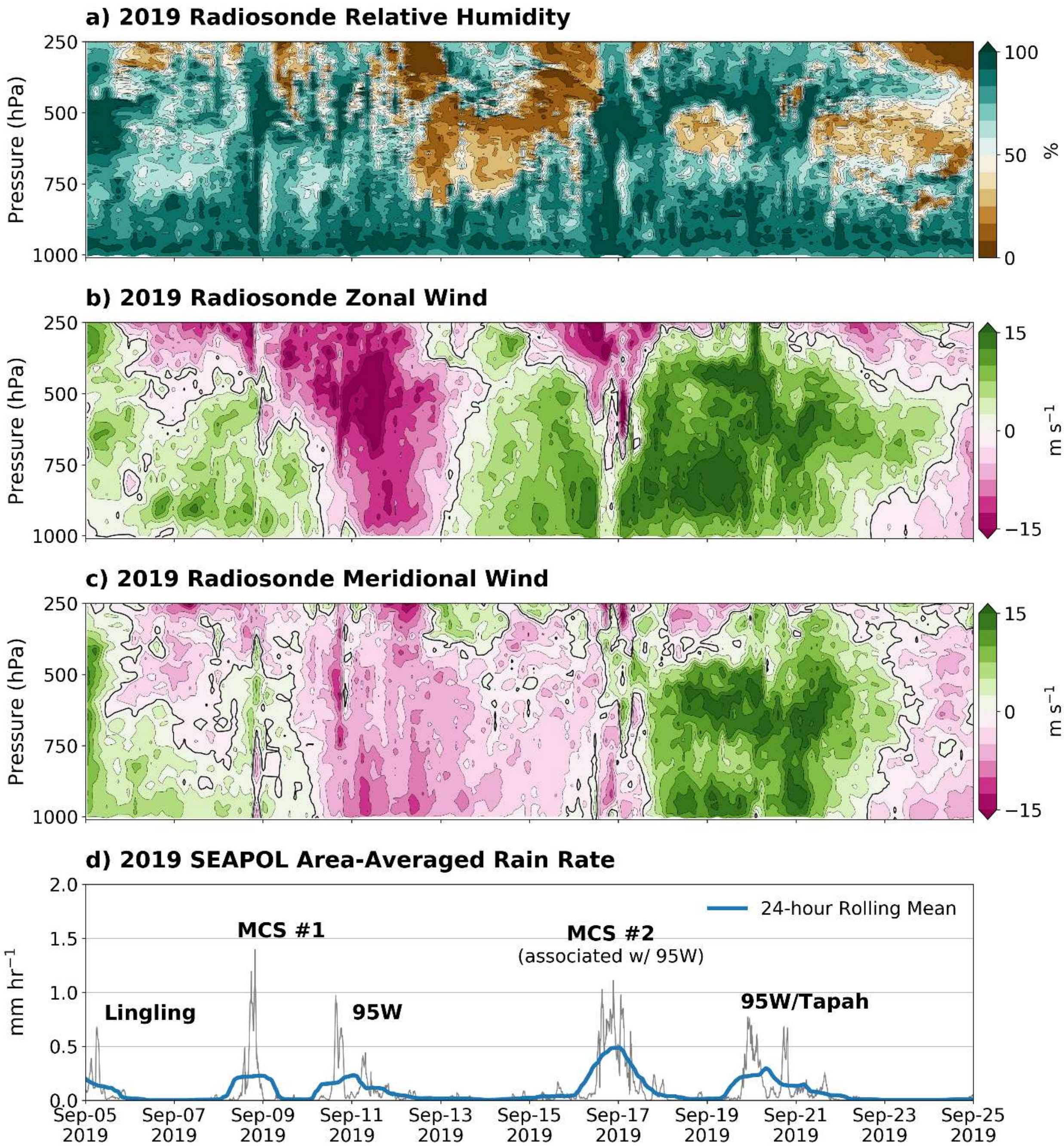

Figure 2.6: As in Figure 2.4, but for the 2019 PISTON Cruise. Note that the time scale on the x-axis is different than in Figure 2.4.

depression (e.g. Beattie and Elsberry 2012), labeled as Invest 95W by the Joint Typhoon Warning Center (JTWC), meandered about the West Pacific for the duration of the *SR* cruise. From 10 September onward, the variability in sounding winds (Figure 2.6b,c) is primarily tied to the location of 95W and where within its broad cyclonic circulation the *SR* was situated. The monsoon depression initially formed to the southeast of the operations area (Figure 2.7), placing the ship in the NW quadrant under northeasterly winds. 95W then moved to the north of the ship, fluctuating in degree of organization and intensity. On 19 September, 95W finally consolidated and strengthened into Tropical Storm Tapah, as it moved to the NW of the ship, placing the *SR* in a region of strong southwesterly inflow. At this point, another monsoon tail formed (Figure 2.8), as was common in the 2018 cruise. Fluctuations in rain rate recorded by SEA-POL (Figure 2.6d) after 10 September can primarily be tied to fluctuations in the strength of 95W/Tapah, with MCS's embedded within the larger-scale tropical storm rain bands moving across the radar observational domain.

2.3.2 PRECIPITATION FEATURES

A time series of precipitation feature count, mean 30-dBZ echo top heights, and mean rain volume is shown in Figure 2.9. Linear and nonlinear features are grouped together for this analysis. For both the 2018 and 2019 cruise, small isolated features occurred most frequently,

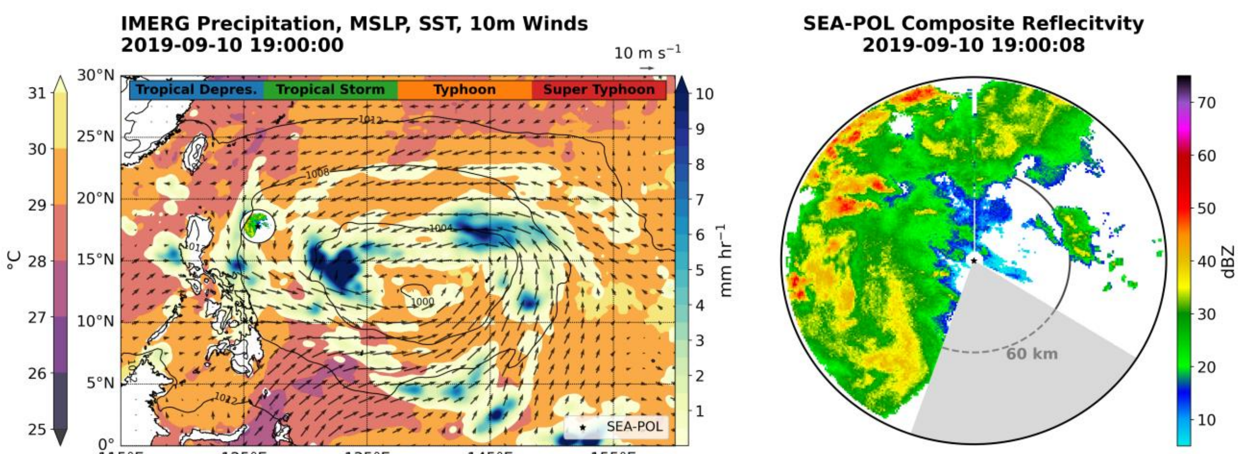

Figure 2.7: As in Figure 2.5, but during the 2019 cruise. The large monsoon gyre 95W can been seen centered around 137 °E, 12.5 °N.

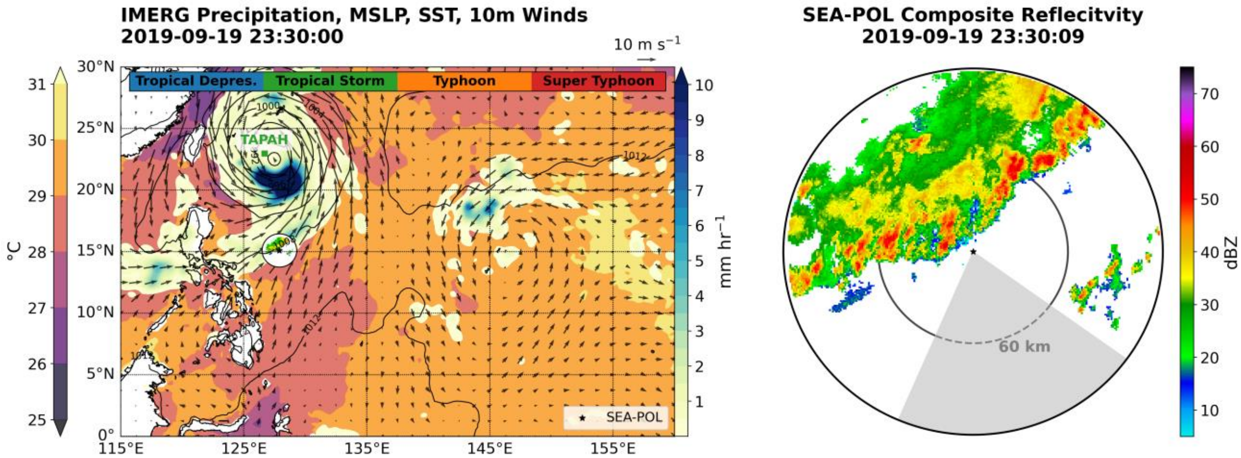

Figure 2.8: As in Figure 2.5, but depicting Tropical Storm Tapah and its monsoon-tail, which was impacting the ship at the time.

MCS's occurred the least frequently, and sub-MCS's fell approximately in the middle. Isolated features were present almost throughout the duration of both cruises. Note that for this feature count, which is calculated as a count per 3-hour window, a single feature may be counted multiple times if it persists for multiple scans within the 3-hour window. However, this multiple-counting effect is expected to be approximately equal for all morphologies, so it is still a valid metric to use.

Examining the 30-dBZ echo top heights (Figure 2.9b,e), isolated features generally had the lowest heights, MCS's had the highest, and again sub-MCS features fell in the middle. It is interesting to note that there was not much fluctuation in mean 30-dBZ echo top height for isolated and sub-MCS over time for either cruise (MCS's were infrequent, so conclusions about their temporal consistency are not made here). A possible exception to this is near the end (6 October onwards) of the 2018 cruise, where the mean 30-dBZ height of isolated features appears to decrease by 1-2 km. This coincides with the dry air intrusion seen in Figure 2.4a, as well as the

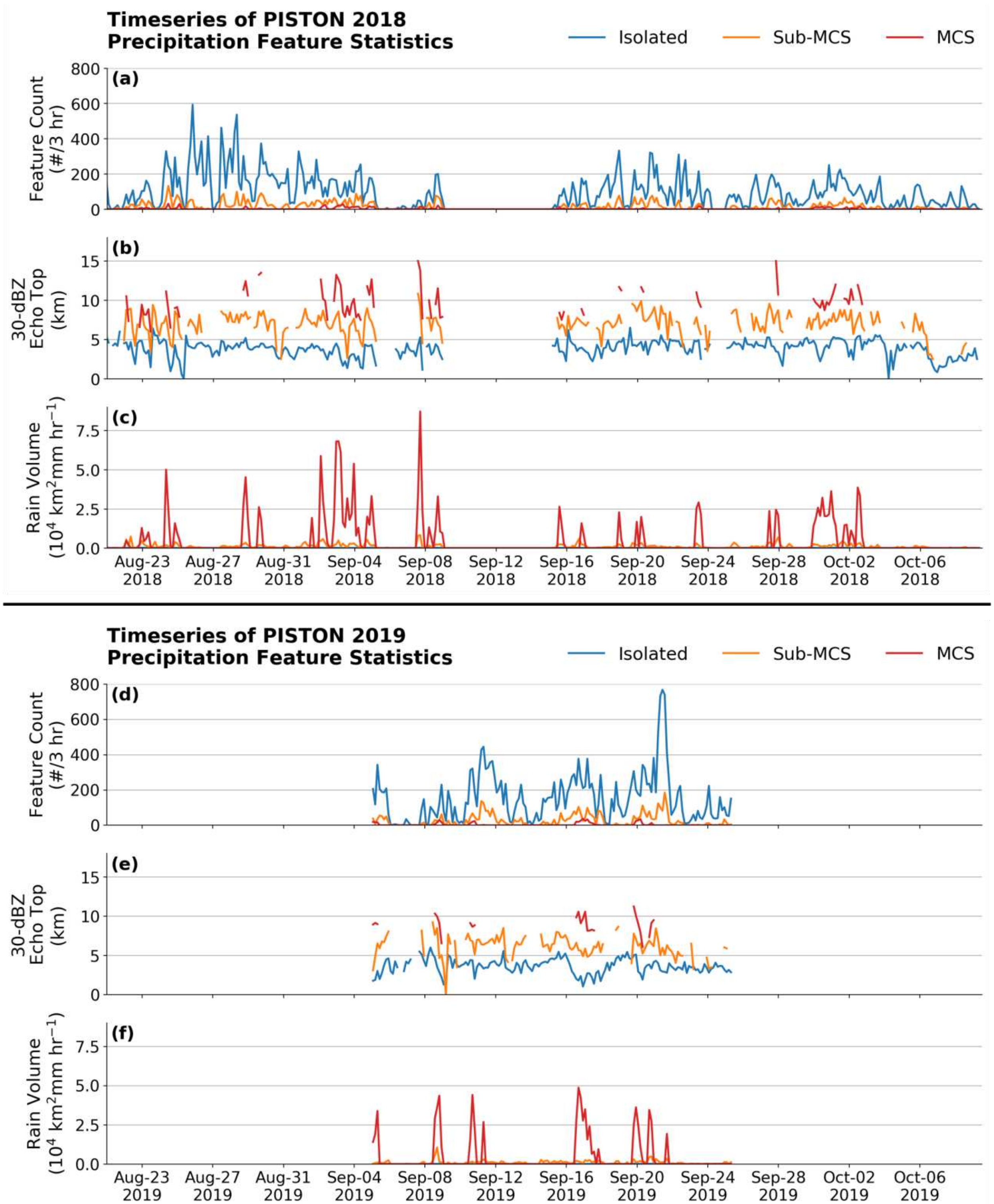

Figure 2.9: Time series of precipitation feature count (a,d), 30-dBZ echo top height (b,e), and rain volume (c,f) for the PISTON 2018 (a,b,c) and 2019 (d,e,f) cruises. Data was binned every 3 hours. Feature count shows the total number of features that occurred in each 3-hour bin, while 30-dBZ echo top height and rain volume show the mean value for all features of a given type in each 3-hour bin.

arrival of the suppressed phase ISO noted by Sobel et al. (2020), both of which would have acted to reduce echo intensity. Also note that the 30-dBZ echo top height of isolated features rarely gets above the freezing level. This suggests that ice-based processes were infrequent in these echoes, rather these features were associated with warm rain processes. However, it is important to consider that this plot includes features at all stages in their life cycles, not just at their maximum intensity. It is probable that the mean echo height of isolated features would be higher if features were only considered at their maximum intensity. This is point is touched on in a later section.

Rain volume (defined as mean rain rate of a feature multiplied by its area) is dominated by MCS's, for both cruises (Figure 2.9c,f). Individual peaks in the rain volume time series match well with the peaks in area-mean rain rate in Figs. 2d and Figure 2.6d, as typhoon rain bands contained large MCS's with strong embedded convection. Note that although the scale of the y-axes on Figure 2.9c and Figure 2.9f are too large too show it, isolated features also contribute a relatively small but consistent rain volume of around 100 km^2 mm hr^{-1}.

Statistics of the different feature morphologies are plotted in Figure 2.10. The ubiquitous nature of isolated cells is once again apparent, with isolated features identified in 91% of the SEA-POL scans (Figure 2.10a). With increasing size (isolated to sub-MCS to MCS) and organization (nonlinear to linear), the morphology frequency decreases. A different pattern is apparent for rain volume (Figure 2.10b). Despite only being present in 13% of SEA-POL scans, MCS's (linear and nonlinear combined) contributed 56% of the total rain volume. In addition to their larger area, Figure 2.10c and Figure 2.10d also show that convective cells within MCS's tended to have higher rain rates and higher 30-dBZ echo top heights, both consistent with increased intensity.

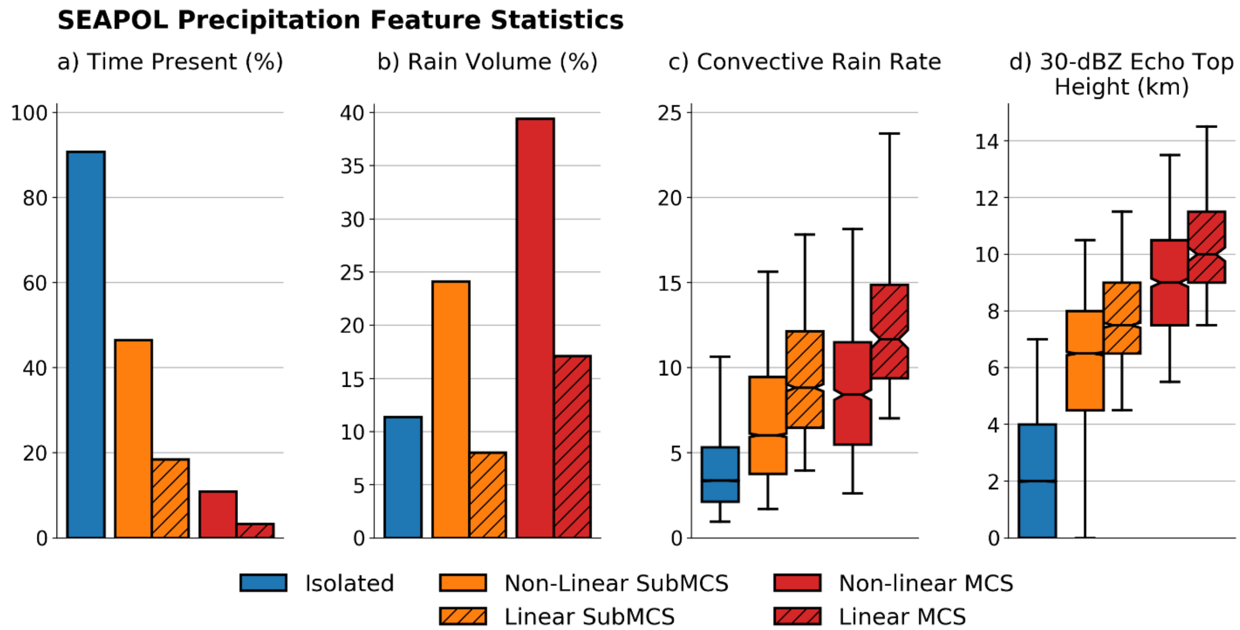

Figure 2.10: SEA-POL precipitation feature occurrence frequency (a), rain volume fraction (b), convective rain rate distribution (c), and 30-dBZ echo top height distribution (d) from both PISTON cruises. Boxplot whiskers represent the 5th and 95th percentile of the data. Notches around the boxplot median values represent the confidence interval around the median, as calculated using a Gaussian-based asymptotic approximation.

For the case of a nonlinear MCS especially, we speculate that this increased cell intensity may be due to cells being less susceptible to entrainment as they are embedded within stratiform areas. Interestingly, mean convective rain rate and 30-dBZ echo top heights of convective cells with linear configuration tended to be enhanced relative to their nonlinear counterparts. The reason for this is unclear and is not examined in this study. Overall, the large raining area of MCS's, combined with their intense embedded convection, allowed for MCS's to dominate the rain volume contribution, despite their infrequent occurrence.

Isolated features on the other hand contribute 11% of the rain volume, despite being present 91% of the time. However, 11% is a non-negligible portion of the total rain. It should also be noted that this analysis considers features at all stages in their lifecycle, not just at their maximum intensity. Weak isolated features which are just forming or nearly dissipated are included in this calculation and will bring down the mean convective rain rates and 30-dBZ echo top heights. This effect can clearly be seen in the 30-dBZ echo top height boxplot for isolated features, where the entire lower quartile of the data consists of features with reflectivity < 30 dBZ (i.e. a 30-dBZ echo top height of 0 km). The impact of this can also be seen in the skewedness of the convective rain rate distribution, which has a long upper tail. This is likely and artifact of the relatively short lifespan of these isolated cells, and the fact that their peak intensity is rather brief. The "forming" and "dissipating" stages of these cells' lifecycles make up a large portion of their existence, and therefore SEA-POL was more likely to sample cells in one of these weaker stages at any given time. However, when isolated features were sampled at near maximum intensity, they had convective rain rates on par with that of sub-MCS's and MCS's (although again these rain rates were relatively short in duration). While MCS's at various points in their lifecycles are also included in this analysis, even the weakest MCSs likely had some embedded convection remaining in it, so they are not as susceptible to this factor. The 11% rain contribution from isolated cells is in close agreement with Rickenbach and Rutledge (1998), who found that isolated convective cells accounted for 12% of the total rainfall observed by the two TOGA COARE ship radars.

2.3.3 PRECIPITATION FEATURES VS. ENVIRONMENTAL CONDITIONS

In this section we examine the relationship between precipitation feature morphology and environmental conditions. First, the influence of active monsoon conditions (defined as periods with strong southwesterly winds) on feature morphology is examined. Figure 2.11 shows the distribution of convective morphologies by wind direction. Here, a wind vector was

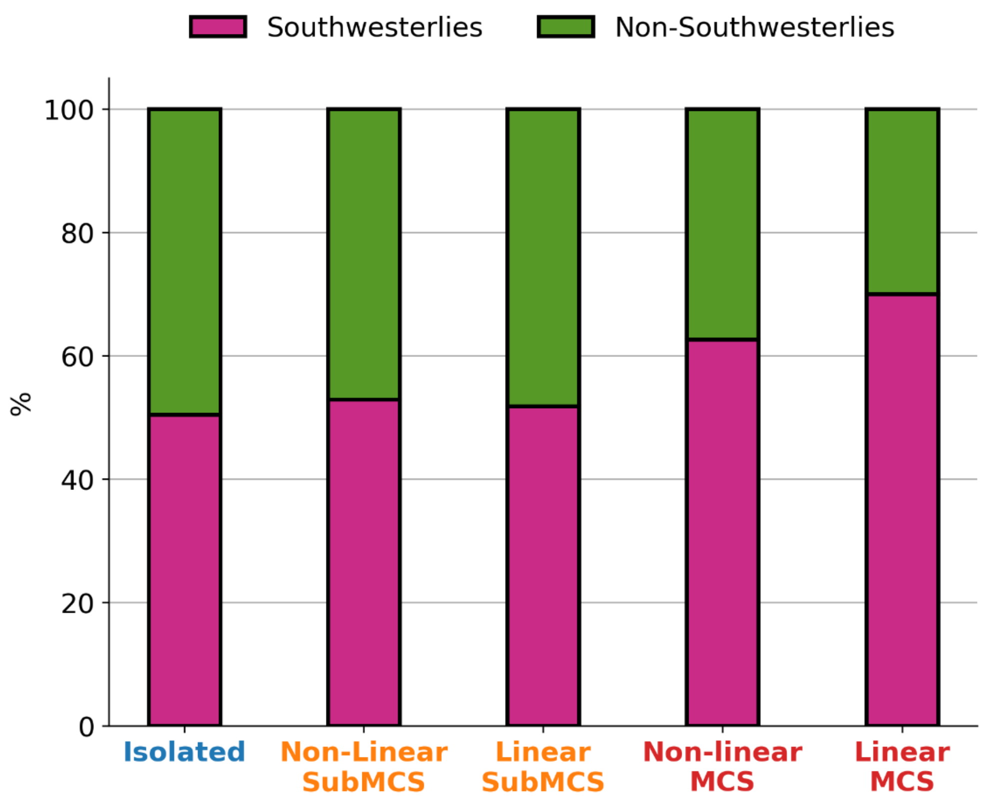

Figure 2.11: Distribution of wind directions at time of occurrence for different feature morphologies. Southwesterlies and Non-southwesterlies we sampled equally using the random-sampling method, described in Sec 3c.

associated with each feature based on the mean low-level (1000-850 hPa) wind recorded by the sounding launched nearest to the time of the feature's occurrence. A feature was labeled as having occurred in a southwesterly regime if the magnitude of the southwesterly component of the wind vector associated with that feature was greater than 3 m s^{-1}. Because of the unequal sampling of southwesterly and non-southwesterly regimes, the following resampling method was preformed to insure equal representation. Each SEA-POL scan was first labeled as occurring in a southwesterly or non-southwesterly regime, following the method above. One thousand radar scans were then chosen at random from each regime, and the precipitation features were then tallied from these scans. Comparisons between other wind regimes were also performed, but showed little-to-no difference in feature frequency. Because of this, and because the southwest monsoon flow is of particular importance in this region, this study will focus only on the difference between designated southwest and non-southwesterly regimes

Figure 2.11 shows that approximately equal numbers of isolated and sub-MCS features occurred in southwesterly and non-southwesterly regimes. MCS's, however, were far more common in the southwesterly regime. This agrees with the results of Xu and Rutledge (2018) and Chudler et al. (2020), which showed that larger features were more frequently present over the South China Sea during periods of strong southwesterly flow. These studies attributed this increase to the enhanced mid-level moisture, surface hear/moisture fluxes, and wind shear present during periods of strong southwesterly flow. Although the current study is examining a different region (east of the Philippines rather than west), it seems reasonable that the same explanation applies here. However, the focus of Xu and Rutledge (2018) and Chudler et al. (2020) was on the BSISO (active BSISO phases are associated with southwesterly winds), and there was no significant BSISO activity during PISTON. Additionally, many of the southwesterly wind regimes during PISTON (specifically during 2018) occurred when a typhoon was passing to the north of the ship, and the increase in MCS's may have been induced by the passing typhoons, especially their outer rain bands. As discussed previously, the rain on the southern flank of these typhoons were often enhanced with a belt of southwesterlies (a "monsoon tail") connecting the typhoon to the core monsoon region, which could enhance precipitation and possibly MCS activity. Regardless of the exact mechanism, a consistent correlation between enhanced southwest monsoon flow and MCS frequency is noted between this current study, Xu and Rutledge (2018) and Chudler et al. (2020).

Figure 2.12 shows the distribution of low-level (1000-850 hPa) wind shear (Figure 2.12a), convective available potential energy (CAPE, Figure 2.12b), and sea surface temperature (SST, Figure 2.12c) associated with the five convective morphologies. Although the distributions in the figure are similar and overlap to a degree, there are statistically significant differences in the median values (as indicated by the notches in the boxplots, see figure description) for different morphologies, which will be discussed here. MCS's tended to occur in higher wind shear regimes than isolated or sub-MCS's. Increased low-level wind shear has been shown to lead to an increase in convective organization, which may have aided the formation of MCS's (Thorpe et al. 1982; LeMone et al. 1998; Lang et al. 2007). However, mesoscale flow features within MCS's can also

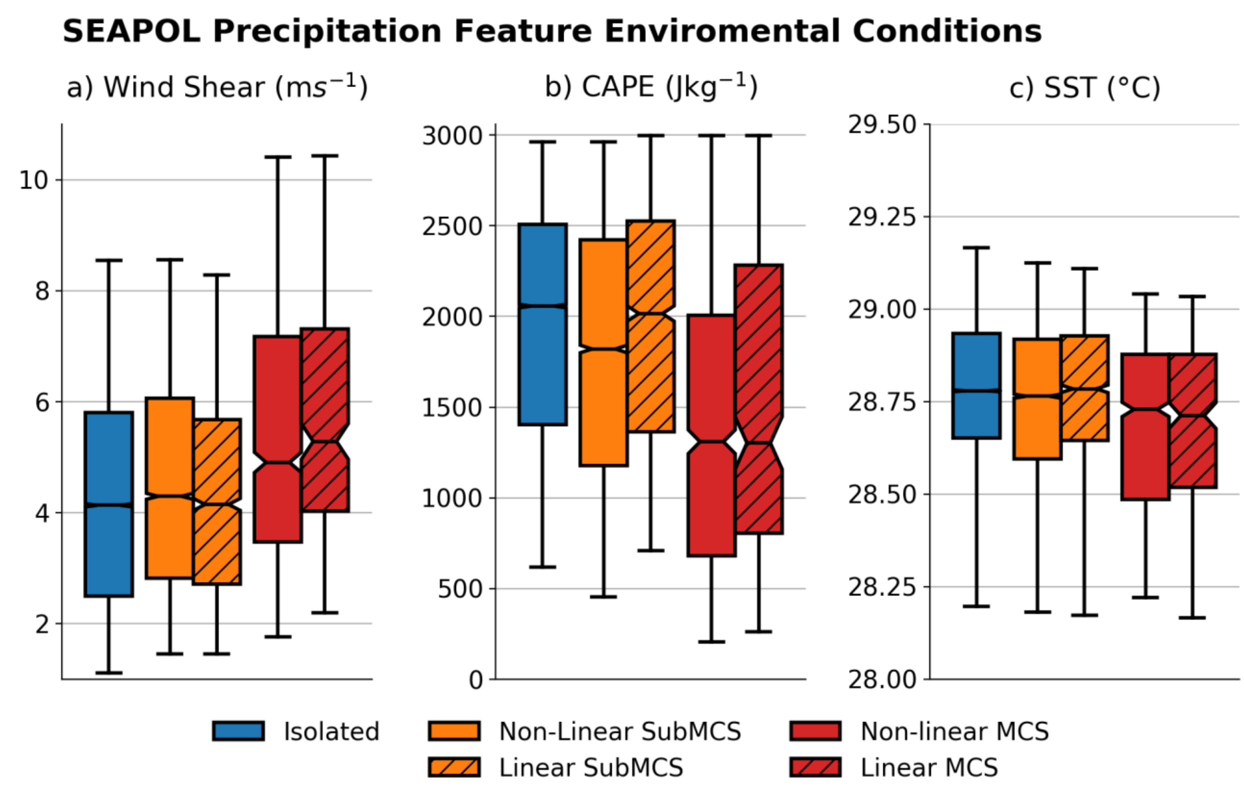

Figure 2.12: 1000-850 hPa wind shear (a), convective available potential energy (CAPE, b), and sea surface temperature (SST, c) statistics for different feature morphologies. Wind shear and CAPE values are derived from atmospheric soundings, SST was calculated based on measurements from an infrared radiometer and a towed thermistor.

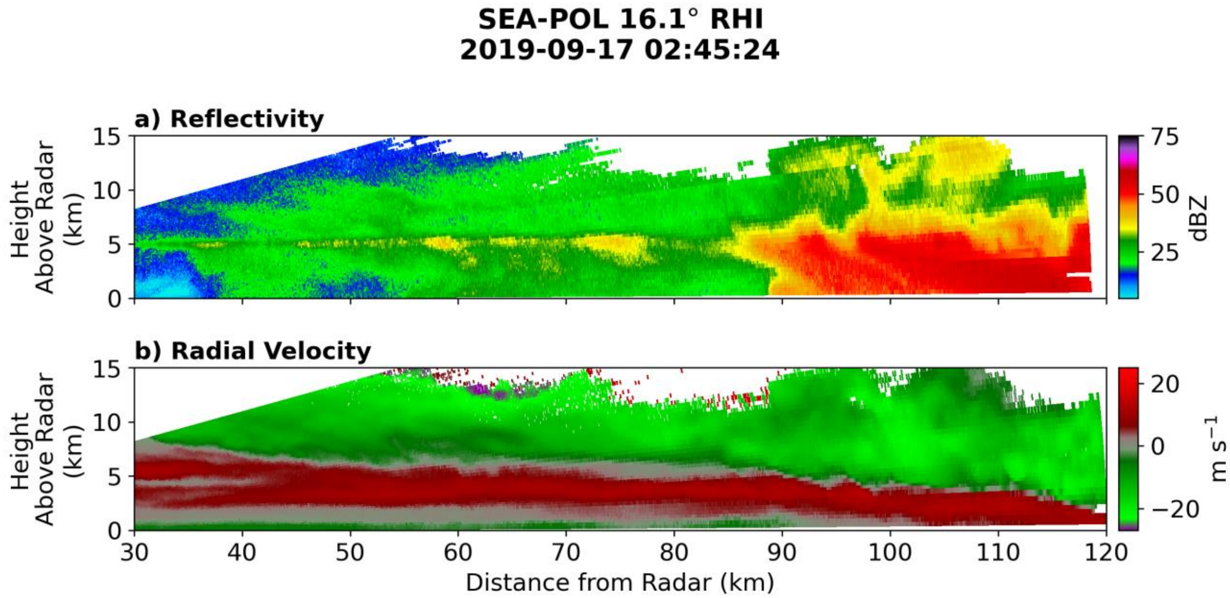

Figure 2.13: Vertical cross-section of radar reflectivity (a) and radial velocity (b) from a MCS observed by SEAPOL during the 2019 cruise.

act to increase low-level shear (i.e. a descending rear inflow jet). Therefore, it cannot be ruled out that the observed increase in shear may be due to processes within MCS's themselves, rather than changes background environmental conditions. An example of this is provided in Figure 2.13, which shows a vertical cross section of an MCS observed by SEA-POL during PISTON 2019. Here, a descending rear inflow jet can be seen underlying a region of front-to-rear outflow, leading to strong vertical wind shear. Unlike wind shear, CAPE is notably lower for MCS's than for other morphologies. This could be a result of soundings that were launched into MCS's, or soundings that experienced surface air that had been modified by nearby MCS's. For example, these MCS's likely produced substantial cold pools, evaporative cooling below their stratiform components, and reduced solar heating of the surface due to cloud shading. Each of these processes would serve to reduce the low-level temperature, which would in-turn reduce surface-based CAPE. This relationship can be seen in Figure 2.14. In addition to CAPE being lower near

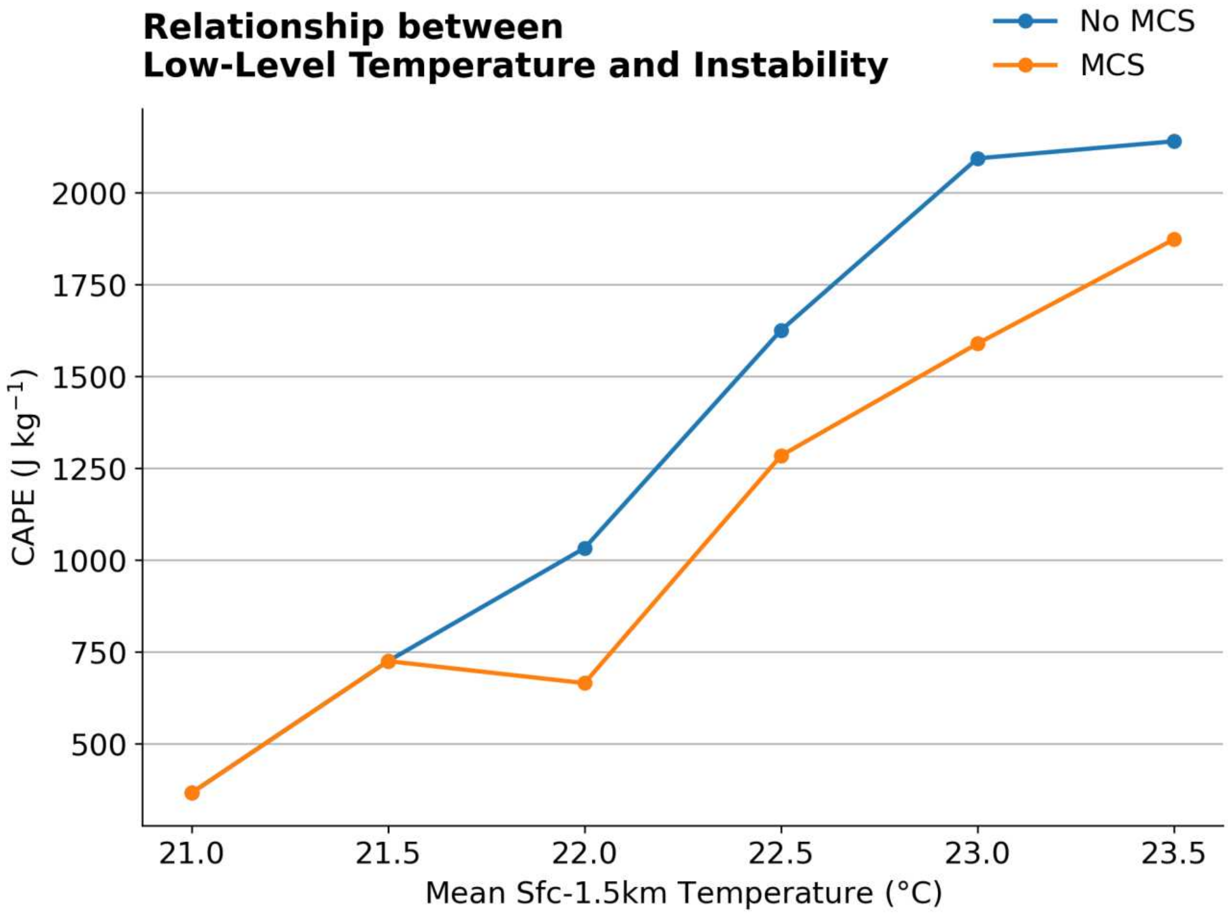

Figure 2.14: Mean convective available potential energy (CAPE) for different mean boundary layer height temperatures for times where an MCS was present (orange line) and no MCS was present (blue line).

MCS's, Figure 2.14 also shows that lower surface-1.5 km mean temperatures correlate with decreasing instability. Furthermore, convective air motions within the MCS's themselves may reduce instability by adjusting the local temperature profile towards moist adiabatic, i.e., the convective adjustment process. This is all to say that there are several reasons to expect lower instability in and around MCS's, as seen in Figure 2.12. Similarly, the SST's associated with MCS's are slightly lower than other morphologies, likely due to extensive cloud shielding and reduced solar insolation. For sub-MCS's, linear systems tended to form in higher-shear environments that nonlinear systems. This agrees with previous studies that highlighted the importance of low-level shear in generating organized convective lines (Houze and Cheng 1997; Rotunno et al. 1988; LeMone 1998; Weisman et al. 1988; Weisman and Rotunno 2004; Liu and Zipser 2013).

2.3.4 EASTERLY WAVES

This section will examine the how environmental conditions and precipitation feature statistics varied over different easterly wave phases observed during the 2018 cruise. Details on the methodology used for wave phase detection can be found in Section 2.2.4.

Figure 2.15 shows a time-height plot of meridional wind (*v*), both with and without a 3-7 bandpass filter applied (Figure 2.15a and Figure 2.15b, respectively). A timeseries plot of 700mb wind, with easterly wave phases marked, is also provided in Figure 2.15c. As expected, the bandpass filter effectively culls out variation in the meridional wind on the timescale of easterly waves. Oscillations in the meridional wind on a timescale of 3-5 days are clearly seen in the filtered plot. Wave phases are also marked in the middle of the plot, as labeled by the automated detection algorithm discussed in Section 2.2.4. Northerly (southerly) phases correspond with a filtered 700 hPa wind of less than -2 m s^{-1} (greater than 2 m s^{-1}), and toughs and ridges fall in-between. The 18 September – 4 October period was not considered in this analysis, as that period was significantly influenced by the passage of Typhoon Trami and Super Typhoon Kong-Rey. Overall, only two full wave events were captured, in addition to two “partial” wave events. However, the ship made a run north just before port call (to make oceanographic transects ahead of a typhoon), and in doing so moved out of the wave, so the other phases were not captured. In total, 4 northerly periods, 4 troughs, 2 ridges, and 5 southerly periods were detected. Given this relatively small sample size, the following discussion may not necessarily be representative of all easterly waves in this region, and caution should be exercised in generalizing results. However,

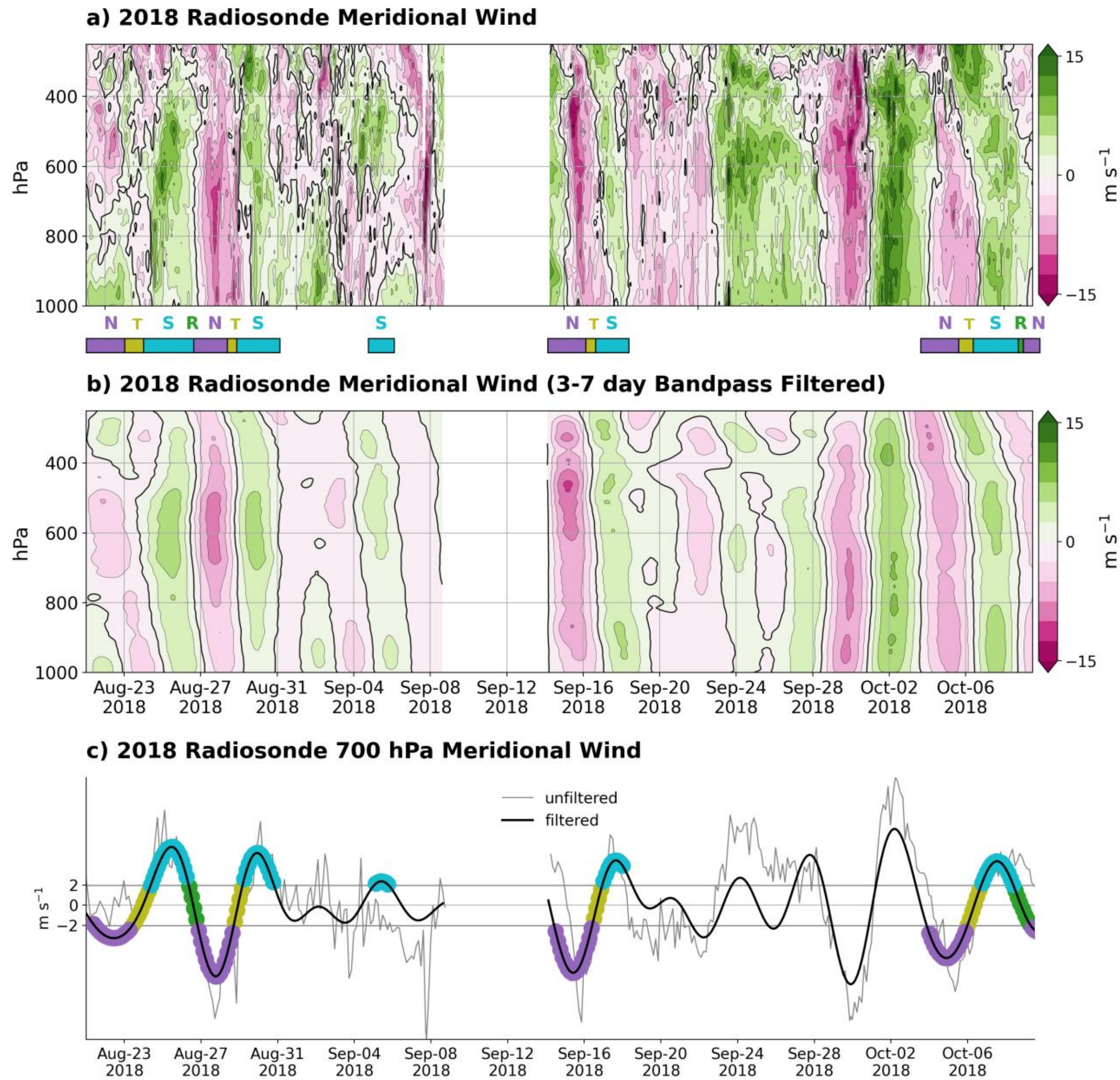

Figure 2.15: Meridional wind from PISTON 2018 sounding data (a), and with 3-7-day bandpass filter applied (b). Lines/labels between (a) and (b) indicate whether that period is identified as a northerly (N, purple), trough (T, yellow), southerly (S, cyan), or ridge (R, green) wave phase. Panel (c) shows a timeseries of the 700 hPa meridional wind, both with and without the 3-7-day bandpass filter. The wind thresholds for easterly wave detection (-2 and 2 m s^{-1}, see Section 2.2.4) are marked, and the line is colored by the detected wave phase.

the uniqueness of these measurements makes this analysis valuable. The wave phases as labeled by the automated detection algorithm were subjectively verified through manual inspection of

ERA5 wind and pressure fields. Although the ship did move around during the field campaign, the spatial extent of the movement during easterly wave passages was small compared to the size of the waves themselves, so results should not be significantly impacted.

Radiosonde measurements were composited by wave phase (shown in Figure 2.16). The composited meridional wind appears as expected, with a southerly wind signal throughout the column associated with the southerly phase, and northerly wind associated with the northerly phase (Figure 2.16b). The zonal wind pattern (Figure 2.16a) shows an easterly (westerly) anomaly in the trough (ridge) phase from the surface to about 500 hPa, with some evidence of a reversal in direction above that level. For temperatures (Figure 2.16c), southerly (northerly) phases featured warm (cold) anomalies throughout most of the column, with the exception of the surface-900 hPa level, wherein the anomalies were shifted about 90 degrees, and warm (cold) anomalies were found in the ridge (trough) phase. For relative humidity (Figure 2.16d), troughs (ridges) were associated with moist (dry) anomalies throughout the column.

The relations discussed above differ in several ways from the results of P03. Looking at easterly waves in the East Pacific, P03 found that *u* and *v* were positively correlated. However, in this study, *u* and *v* appear to be about 90-degrees out-of-phase, with *v* peaking in southerly phases and *u* peaking in troughs. This is important, as a positive correlation of *u* and *v* is needed for barotropic conversion of eddy available potential energy to kinetic energy (Maloney and Dickinson 2003; P03). The fact that the waves observed during PISTON apparently did not feature positively correlated *u* and *v* winds (i.e. the waves were not tilted in the horizontal plane) suggests that these waves were drawing their energy from some other process. P03 also noted a westward tilt with height in the waves they analyzed, suggesting the possibility of baroclinic energy

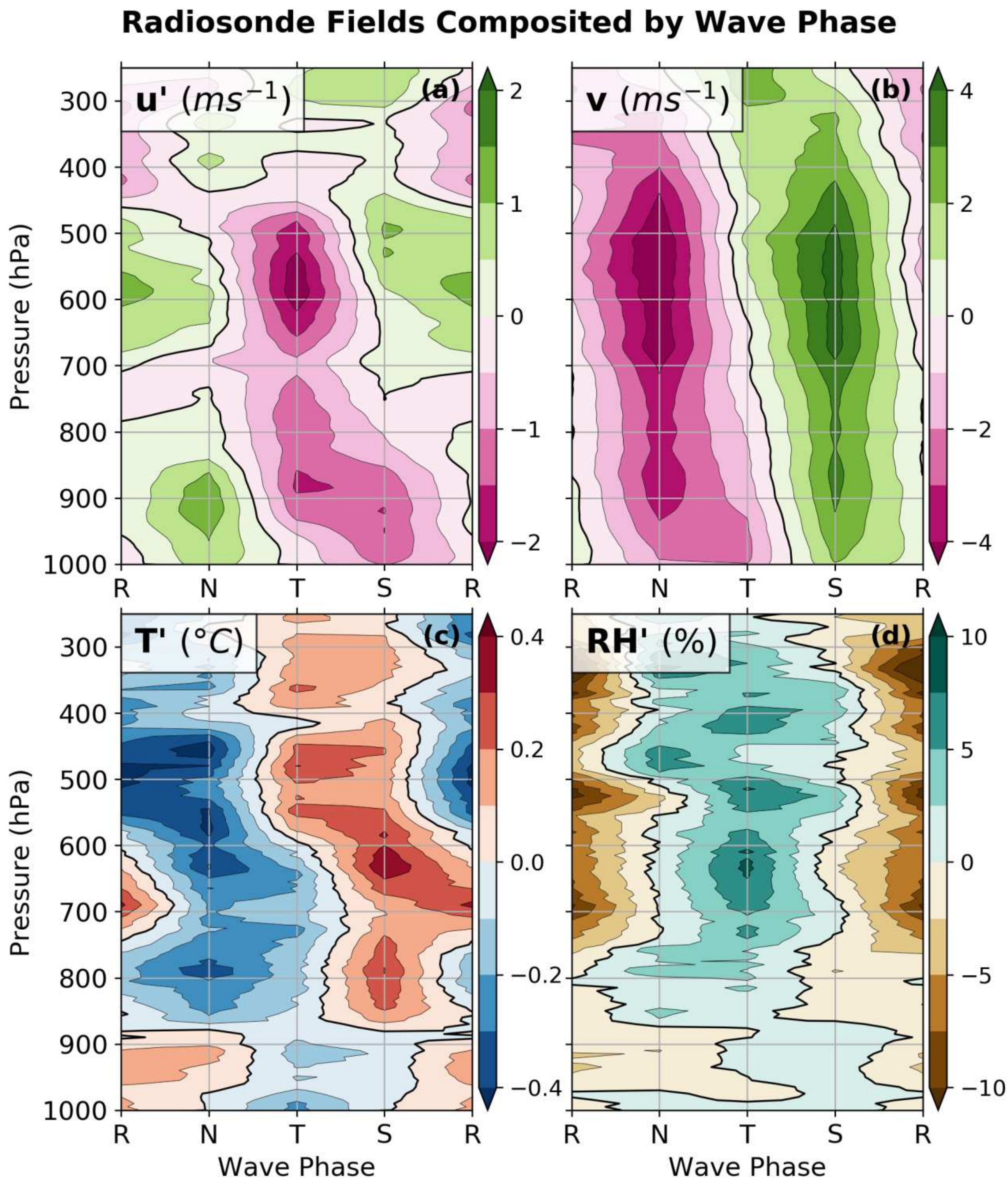

Figure 2.16: PISTON 2018 radiosonde zonal wind anomaly (a), meridional wind (b), temperature anomaly (c), and relative humidity anomaly (d) composited by the easterly wave phase they occurred in (R = Ridge, N = Northerly, T = Trough, S = Southerly. Anomalies were calculated against the mean of that variable across the 2018 operations period.

conversion (e.g. Lau and Lau 1992, Maloney and Dickinson 2003), but no significant tilt is evident in Figure 2.16, so baroclinic contribution to wave growth also appears to be insignificant for the PISTON waves. This leaves diabatic heating as the remaining possible energy source, wherein the latent heat release and rising air within convection leads to generation of eddy kinetic energy. This is further supported by the fact that area-mean rain rate anomalies maximize in the trough and southerly phases (not shown), which matches the location of positive temperature anomalies in Figure 2.16c. Additionally, P03 found that at low levels, warming (cooling) occurred in the northerly (southerly) phase, while this study finds warm (cold) low levels in the ridge (trough) phase. Overall, it is not too shocking that the structure of the PISTON easterly waves differs from those analyzed in P03, as they occurred in different areas of the world (the West and East Pacific, respectively), where the sources and energetics differ substantially (Thorncroft and Hoskins 1994a; Thorncroft and Hoskins 1994b; Dickinson and Molinari 2002; Maloney and Dickinson 2003, see discussion in Section 2.1.3).

To further examine these waves and their horizontal structure, ERA5 700 hPa geopotential height and wind vector data were collected within 10 degrees of the *TGT* and composited by easterly wave phase (Figure 2.17). Also plotted is the precipitation frequency derived from IMERG. Note that the x- and y-axis of these plots are not absolute geographical coordinates of longitude and latitude, but rather indicate a distance from the ship. The general structure of the geopotential height lines and wind barbs follows what one would expect to see in easterly waves, which have "inverted trough" structures (Frank 1969). The ridge phase (Figure 2.17a) shows some evidence of a southwest-to-northeast tilt with increasing latitude, however this tilt is less clear in the other phases. It is apparent in Figure 2.17c that the trough phase

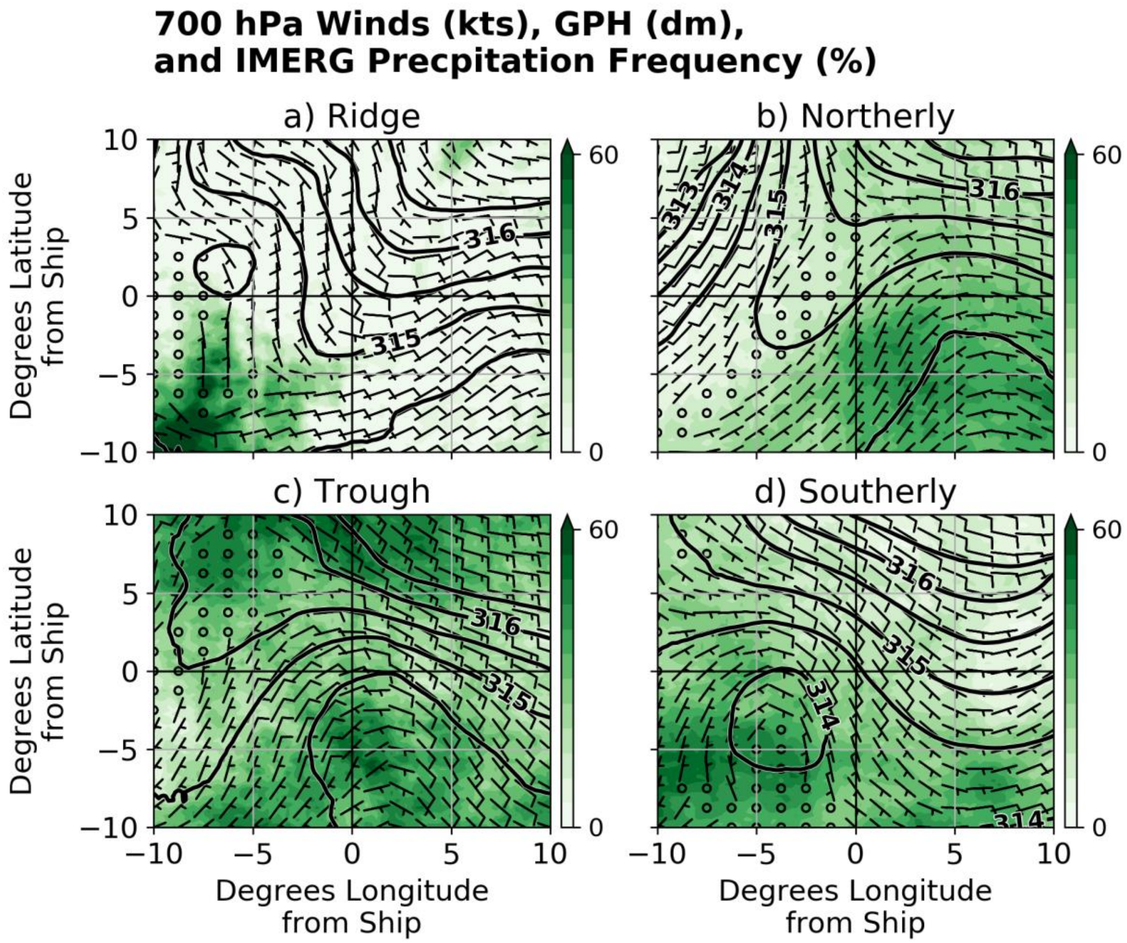

Figure 2.17: ERA5 Reanalysis 700 hPa wind (barbs), geopotential height (black contours) and IMERG precipitation frequency (green shading) composited by easterly wave phase.

features the highest probability of precipitation. In the northerly (southerly) panel, the trough of the wave lies to the east (west) of the ship, and is co-located with a region of enhanced precipitation. In the trough panel, much of the map is covered in higher precipitation probabilities. This agrees with the results of Figure 2.16, which showed higher relative humidity anomalies associated with troughs.

Looking at precipitation features again, Figure 2.18 shows the number of precipitation features as a function of convective morphology and the easterly wave phase within which they occurred in. Some patterns are evident, however the unequal sampling of wave phases during the cruise requires cautious interpretation of this table. For example, although the highest number of isolated features occurred in southerly phases, this is at least in part due to the fact that southerly phases were simply sampled more often than the other phases. On the other hand, even though only slightly more linear MCS's occurred during troughs than during northerly or southerly phases, troughs were sampled much less frequently than northerly or southerly phases, so the high number of linear MCS's is more significant in this regard.

The issue of unequal sampling can be overcome with a random-sampling method, similar to what was described in Section 2.3.3. Each radar scan was first labeled by the wave phase it occurred in. Again one-thousand scans were randomly sampled (with replacement) for each of the 4 phases. Precipitation features were then identified and classified from the resulting 4,000 scans, which had an equal number of samples from each wave phase. Figure 2.19 shows the

	Isolated	Non-Linear SubMCS	Linear SubMCS	Non-linear MCS	Linear MCS	Total
Ridge	475	24	2	0	0	501
Northerly	2981	701	133	45	5	3865
Trough	1083	355	56	31	8	1533
Southerly	3800	1011	177	97	6	5091
Total	8339	2091	368	173	19	10990

Figure 2.18: PISTON 2018 precipitation feature count by wave phase and morphology. Darker colors correspond to higher numbers, with the 'total' boxes being colored on a separate scale.

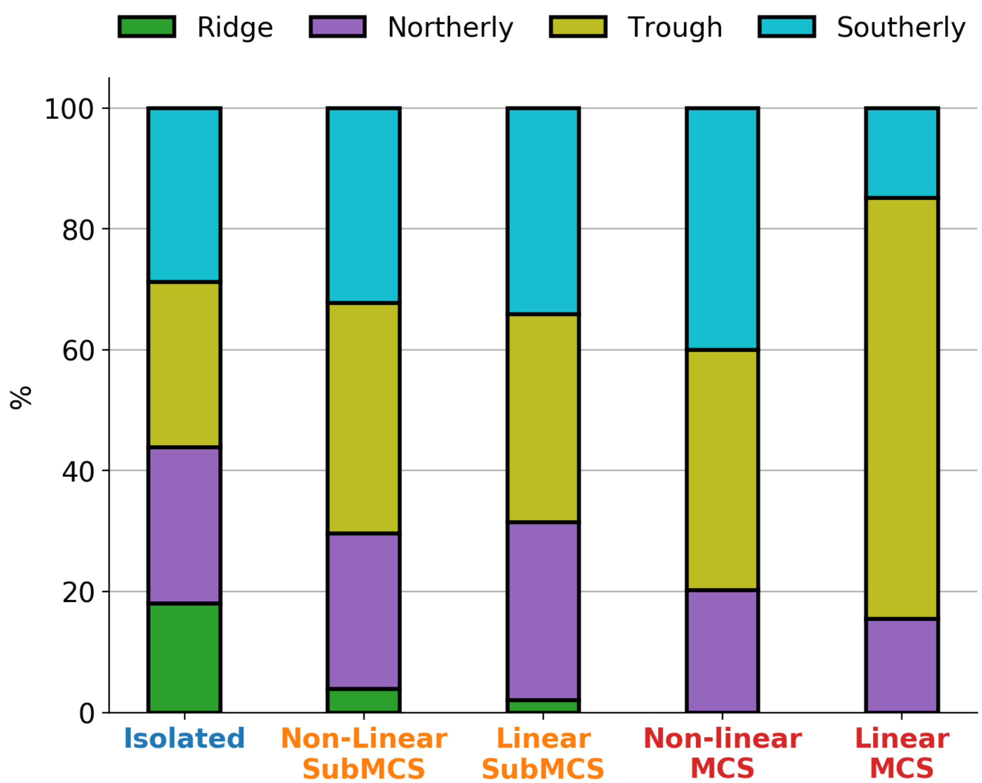

Figure 2.19: Distribution of the easterly wave phases under which different precipitation feature morphologies occurred.

distribution of wave phases that different feature morphologies occurred under, based on this re-sampled SEA-POL data. Compared to other feature types, isolated features were most likely to occur during ridge phases. As mentioned previously, ridges were typically associated with reduced relative humidity anomalies throughout the column. These relatively dry conditions were apparently enough to suppress the formation of even moderate-sized sub-MCS's (and certainly MCS's). On the other hand, clearer skies may have led to increased solar insolation and SST increases, which promote the formation of the isolated cells. These shallow cells may be important in moistening the lower troposphere to support more widespread convection later, similar to the "discharge-recharge" theory for Madden-Julian Oscillation onset (Bladé and Hartmann 1993; Xu and Rutledge 2016).

On the other end of the size and organization spectrum, linear MCS's were by far most likely to occur in the troughs of easterly waves. The high moisture content seen during troughs apparently led to conditions which were conducive for large, organized MCS's. The MCS's themselves may also be contributing to the high moisture content seen in Figure 2.16. Furthermore, these MCS's also produced broad regions of stratiform rain, which leads to a top-heavy heating profile (Houze 1989, Schumacher et al. 2007, Tao et al. 2010). This is consistent with Figure 2.16c, which shows more heating aloft in the trough phase. There is also some evidence of deep vertical shear in the meridional wind plot of Figure 2.16, which may have acted to expand stratiform regions through detrainment of ice hydrometeors from deep convection (Houze 2004; Yamada et al. 2010). While linear MCS's occurred most often in troughs, nonlinear MCS's were relatively more likely to be associated with southerly phases. As southerly phases follow trough passages, it seems plausible that this transition from linear to nonlinear could be a result of the main convective line of MCS's weakening or moving out of range of SEA-POL as the trough axes passed. On the other hand, sub-MCS's were more likely to be found in northerly phases than MCS's. Northerly phases follow ridges (which featured a relatively high number of isolated features) and precede troughs (which featured a large number of MCS's), so there is evidence that the northerly phases are a sort of "transition zone' from small isolated features to large MCS's. This transition from sub-MCS's (which typically have a relatively high convective fraction) to nonlinear MCS's (which have a high stratiform fraction) as the wave transitions from northerly to trough to southerly agrees with the findings of P03, who noted a transition from convective to stratiform rainfall across the trough axes.

2.4 Summary and Conclusions

During the PISTON field campaign, the CSU SEA-POL radar sampled convection across a broad spectrum of sizes and organizations. Although no discernable BSISO event occurred, the ships encountered a wide variety of other interesting large-scale atmospheric phenomena, such as easterly waves and typhoons. The purpose of this study was to analyze the convection observed by SEA-POL during PISTON, and to tie the variability in convective morphology to the large-scale conditions the convection was embedded within.

During the 2018 cruise (particularly in the first half), much of the variability was characterized by the passage of easterly waves on 3-5-day time scales. The 2018 cruise was also marked by the passage of several tropical cyclones, the outer rainbands of which impacted the ship as the storms moved to the north. Several of these storms also produced "monsoon tails", wherein a belt of southwesterly winds and enhanced precipitation connected the core of the monsoon region over the South China Sea and Bay of Bengal to the southern flank inflow of the cyclones. These monsoon tails and associated rainfall tended to persist in the operations area even after the tropical system had moved well away from the ship. The largest precipitation events during 2018 were generally tied to the passage of these typhoons.

While 2018 featured numerous easterly waves and typhoons all impacting the ship separately, the weather on the 2019 cruise was mainly controlled by one phenomenon: a large monsoon gyre which meandered about the western North Pacific for most of the operational period. Designated as Invest 95W by the JTWC, the broad cyclonic system fluctuated in intensity and organization for much of the cruise, before eventually becoming Tropical Storm Tapah.

Variation in wind profiles at the ship was mainly tied to the location of 95W/Tapah, and variation in precipitation tied to fluctuations in the monsoon gyre's organization.

An automated precipitation feature detection/classification algorithm (which was updated from the XR15 method to more accurately distinguish linear convective feature) was run on both years of the SEA-POL dataset. It was found that occurrence frequency and rain volume contribution had an opposite relation the feature size. That is, smaller features occurred more frequently but produced less of the total rain, while larger features occurred infrequently but produced a disproportionate fraction of the rain. For example, isolated features (< 20km in length) were present in 91% of radar scans, and contributed 11% of the total rain volume. Conversely, MCS's (area > 2000km^2) were present in only 13% of scans yet were responsible for 56% of the total rain volume. Larger features also tended to be more intense, as defined by larger mean convective rain rates and taller 30-dBZ echo top heights. It is hypothesized that this is a result of convection in larger features being shielded from entrainment of dry air. Linear features also tended to be more intense than their nonlinear counterparts, possibly due to the impact of vorticity balance between cold pools and wind shear (Rotunno et al. 1988, Weisman et al. 1988, Weisman and Rotunno 2004).

Precipitation feature statistics were examined as a function of the environmental conditions which they occurred in. It was found that southwesterly wind regimes brought a higher likelihood of MCS's, while non-southwesterly regimes featured all morphologies at approximately equal frequencies. The finding of more MCS's in southwesterly wind regimes, which can be thought of as periods with an active monsoon flow, agrees with the results of Xu and Rutledge (2018) and Chudler et al. (2020), which linked the increase in feature size to an increase in wind shear and mid-tropospheric moisture. Similarly, MCS's were also found to preferentially form when low-level wind shear was greatest. Conversely, CAPE and SST's were found to be lower when MCS's were present. This may be a result of the MCS's themselves impacting the environment in ways that reduce CAPE and SST's. Linear sub-MCS's were found to occur in higher low-level wind shear than nonlinear sub-MCS's, agreeing with previous studies suggesting that low-level wind shear is important in generating organized convective lines (Houze and Cheng 1997; Rotunno et al. 1988; LeMone 1998; Weisman et al. 1988; Weisman and Rotunno 2004; Liu and Zipser 2013).

Finally, the environmental conditions associated with the different phases of easterly waves was examined, as well as the precipitation features that occurred in them. Before summarizing these results, it is important to note that only a small sample of waves (2 full waves and 2 partial waves) were observed during PISTON. Therefore our results are likely not necessarily representative of all easterly waves in the region, and caution should be exercised in making any general conclusions. That being said, to our knowledge there have been no in-situ field campaign measurements of easterly waves in the northern West Pacific, so the results are still valuable and could serve as a focus of further research.

Vertical profiles of *u* and *v* were found to be 90-degrees out-of-phase, in contrast with previous studies which showed positive correlation between the two. This has important implications to barotropic conversion and energy extraction from the mean flow, which is thought to be a main source of energy for easterly waves in this region. Because positive precipitation anomalies were correlated with positive temperature anomalies, it is possible that the easterly waves observed during PISTON relied on diabatic heating as a main source of energy.

One explanation for the apparent lack of barotropic processes is that these waves were observed further east than the region where maximum strengthening usually occurs, so perhaps baroclinic conversion processes had not yet begun. It was also found that the trough (ridge) of waves were associated with moist (dry) relative humidity anomalies, also in slight contradiction to previous analysis. With regard to precipitation features, ridges featured a relatively high number of isolated features, troughs a high number of linear MCS's, and northerly and southerly phases were found to act as a transition zone between the two.

Several other areas of future research exist for the PISTON dataset. While this study focused on large scale conditions and statistics of precipitation features, future studies will examine individual convective events on a case study basis, using the SEA-POL polarimetric data and detailed vertical cross-section scans. The polarimetric data in particular will provide important insights to the microphysical characteristics of convection in the West Pacific, and analysis on this topic is already underway. The impact of rainfall on the ocean surface (and vice versa) using a freshwater lens detection algorithm such as in Thompson et al. (2019) is also an enticing avenue for future work. Although this study primarily examined convection within the 120km range of SEA-POL, it also lays the foundation for future work looking at the impact of this convection on the global climate system. For example, because this study links convective morphologies to environmental conditions and synoptic patterns, analysis on the frequency at which these conditions and patterns occur would lead to insights on the broader-scale impacts of this convection on the atmosphere. Overall, the suite of scientific instrumentation on board the *TGT* and *SR* captured a multitude of atmospheric and oceanic measurements, and the multifaceted dataset affords exciting opportunities to comprehensively examine the weather phenomena which were observed.

Chapter 3: Unique Radar Observations of Large Raindrops in Tropical Warm Rain During PISTON[1]

3.1 Introduction and Background

3.1.1 TROPICAL WARM RAIN

Over the tropical oceans, isolated raining cells, including some with tops near the freezing level are ubiquitous. These warm rain convective cells, defined as clouds which produce precipitation from condensation and collision-coalescence, are an important feature over the warm oceans (Johnson et al. 1999; Lau and Wu 2003). Previous studies have found that between 10-30% of all precipitation in the tropics falls as warm rain, depending on the method used to identify warm rain cells (Rickenbach and Rutledge 1998; Johnson et al. 1999; Petty 1999; Stephens et al. 2002; Lau and Wu 2003; Schumacher et al. 2007). In addition to this precipitation contribution, warm rain cells have also been shown to have significant impacts on heating profiles. During the Tropical Ocean and Global Atmosphere Coupled Ocean–Atmosphere Response Experiment (TOGA COARE), Schumacher et al. (2007) observed several periods with enhanced low-level heating, and attributed these periods to latent heating owing to the presence of cumulus congestus clouds. The large albedo of these clouds (compared to the dark ocean below) also has significant impacts on radiative forcing (Hartman and Short 1980; Slingo 1990). In Johnson et al. (1999), a trimodal structure of tropical convection was demonstrated, wherein

This chapter is a slightly modified version of the work under review for publication in *Monthly Weather Review* as: Chudler, K., S. A. Rutledge, B. Dolan (under review), Unique Radar Observations of Large Raindrops in Tropical Warm Rain During PISTON cumulus congestus served as an intermediary between shallow fair-weather (including non-precipitating) cumulus and deep cumulonimbus-producing convection. These congestus clouds, which were argued to be primarily associated with warm rain processes, act to moisten the mid-levels of the atmosphere, which is an important precursor to deep convection. It is clear that this shallow to moderate depth convection, producing precipitation through primarily warm-rain processes has important feedbacks to latent heating and energetics, the water cycle, and the broader tropical environment.

An interesting phenomenon which has previously been observed in the tropics is the presence of large (> 4.5 mm) raindrops in warm rain cells (Beard et al. 1986; Rauber et al 1991; Takahashi et al. 1995; Szumowski et al. 1997; Szumowski et al. 1998; Szumowski et al. 1999; Hobbs and Rangno 2004; Gatlin et al. 2015). Drops of this size would not be particularly remarkable in the midlatitudes where melting hail routinely leads to large drops. However, in the tropics, drop sizes are typically smaller (median drop diameter D_0 < 1 mm; Bringi et al. 2003; Ulbirch and Atlas 2007; Bringi et al. 2009; Thurai et al. 2010; Thompson et al. 2015; Dolan et al. 2018), so the presence of large drops is more remarkable. Moreover, previous studies (Beard et al. 1986; Rauber et al 1991; Szumowski et al. 1997; Szumowski et al. 1998; Szumowski et al. 1999) have observed large drops in cells confined to at or below the melting level (~5 km), removing the possibility that ice contributed to the presence of large drops.

In their extensive work cataloging over 9000 hours of disdrometer data from across the globe, Gatlin et al. (2015) found, perhaps surprisingly, that large raindrops were actually more commonly found at tropical locations than subtropical or high-latitude locations. However, the vertical extent of the clouds (i.e., whether they were above the freezing altitude or not) and the location (land or ocean) were not considered in their study (several dendrometers were located on prominent land masses), so a portion of those large drops may arise due to melting hail and graupel, rather than warm rain. In the Joint Hawaiian Warm Rain Project (JHWRP), drops were observed in warm rain clouds off the coast of Hawaii that often exceeded 4 mm in diameter, with a maximum diameter of 8 mm (Beard et al. 1986; Rauber et al. 1991). Using aircraft disdrometer data and simple collection equations for raindrop growth, Beard et al. (1986) suggested that the high liquid water content in the region, combined with strong updrafts (~7-10 m s^{-1}), was sufficient to explain the formation of the large drops. Rauber et al. (1991) proposed a different mechanism for large drop formation, wherein raindrops circulated between the updraft and downdraft of a convective cloud, allowing extended periods of accretional growth of these drops with small cloud droplets. As the updraft weakened, the large drops then fell through the former updraft channel where smaller drops, which would have otherwise caused collisional break-up of the large drops, were largely absent.

Building on the JHWRP, the Hawaiian Warm Rain Project (HaRP) further investigated the warm rain processes leading to large drops. Szumowski et al. (1997), (1998) and (1999) explored the formation of these large drops. They found that, within a window as short as 15 minutes, shallow cells with intense updrafts (5-9 m s^{-1}) could produce drops as large as 8.5 mm in diameter. The formation of large drops was favored in low wind shear environments, where updrafts were not tilted significantly. In these cases, drops would remain suspended above or within the updraft, where liquid water content was high, and drops could grow rapidly. Furthermore, these updraft channels were also hypothesized to be relatively clear of smaller raindrops. This is possibly due to a sedimentation size-sorting mechanism, where large drops fall through the updraft while smaller ones are suspended aloft (i.e., Kumjian and Ryzhkov 2012), resulting in a "clean" channel for large drops to fall through, and lowering the likelihood of collisional break-up with smaller drops. In the sheared/tilted updraft case, large drops are deposited away from this "clean" updraft channel and may be prone to collisional breakup induced by collisions with smaller drops. This is consistent with part of the mechanism put forth by Rauber et al. (1991). They also found the large nucleating aerosols, such as those provided by sea spray, were precursors to large drop formation, providing a relatively large starting point for droplets to grow.

3.1.2 PISTON OBSERVATIONS

The Propagation of Intraseasonal Oscillations (PISTON) Field Campaign, which took place in the open waters of the western North Pacific during the late-summer and early-autumn of 2018 and 2019 (Sobel et al. 2020), provided an opportunity to observe warm rain cells (along with other types of oceanic convection) in detail. Onboard the R/V *Thomas G. Thompson* (2018) and R/V *Sally Ride* (2019) was the Colorado State University SEA-POL radar (Rutledge et al. 2019 a, b), a polarimetric weather radar which took measurements of precipitation for the duration of both cruises. Using data from SEA-POL, Chudler and Rutledge (2021) found that small, isolated convection (primarily composed of warm rain cells) were present in over 90% of the SEA-POL scans, and contributed 11% of the radar-measured rain volume.

An interesting feature which was frequently noted during PISTON was the tendency for isolated convection to contain small areas with extremely high values of differential reflectivity. An example of this phenomenon is shown in Figure 3.1. Differential reflectivity (Z_{dr}), defined as the logarithm ratio of the horizontally and vertically polarized radar reflectivities, provides a measurement of the reflectivity-weighted oblateness of drops within a radar volume, with positive values corresponding to drops which have a larger horizontal axis in comparison to the vertical axis. While small raindrops (< 1 mm in diameter) are nearly spherical ($Z_{dr} \approx 0$ dB), larger

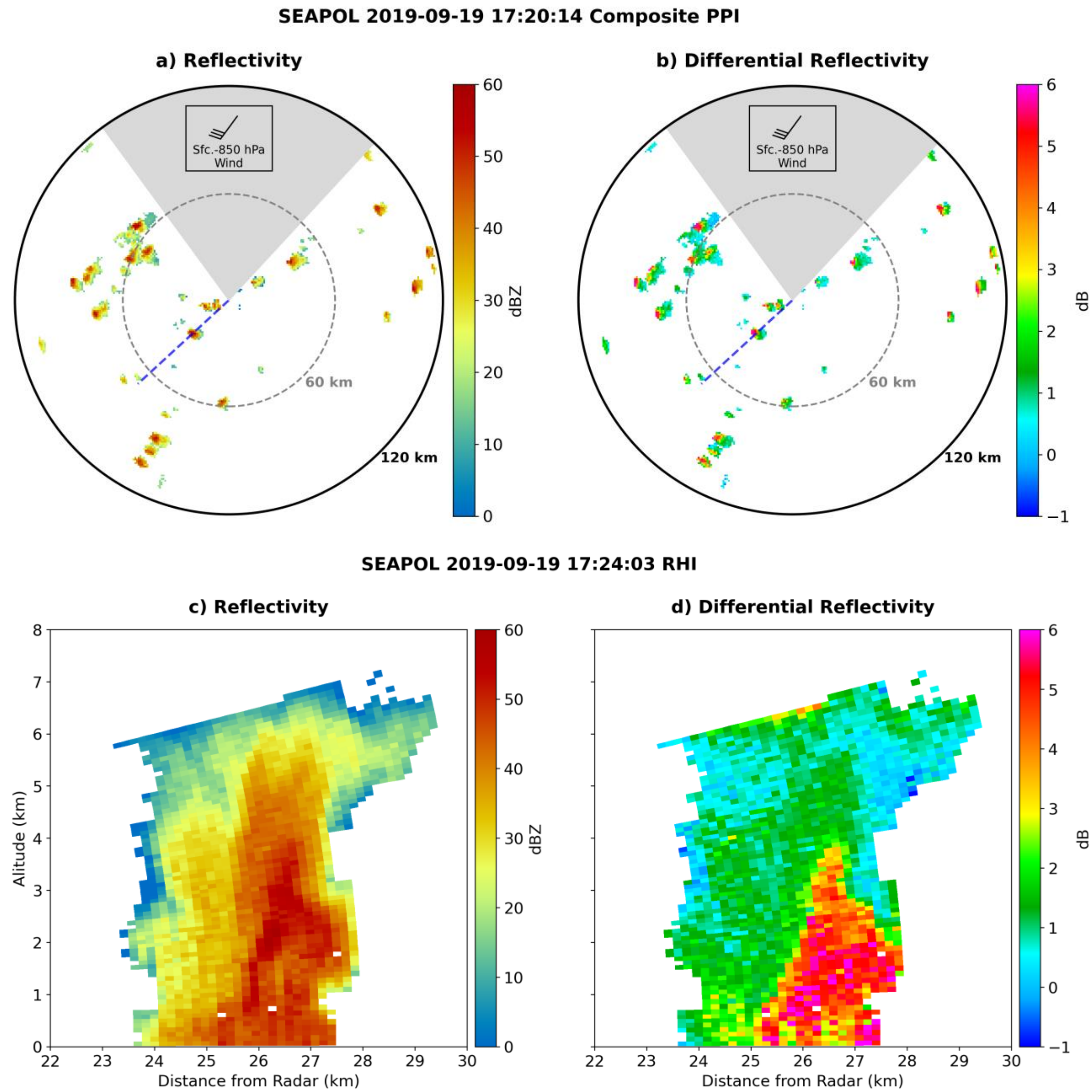

Figure 3.1: Example of cells with high-Z_{dr} seen by SEA-POL. PPI images in the top row provide top-down views of reflectivity (a) and differential reflectivity (b), and RHI images show vertical cross sections of the same variables in the bottom row (c, d). The location of the cross section plotted in the RHI images (c, d) is marked with a blue dotted line in the PPIs (a, b). The mean surface-850 mb wind vector is shown in (a) and (b), as determined from the radiosonde launch occurring closest to the SEA-POL scan time.

drops are distorted into oblate shapes (Pruppacher and Klett 1978), thus increasing Z_{dr}. During PISTON, cells with Z_{dr} in excess of 3.5 dB were frequently observed, and occasionally reached 7 dB or higher. The relationship between drop size and Z_{dr}, as calculated using T-matrix scattering simulations (Mishchenko et al. 1996) for a radar with the same frequency as SEA-POL's (5.65 GHz), is shown in Figure 3.2. The calculations for a 3 GHz S-Band radar are also plotted for comparison. For drop diameters below ~4.5 mm, in the Rayleigh scattering regime, Z_{dr} increases approximately linearly with drop size. Past this point, however, as drop size enters the Mie scattering regime for the 5.6 GHz radar (5 cm wavelength), a prominent spike in Z_{dr} is evident,

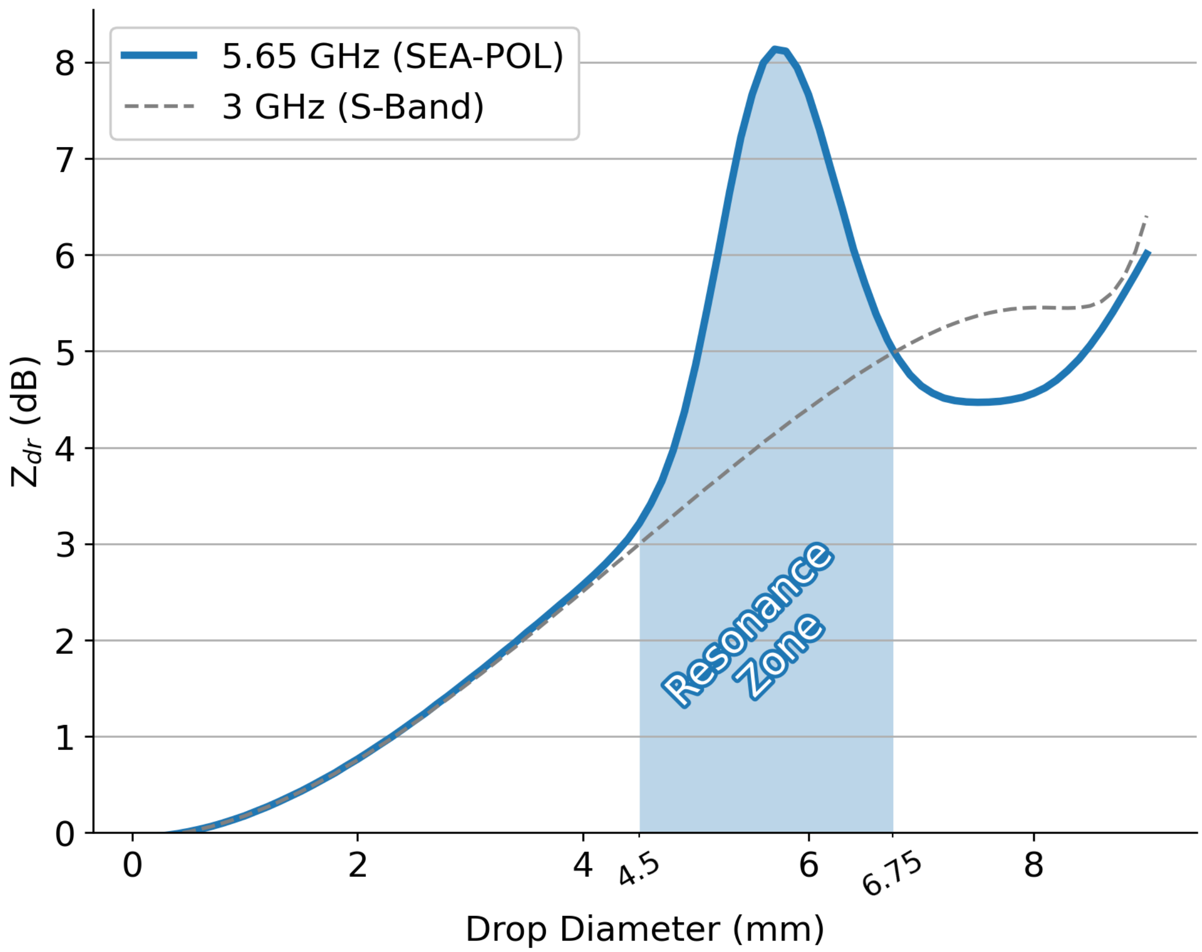

Figure 3.2: Simulated Z_{dr} vs drop diameter for SEA-POL (5.65 GHz, blue line) and a 3 GHz radar (dashed grey line). Z_{dr} values are calculated based on monodisperse drop distributions at a concentration of 10 m^{-3} mm^{-1}. Z_{dr} is calculated based on a water temperature of 20 °C and a mean canting angle of 0°, and a standard deviation of the canting angle of 10°. A "resonance zone" in marked between 4.5 and 6.75 mm, where Mie scattering effects lead to increased Z_{dr}.

caused by resonance effects (Bringi et al. 1991; Zrnić et al. 2000; Carey and Petersen 2015). This Mie scattering artifact makes the extreme Z_{dr} values observed in rain more readily explainable, as values of over 7 dB would be highly unlikely in a Rayleigh scattering regime (with the exception of insects, which are very unlikely over the open ocean). However, even after accounting for Mie scattering, Z_{dr} values of over 3.5 dB still suggest drop sizes in excess of 4.5 mm, which again is a curious feature in tropical warm rain cells. The region between 4.5 and 6.75 mm in Figure 3.2 is referred to as the "resonance zone", marking where Mie effects lead to a non-linear increase in Z_{dr}. In fact, Mie resonance effects extend beyond 6.5 mm, but cause a decrease in Z_{dr}, so they are excluded for convenience. The size of 4.5 mm will serve as a general threshold for large drops in this study.

Although studies on large drops forming in warm rain are sparse (notably only from the JHWRP and HaRP studies discussed above), it appears that given the right conditions (i.e., high liquid water content, strong and upright updrafts, and large nucleating aerosols), large drops can form through warm rain processes alone, without the need for melting ice. While these studies outlined the possible mechanisms for large drop growth, they lack in continuous robust observations, which the present study seeks to build upon. First, the JHWRP and HaRP studies are based primarily on analysis of a few case studies. With over 7000 volume scans collected during ~70 days at sea, the SEA-POL dataset allows for a robust statistical analysis of the characteristics of these large drop-producing storms. Additionally, while Szumowski et al. (1997, 1998, 1999) also utilized a C-band radar in their analysis, it was a single-polarized radar, and subsequently only reflectivity and radial velocity was examined. The polarimetric products offered by SEA-POL, particularly Z_{dr}, provide a more direct measurement of drop size and shape, which is of central importance to this analysis. This study seeks to leverage the high-resolution and long-term polarimetric observations from SEA-POL to characterize warm rain cells, particularly those which develop high Z_{dr} cores.

3.2 Data and Methods

3.2.1 SEA-POL RADAR

The radar data used herein was collected by the Colorado State University SEA-POL radar, a polarimetric C-band weather radar designed for use at sea. This work primarily uses the 360° plan position indicator (PPI) scans, which were taken every 15 minutes in 2018 and every 10 minutes in 2019. These PPI scans were then interpolated onto a regular 300x300x15 km (x-y-z) grid, with grid spacings of 1 km in the horizontal and 0.5 km in the vertical. Convective/stratiform partitioning and rain rate were then calculated at each grid point, using the algorithms outlined in Steiner et al. (1995) and Thompson et al. (2018), respectively. In addition to the PPI scans, range height indicator (RHI) scans were performed in-between PPI scans, which are examined for a case study presented in this paper. These RHI scans provide vertical cross-section "slices" of echoes at high spatial resolution. During the 2019 operations, rapid RHI scans were the focus, with sweeps being separated by as little as 15 seconds. The storm target for the RHI scans was chosen at the discretion of the radar operator. Note that, unlike the PPI data, the RHI scans were not gridded and have been left in their native spherical coordinates. Also utilized in 2019 was a scanning strategy which was optimized for rainfall mapping. As this scanning strategy focuses on capturing the lower levels of storms, storms were occasionally not topped by the radar beam, and their vertical extents therefore not fully captured. Thus, data on the vertical structure of storms from PPI scans is more limited for 2019. A more detailed explanation of the scanning strategies employed during PISTON, as well as the rigorous quality-control process used on the data, can be found in Chudler and Rutledge (2021).

3.2.2 FEATURE DETECTION AND TRACKING

To identify and analyze the warm rain cells, the precipitation feature identification method outlined in Chudler and Rutledge (2021) was utilized. This method identifies and groups contiguous regions of reflectivity pixels greater than a specified threshold, and then attributes each of these "features" with statistics such as echo top height, maximum/mean reflectivity and rain rate, total area, etc. For the 2019 data, echo top heights were only calculated for storms which were had their full vertical extent captured by SEA-POL (see note in Section 3.2.1. For the present study only "isolated" features (those with a maximum horizontal dimension of less than 20 km) are examined (sub-MCS and MCS features are grouped into a single "non-isolated" category, and linearity is not considered). Additionally, while Chudler and Rutledge (2021) used the 2 km grid-level to identify and group features, the present study groups features based on composite reflectivity, or the maximum reflectivity observed throughout the vertical column at each horizontal grid point. This is done in order to align with the methods employed by the cell-tracking algorithm discussed in the subsequent paragraph. Sensitivity tests show that the overall feature statistics do not change significantly between using 2 km and composite reflectivity for identifying features, with a modest increase in average feature area being the most notable change.

While the feature identification method described above provides a method for identifying features in each SEA-POL scan, it has no way of deriving temporal continuity of features between scans. That is to say, a single cell which in reality persists between SEA-POL scans as a single entity will be identified as two separate features by the Chudler and Rutledge (2021) method. In order to glean information on the statistics of these cells throughout their lifetime, a different algorithm is desired. Toward that end, the Thunderstorm Identification, Tracking, Analysis, and Nowcasting (TITAN) cell tracking technique (Dixon and Wiener 1993) is utilized in the present study. Specifically, the TINT Python package (https://github.com/openradar/TINT) developed by Fridlind et al. (2019), which takes the TITAN algorithm and wraps it up into a convenient and computationally efficient Python program, is used for analysis herein. As modified for the present study, this algorithm takes two successive SEA-POL scans at time t_0 and t_1, identifies the features in each scan based on the Chudler and Rutledge (2021) method, and then attempts to pair features together between t_0 and t_1 based on phase correlation calculations for each feature, while also taking into account the previous motion of the feature. While the TINT package does provide a limited set of attributes of each feature in addition to tracking them, more detailed statistics were desired. Accordingly, the feature identification/characterizing code used in Chudler and Rutledge (2021) was merged with the TINT algorithm for this study, resulting in a robust database which provides the track and attributes of all features seen by SEA-POL throughout their lifetimes.

3.3 Statistical Results

3.3.1 GENERAL STATISTICS

The following section will discuss the general attributes of high-Z_{dr} cores (HZCs) and the convective cells that contain them. A HZC is defined as a cluster of Z_{dr} pixels within an isolated cell which is made up of at least five contiguous pixels of composite Z_{dr} > 3.5 dB. The five-pixel threshold was chosen to exclude spurious noise and non-meteorological sea clutter which occasionally led to very small regions of high Z_{dr}. The 3.5 dB Z_{dr} threshold was chosen as it is the approximate threshold at which Mie scattering effects commence, and is associated with drop diameters of ~4.5 mm (See Fig. 2). It should be noted that although there is a sudden jump in Z_{dr} around this diameter, this is due to the specific frequency (5.65 GHz) used by the SEA-POL radar, and has no particular physical significance in terms of drop size. Echoes on either side of this Mie scattering threshold may have drastically different Z_{dr} values, however their drop sizes may be relatively similar. The 3.5 dB threshold is somewhat arbitrary in that regard; however, it still serves as convenient marker for defining a cell that contains large drops.

Approximately one-quarter (24%) of the SEA-POL scans contained at least one HZC echo. Although on an individual basis isolated cells actually only rarely developed an HZC (2% of all isolated cells), the ubiquitous nature of isolated cells resulted in HZCs being present a significant portion of the time. Additionally, stronger isolated cells were more likely to contain an HZC – cells whose reflectivity exceeded 40 dBZ at some point developed an HZC 10% of the time, and cells with a maximum reflectivity over 50 dBZ had an HZC 34% of the time.

Figure 3.3 shows statistics on the duration, formation time, area, and height of HZCs. The vast majority of HZCs (> 80%) were short-lived, lasting less than 10 minutes (Figure 3.3a). In reality there is likely additional variability within the 0–10-minute bin in this histogram, however because horizontal scans were only taken every 10 (15) minutes in 2019 (2018), 10 minutes is the finest interval which can be resolved. Figure 3.3b shows the formation time of HZCs, defined as the time between the formation of a given isolated cell, and the time at which an HZC was first observed. The majority (65%) of HZCs appeared in 20 minutes or less after cell initiation, or within 1-2 SEA-POL scans.

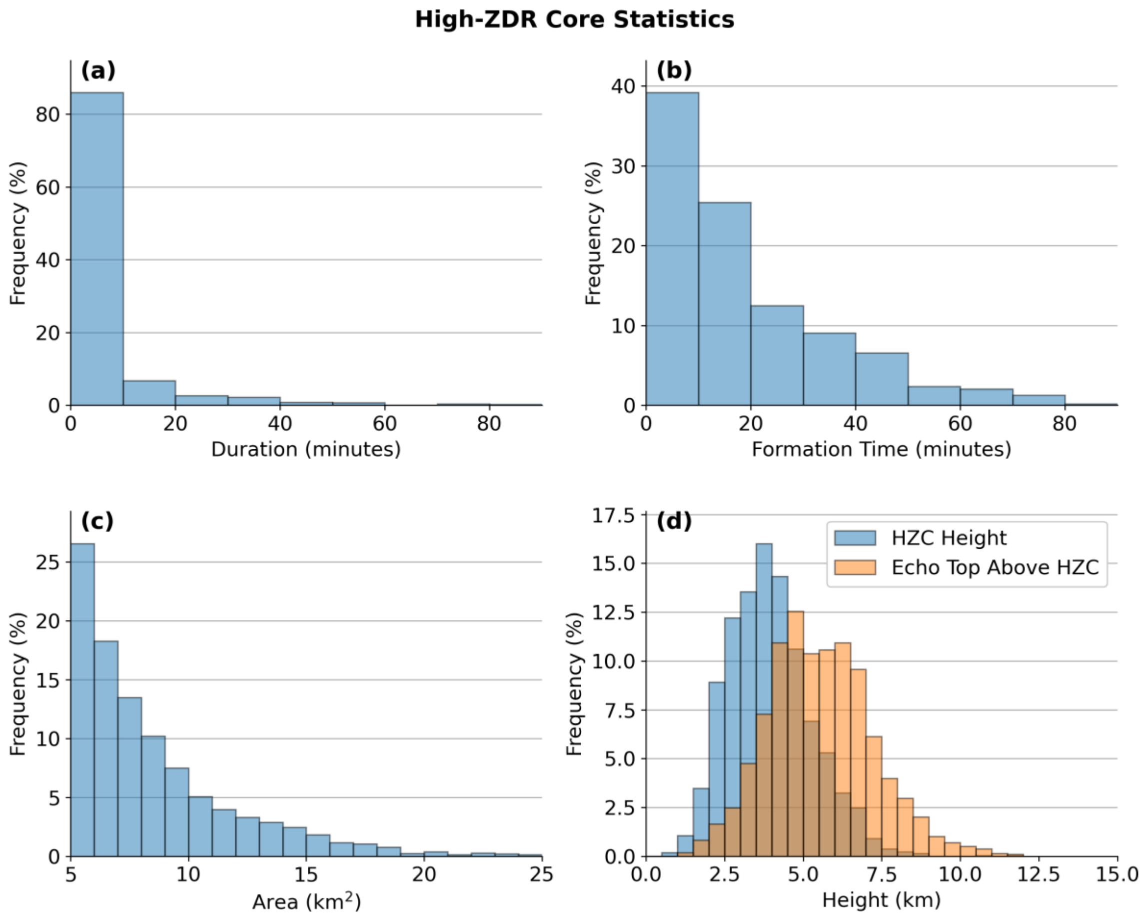

Figure 3.3: Duration (a), formation time (b), area (c) and height (d) of high-ZDR cores (HZCs). The bottom-right panel (d) shows both the height of the HZC (blue bars) as well as the maximum height of reflectivity above the HZC (orange).

The majority of HZC's were quite small, with a mean area of 8 km^2. By definition (described in the preceding paragraph), 5 km^2 is the smallest possible HZC size (owing to the interpolation grid size), so it is the smallest bin size used here. Figure 3.3d shows both the height of HZCs (blue bars) as well as the height of reflectivity echo tops above the HZCs (orange bars). The majority of HZCs were shallow, with a mean height of 3.7 km, with 87% of the HZCs topping out at or below the freezing level (5 km). The reflectivity above the HZCs was also typically shallow, and on average extended 1.6 km above the HZC. However, it should be noted that approximately half of isolated cells with HZCs had reflectivity echo tops which extended above the freezing level. This brings us to an important distinction. While a warm rain cell is technically defined as a cell which is confined entirely below the freezing level (Glickman et al. 2000), this is different from a cell which exhibits warm rain *processes*. That is to say, even in a cell which has some cloud mass in a sub-freezing environment, and therefore could contain ice, there may still be substantial collision-coalescence drop growth (Johnson et al. 1999; Lau and Wu 2003). This is particularly true in the tropics, where liquid water contents are substantial and warm cloud depths are large. Johnson et al. (1999) argued that cumulus congestus clouds (defined as radar echoes with tops between 4.5 and 9.5 km) may not fully glaciate until reaching temperatures of around -15 °C, and that significant amounts of supercooled liquid water can exist in these clouds at temperatures between -10 and -15 °C. When the cells are very short lived, as was evidenced in Figure 3.3a, this likely reduces the probability of freezing even further. For these reasons, HZCs within isolated cells which extend above the freezing altitude will be treated the same as those in pure warm rain clouds for the purposes of this paper. While we acknowledge that some ice and freezing/melting may exist in these storms, we argue that warm rain processes are the predominant mechanism for rain production in most cases.

3.3.2 HZC CELL STRUCTURE

Figure 3.4 shows the location of HZC pixels in isolated cells relative to the wind direction. For this analysis, the upwind/downwind "edge" of a cell was defined as the furthest upwind/downwind point from the cell center with a reflectivity greater than or equal to 17 dBZ (the same threshold used for feature identification). Wind direction was determined from the sounding which was launched nearest to the time the cell was observed. Each vertical radar grid level was considered independently and matched to the wind direction at the closest vertical

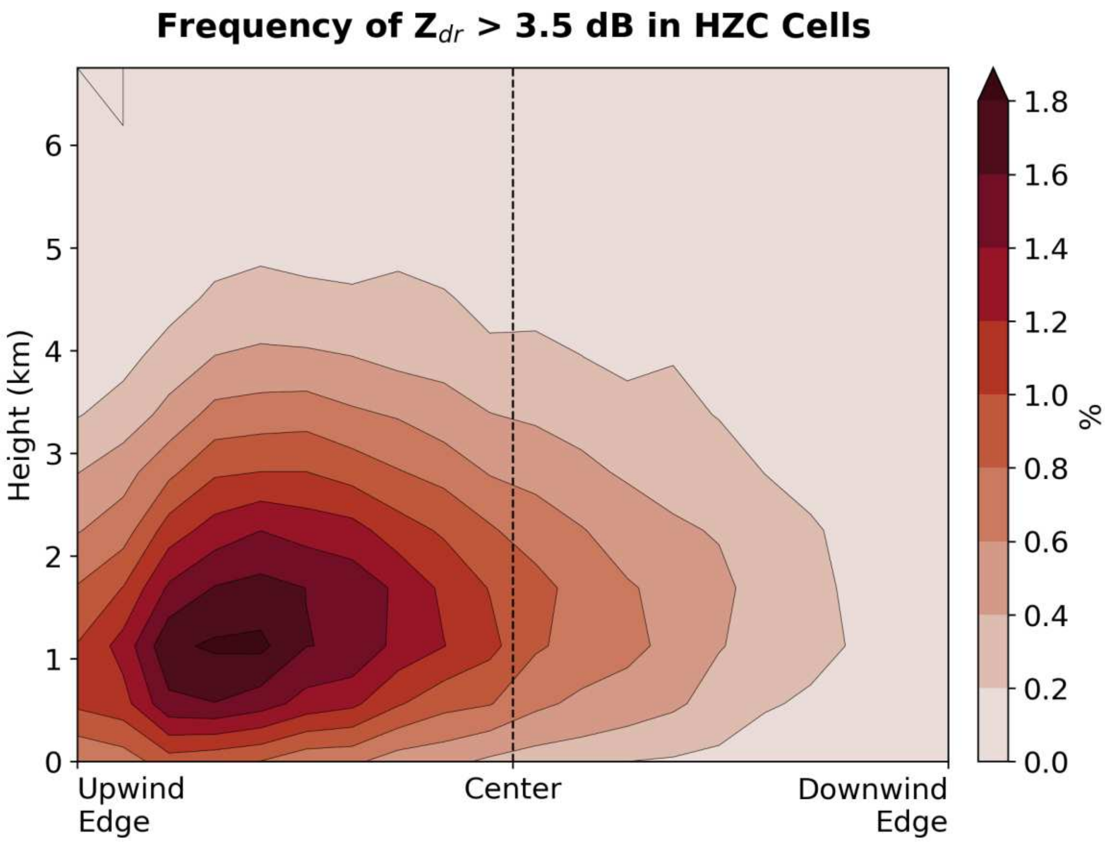

Figure 3.4: Heatmap of the location pixels with high Z_{dr} within HZC cells. The center is calculated as the center-of-mass of all pixels (not weighted by reflectivity) within the cell, and edges are defined as the furthest upwind/downwind point from center.

sounding level. High Z_{dr} pixels were primarily found on the upwind side of cells, with 75% of high Z_{dr} pixels located upwind of the echo center. We hypothesize that this pattern is caused by size sorting, wherein the horizontal advection of smaller drops is more substantial than large drops. As drops begin to grow and the drop size distribution within the cell broadens, the smaller drops are transported downwind, leaving mainly large drops on the upwind side. This would result in enhanced Z_{dr} on the upwind side.

Although high-Z_{dr} frequency appears to decrease on the downwind side of these cells, this does not necessarily mean that the large drops are entirely absent there. Despite the fact that reflectivity is proportional to the sixth power of drop diameter, and therefore Z_{dr} will be strongly influenced by the largest oblate drops, in the case where a high number concentration of small drops is mixed with a very low concentration of large drops, the Z_{dr} signal can be dominated by the quasi-spherical smaller drops, producing a smaller Z_{dr}. Hence, it, is possible that the large drops may still exist in regions of more modest Z_{dr}. High-Z_{dr} values may only arise when/if the size sorting mechanism discussed above isolates the large drops by themselves on the upwind side, and masks the high Z_{dr} signal on the downwind side by locally increasing the concentration of small drops. This effect of small drops masking the high-Z_{dr} signal of large drops is investigated further in Section 3.3.3.

Looking now at vertical structure, Figure 3.4 shows that HZC pixels were more frequently found in the lower levels of echoes, with a maximum around 1 km. Below 1 km the frequency drops off, although this is likely due to under sampling as a result of the radar-beam overshooting the near-surface levels at far ranges. The increase in high Z_{dr} frequency with lower altitudes may be due to a couple reasons. As the drops fall from cloud top, they likely continue to grow through collision-coalescence and increase in size, which would lead to a higher Z_{dr}. Additionally, the temperature of the raindrops may also play a significant role given the sensitivity of the dielectric constant to temperature. At higher temperatures, the spike in Z_{dr} in the Mie scattering region Figure 3.2 is larger, so the increase in high-Z_{dr} pixel frequency at low levels may also be attributed to the warmer temperatures nearer to the ocean surface. (This temperature effect is discussed further in Section 3.3.3.

Figure 3.5 shows the structure of radar variables within HZC cells. The overall picture is consistent with the idea of a cell with drops which have been sorted such that only large drops remain on the upwind side. Note that while the maximum in Z_{dr} occurs at the far upwind edge,

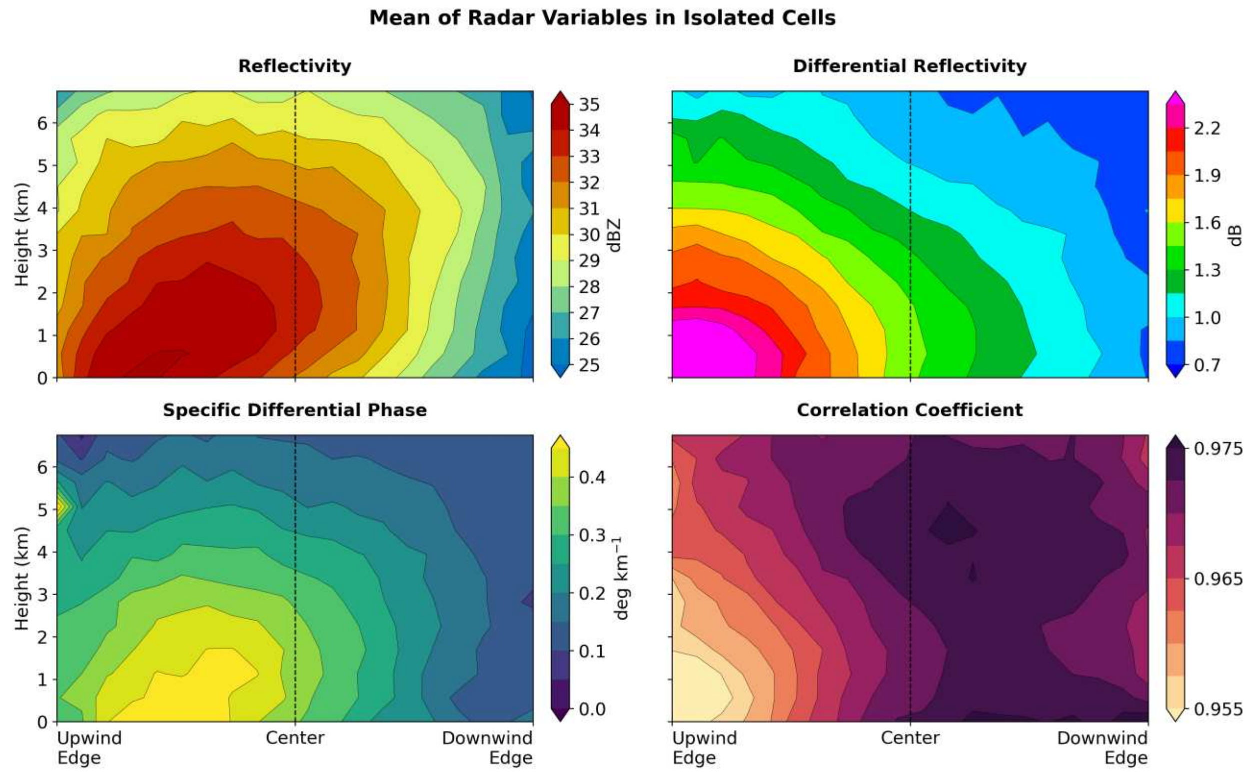

Figure 3.5: As in Figure 3.4, but looking at the mean values of reflectivity (a), differential reflectivity (b), specific differential phase (c), and correlation coefficient (d). Each panel also shows the mean rain rate at each horizontal bin (green line, annotated with rain rate values in mm hr^{-1}).

the maximum in specific differential phase (K_{dp}) is displaced further downwind. Because K_{dp} is proportional to total liquid water content and mass weighted oblateness (Bringi and Chandrasekar 2001), the fact that the Z_{dr} maximum lies in a region of lower K_{dp} suggests that the far upwind edge of these HZC cells is composed of very large drops, but at low concentrations, constituting small liquid water contents. Correlation coefficient (ρ_{hv}), a measurement of the homogeneity (or lack thereof) of scatterers within a beam volume, is also at a minimum at the far upwind edge. These depressed values of ρ_{hv} are likely due to increased values of backscatter differential phase caused by raindrops with diameters well into the Mie scattering region. In these situations, ρ_{hv} can be as low at 0.93 at C-band as discussed by Ryzhkov and Zrnic (2019).

Furthermore, oblate drops may oscillate as they fall, which would further reduce ρ_{hv} (Kumjian and Ryzhkov 2012).

Vertically, the upwind edge shows an increase in Z_{dr} as altitude decreases. This again demonstrates the possible impact of drop growth as well as increasing temperature on Z_{dr}, As drops fall, they warm and continue to grow, both of which enhance Z_{dr}. Sedimentation size sorting, wherein large drops fall out quicker compared to smaller ones (Kumjian and Ryzhkov 2012) may also be playing a role.

Further downwind, significant concentrations of smaller drop sizes begin to mix in, leading to maxima in reflectivity and K_{dp}, while Z_{dr} begins to decrease either due to the masking effect discussed previously, or due to absence of large drops. Moving past the center to the downwind side, reflectivity, K_{dp}, and Z_{dr}, all decrease as ρ_{hv} increases. This suggests that the downwind side of HZC cells are composed primarily of light rain or drizzle with near uniform quasi-spherical drops, potentially blown in from the upwind side.

3.3.3 SCATTERING SIMULATIONS

We now explore the theoretical basis for some of the observations of HZCs described above. This section will investigate simulated Z_{dr} for given drop size distributions, calculated using the PyDSD software package (https://github.com/josephhardinee/PyDSD). As discussed above, it is hypothesized that large drops may exist outside of high-Z_{dr} regions due to the masking effect of small drops. This is demonstrated in Figure 3.6, which shows the simulated Z_{dr} of large drops

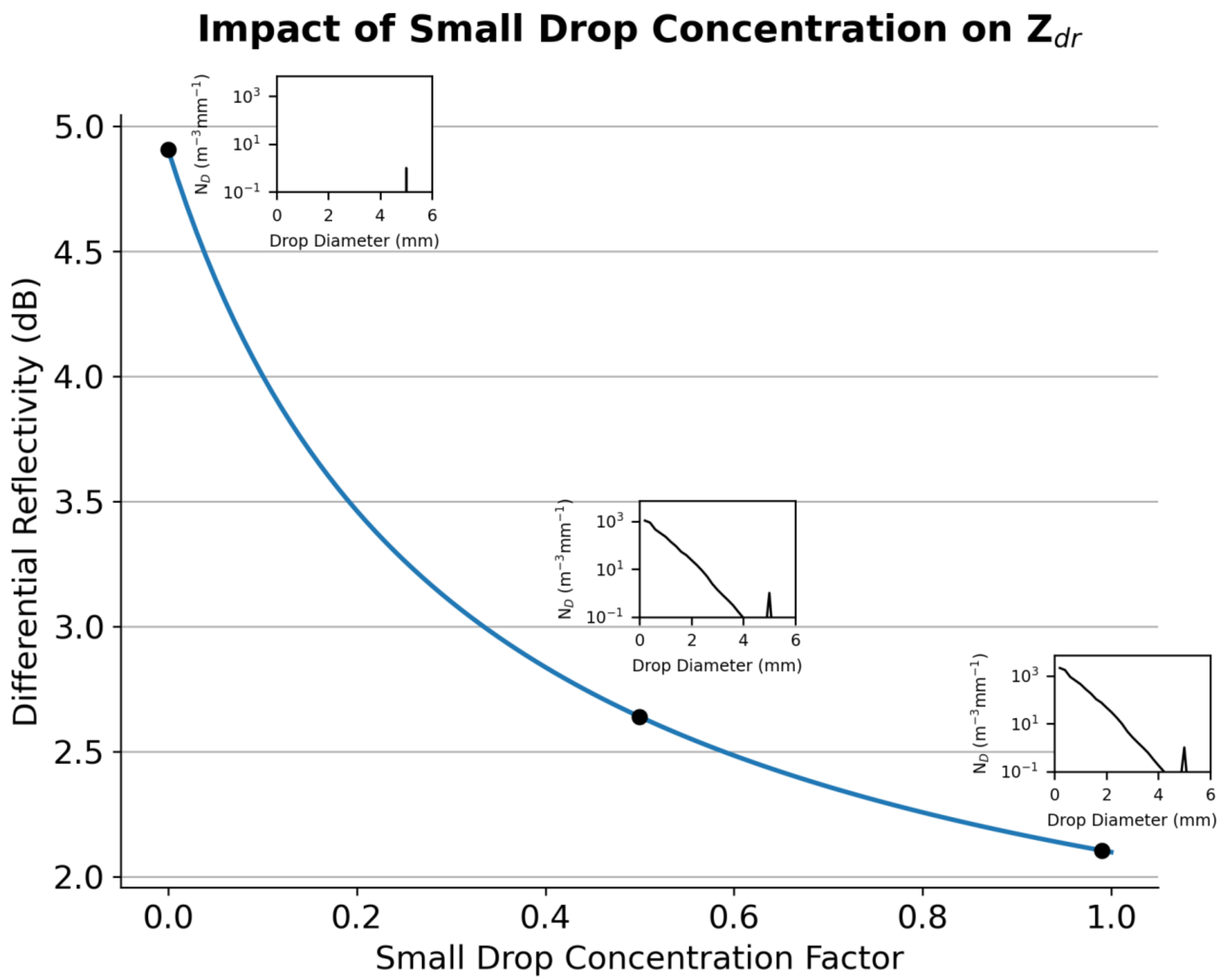

Figure 3.6: Calculated Z_{dr} vs concentration of small drops. Baseline small drop concentration factor was determined by averaging disdrometer data from cells with light-to-moderate rain, and then multiplied by a "concentration factor" on x-axis and combined with a set concentration of large (5 mm) drops. Inset plots show the drop distribution at selected points along the line. Calculations were performed for a radar with a SEA-POL frequency (5.65 GHz), with all of the same scattering parameters outlined in the caption of Figure 3.2.

mixed with varying concentrations of small drops. For these calculations, two years of data from the two-dimensional video disdrometer located at the U.S. Department of Energy Atmospheric Radiation Measurement Program site on Manus Island, Papua New Guinea were used to create a baseline "small drop" concentration (Thompson et al. 2015). To represent the typical drop size distribution which may be associated with convective cells, all record times which logged a rain rate of > 10 mm hr^{-1} and a Z_{dr} of < 2 dB were averaged into a single distribution. This baseline distribution was then multiplied by various concentration factors from 0 (no small drops used) to 1 (entire small drop concentration used), and "mixed" with 5 mm drops with a fixed concentration of 5 m^{-3} mm^{-1}. This large drop size and concentration was chosen to be consistent with the findings of the HaRP project (Szumowski et al. 1997, 1998, 1999), and also agree with the findings of in-situ aircraft disdrometer measurements from PISTON (see Section 3.4.1). When no small drops are included in the scattering calculations (left side of Figure 3.6), the simulated Z_{dr} is nearly 5 dB, similar to what was observed by SEA-POL on the upwind side of the HZC cells. However, as small drops are mixed in, Z_{dr} rapidly decreases. When the full small drop concentration is applied, Z_{dr} drops to ~ 2 dB. This finding suggests that even when the Z_{dr} in tropical convection is measured at more typical levels (1-2 dB), this does not preclude the existence of large drops in that same radar volume.

It was also noted previously that the frequency of high-Z_{dr} pixels was higher at lower altitudes, where temperatures are generally higher. Figure 3.7 shows the sensitivity of Z_{dr} scattering calculations to water drop temperature due to the dielectric effect. In the Mie scattering regime, temperature has a significant impact on Z_{dr}. For example, a 5.5 mm drop at near-freezing temperatures would have a Z_{dr} of 5.5 dB, while a drop at 25 °C (the approximate surface mean wet-bulb temperature during PISTON) would have a Z_{dr} of 8.3 dB. As drops fall and warm, their Z_{dr} may increase even if their size remains constant. This effect could partially explain the increase in the frequency of high-Z_{dr} pixels at lower altitudes.

3.3.4 DROP GROWTH

This section will investigate the growth of drops in tropical warm rain under different microphysical regimes. Following the methods of previous studies (Beard et al. 1986; Szumowski et al. 1997; Szumowski et al. 1998; Szumowski et al. 1999), a simple continuous collection equation will be used to simulate droplet growth:

$$\frac{dr}{dt} = \frac{V_r W_l E_c}{4\rho_l} \tag{3.1}$$

where V_r is drop fall speed, W_l is the liquid water content, E_c is the collection efficiency, and ρ_l is the density of water. V_r is derived from the Gunn and Kinzer (1949) drop terminal velocity experiments, and E_c is a function of drop size, interpolated from Yau and Rhodes (1996, Table

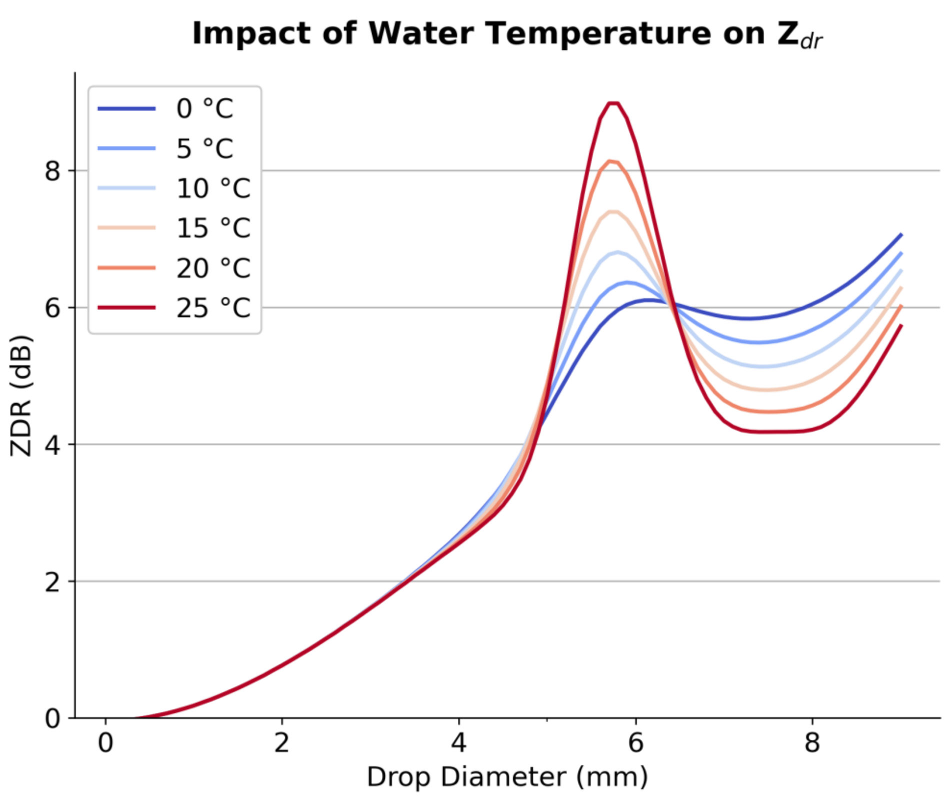

Figure 3.7: As in Figure 3.2 but calculated for different water temperatures.

8.2). Drops were initialized with an initial diameter of 20 μm (comparable to the size of a nucleating sea salt aerosol, Woodcock 1953; Szumowski et al. 1991), and released into an environment with some prescribed constant updraft speed and liquid water content (LWC). Equation (3.1 was then integrated forward with a time step of 30 seconds, and continued until the drops returned to the initial height they were released at, assumed to be cloud base.

Figure 3.8 shows the growth trajectory of a water drop under varying background LWCs. In all LWC scenarios, large drops (> 4.5 mm) formed by the time the drop exited cloud base.

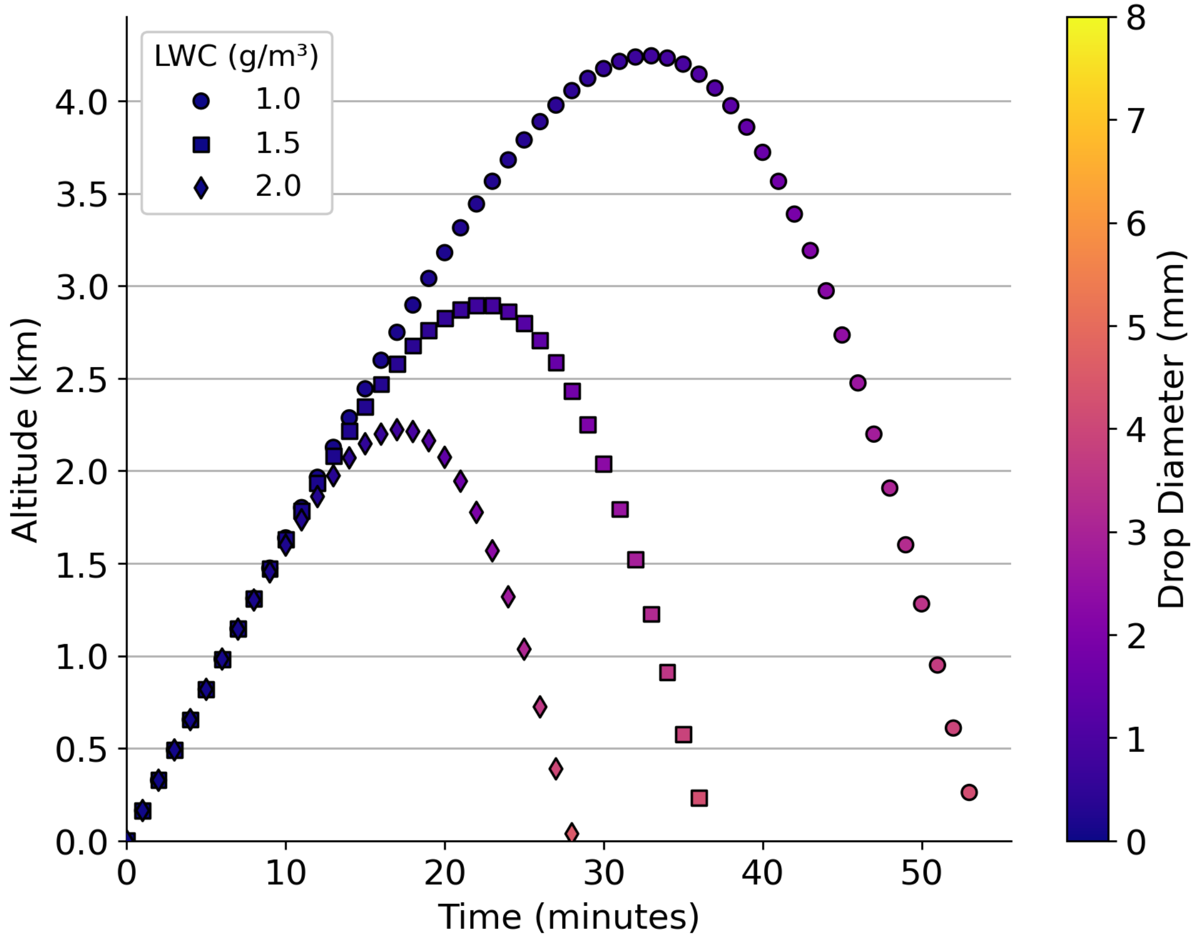

Figure 3.8: Time series of drop growth using the continuous collection equation under different background liquid water contents (LWC). A constant updraft speed of 3 m s^{-1} was used in these calculations.

Interestingly, the final drop diameter for all LWC scenarios is approximately equal. Although drops do grow more slowly in low LWC conditions, slower growth allows them to be lofted higher in the cloud. Therefore, the slow growth rate at low LWCs is offset by a longer cloud residence time, and the final drop size is similar. However, at a LWC of 1 g m^3, it takes nearly a full hour for the drop to exit the cloud. The majority of HZC cells observed during PISTON formed in 20 minutes or less (Figure 3.3), so this suggests that high cloud LWCs (> 2 g m^{-3}) must have been commonly present during PISTON operations. While Szumowski et al. (1998) generally found that LWC values were less than 1.5 g m^{-3} during HaRP, they suggest that this may be an underestimate due to instrument limitations. Additionally, aircraft observations of HZC cells during PISTON (discussed in Section 3.4.1) observed LWC's > 2 g m^{-3}, so this is a reasonable value to expect. Drop sizes at the highest point of these trajectories are all around 0.8 mm, which is close to the 1 mm drops at cloud top observed by Szumowski et al. (1998).

Figure 3.9 shows similar drop growth trajectories, but calculated for different updraft speeds while holding LWC constant at 1.5 g m^{-3}. Generally, as updraft speed increases, the final drop size upon exiting cloud base increases. While a 1 m s^{-1} updraft is too weak to support large drop formation (final drop size is less than 1 mm in this scenario), stronger updrafts of 3 and 5 m s^{-1} were found to produce drops of 4.2 mm and 10 mm, respectively. The latter is probably unrealistically large, and arises due to the limitations of this simple model (for example, breakup is not considered). In reality, a 5 m s^{-1} updraft would be unlikely to last for 50+ minutes as is shown in this plot, and the drop would probably not remain within the updraft core for that entire time even if it did. During PISTON, HZC cells had echo tops as low as 3 km. This is approximately the maximum elevation reached by the drop in the 3 m s^{-1} updraft scenario. Evidently, with this

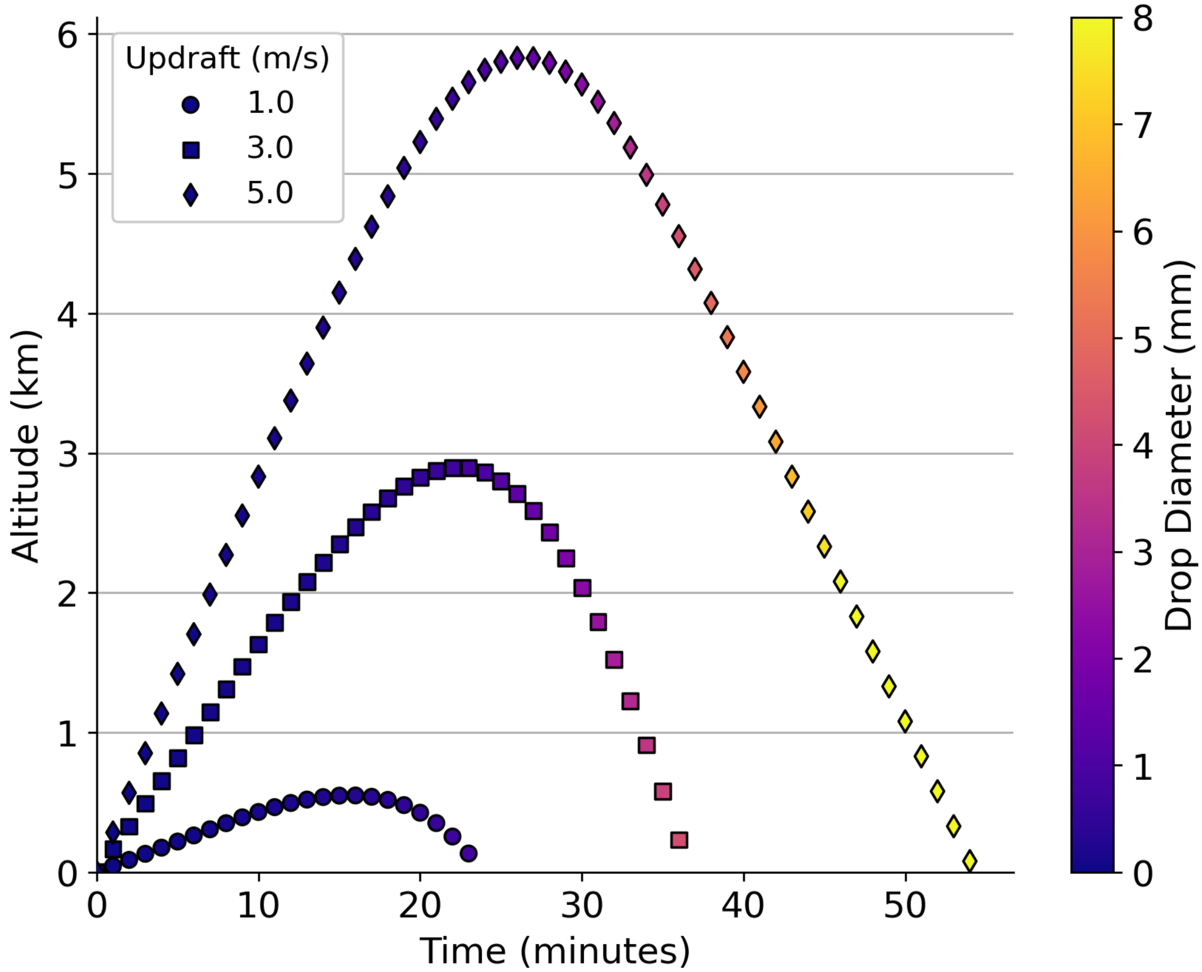

Figure 3.9: As in Figure 3.8, but with varying updraft speeds and liquid water content held constant at 1.5 g m^{-3}.

simple model, a LWC of 1.5 g m^{-3} and an updraft speed of 3 m s^{-1} is sufficient to explain the formation of 4.5 mm drops in very shallow convection.

3.3.5 HZC CELL LOCATION

To this point, only HZCs observed within small, isolated convective cells have been considered. However, HZCs did occasionally occur in the convective portions of larger, more organized precipitation features. The following section will address this.

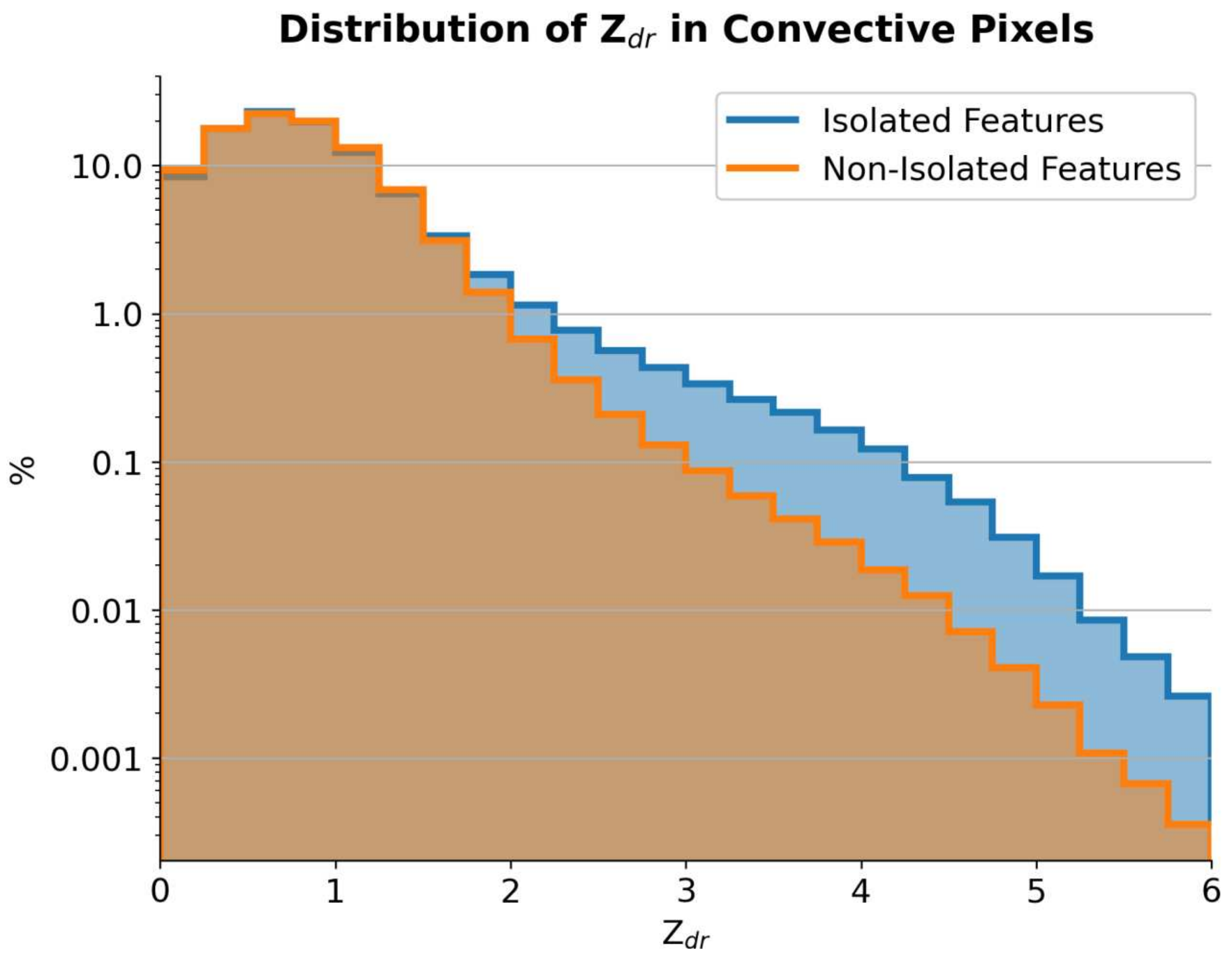

Figure 3.10: Distribution of differential reflectivity (Z_{dr}) within convective pixels for isolated (blue) and non-isolated (orange) pixels, as classified by the Steiner et al. (1995) algorithm. Distribution has been plotted on a log-Y axis to emphasize the differences at the extreme right tail.

Figure 3.10 shows the distribution of Z_{dr} values in convection for isolated and non-isolated features. To emphasize the differences in the tail of the histogram, which makes up a relatively small fraction of the overall distribution but is the primary interest of this study (large Z_{dr}), a log-Y axis is used in this plot. Large Z_{dr} values are much more common in isolated cells compared to non-isolated cells. Convective elements within the larger precipitation features are typically deeper and longer lived, meaning ice and freezing/melting processes may be present in these features. Recall that for large drops to form, it is hypothesized that a “clean” updraft channel is required (Rauber et al. 1991, Szumowski et al 1999), free of any small drops which would otherwise cause collisional break-up of the large drops. If extensive ice mass exists within the sub-freezing portion of a convective core, as this ice melts and falls to lower levels, it may prevent a "clean" channel from existing, and therefore preclude the formation of larger drops, or work to reduce their presence due to collisional breakup. Another possibility is that large drops do exist in larger convective systems, but the drop size distribution in these cases contain a higher number of smaller drops, which could mask the high Z_{dr} signature (as discussed in Section 3.3.3).

However, as was mentioned previously, large, organized features did occasionally contain HZCs, despite extensive amounts of ice and melting existing within the feature. One clue as to how this may happen lies within the location of HZCs within these features. Although it is not directly quantified in the present study, in general it was noted that HZCs within MCS during PISTON typically occurred on the leading convective edges. An example of this is provided in Figure 3.11. The convective line on the leading edge of this southward-propagating MCS is dotted with numerous individual HZCs. Although high reflectivity values exist elsewhere in the storm, only the extreme southern edge of the leading line has any high-Z_{dr} signal. The convection here is young, relatively shallow, and removed from the extensive region of stratiform (and associated ice processes) behind it. Strong updrafts along the leading edge (likely associated with cold pool propagation) are evidently enough to initiate the formation of large drops.

3.4 Case Studies

3.4.1 LEARJET OBSERVATIONS

During the 2019 PISTON campaign, collaborative operations were performed with the Cloud, Aerosol and Monsoon Processes Philippines Experiment ($CAMP^2Ex$,

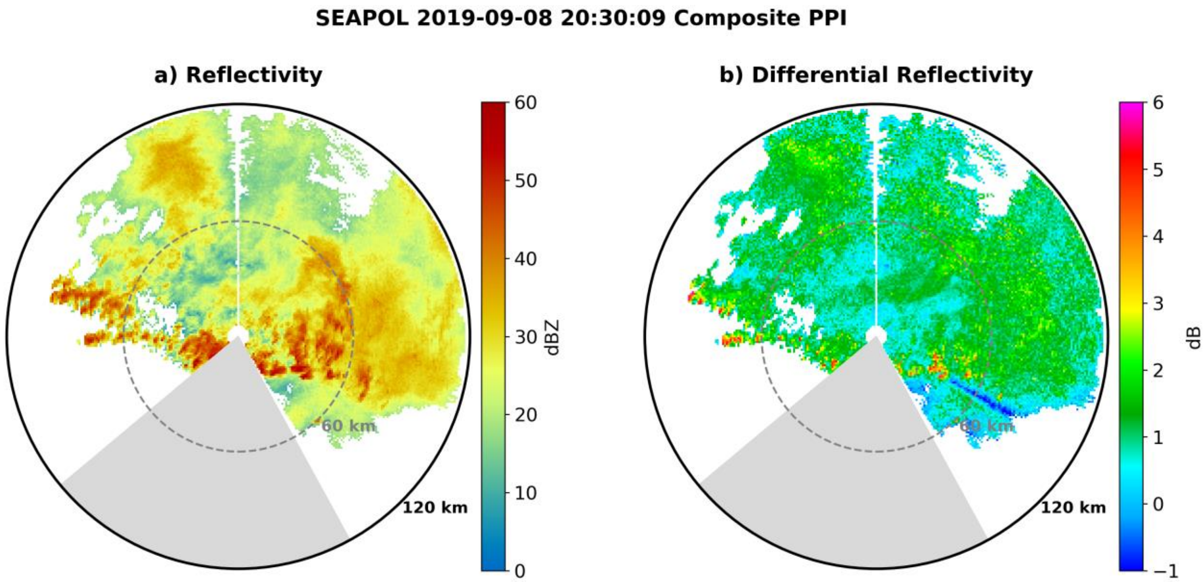

Figure 3.11: Example of a large convective system with areas high-Z_{dr} on the leading convective edge on the south side.

https://camp2ex.jpl.nasa.gov) project, which was ongoing in the same region that year. The CAMP²Ex field project involved multiple aircraft, including the SPEC Inc. Learjet, which was outfitted with a suite of state-of-the art particle probes (Lawson et al. 2015) capable of taking measurements of cloud/raindrop sizes and concentrations across a wide drop size spectrum. On September 10, the concurrent measurements of a HZC cell were made with both the SEA-POL radar and the Learjet particle probes (Figure 3.12). Although the cell was short-lived (< 30 minutes), the Learjet was able to make two passes through the upper and lower portions of the cell. Figure 3.12 shows a vertical cross section of the cell which was captured by SEA-POL near the time of the passes.

The drop size distributions recorded by the Learjet probes during each pass are shown in Figure 3.13. During the first pass through the upper portion of the storm, where Z_{dr} was 3-4 dB, the Learjet recorded drops up to 3.75 mm in diameter. This pass featured a very high LWC over

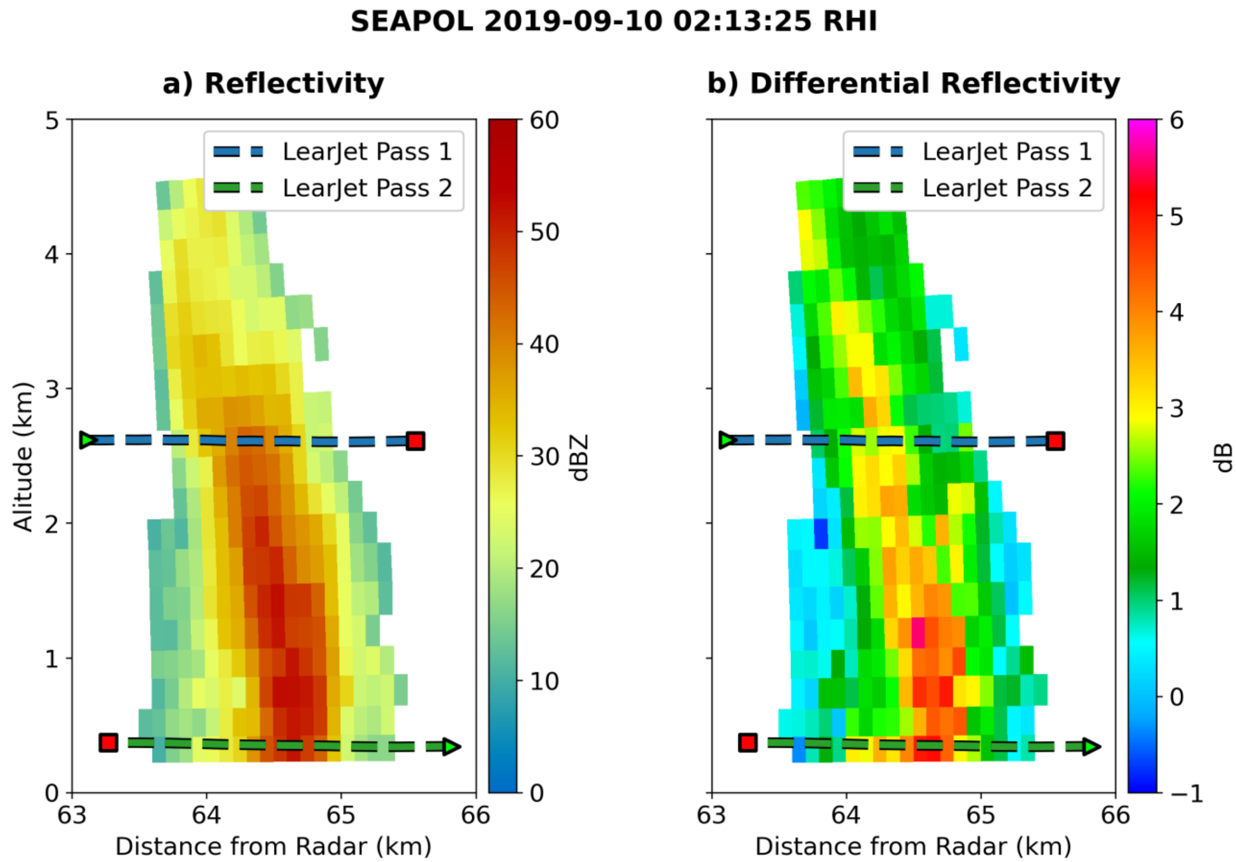

Figure 3.12: Vertical cross section of an HZC cell sampled by the Learjet aircraft. The dashed lines mark the path of the Learjet, which made two passes through the storm. The upper pass (blue) occurred at 02:13 UTC, and the lower pass (green) occurred at 02:16 UTC. The green triangle and red square markers denote the beginning and ends of the passes, respectively.

2 g m^{-3}, in part due to a very high concentration of small 10-50 μm cloud droplets. Szumowski et al. (1999) suggested that drop growth is most rapid in the near-suspension and early-fall period near the top of the cloud, which is certainly plausible in this case given the very high liquid water content. The slow drop fall speeds in this near-suspension phase may also preclude extensive collisional break-up from occurring, despite the high concentration of intermediate and small drops. Approximately 3 minutes later, the aircraft made a pass through a rain shaft below cloud base. Here, drops up to 4.5 mm in diameter were observed. This increase in drop size corresponds with an increase in Z_{dr} seen by SEA-POL (Figure 3.12b), with values over 5.5 dB measured near

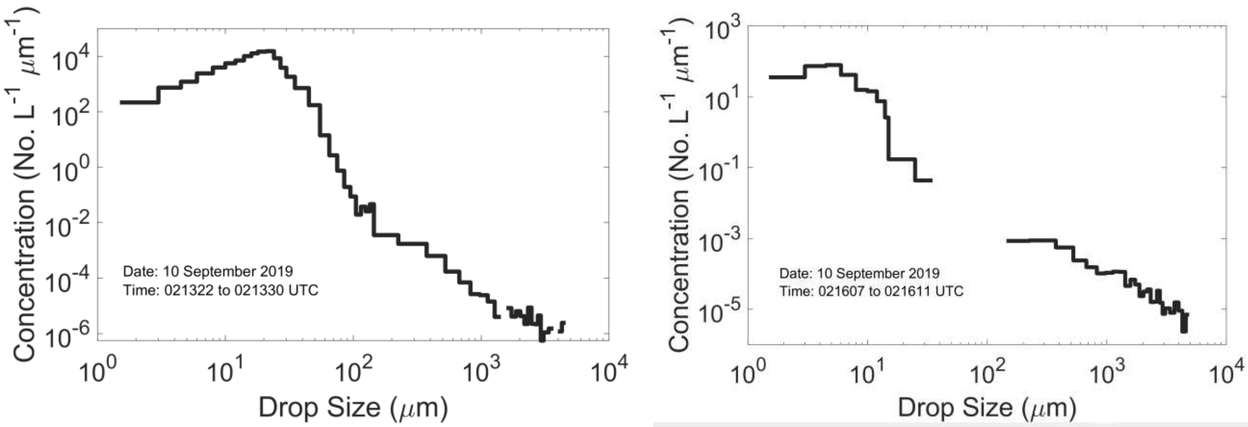

Figure 3.13: Drop size distribution measured by the Learjet particle probe during the flight paths drawn in Figure 3.12. Data in the left panel and right panels correspond with the upper and lower passes marked in Figure 3.12, respectively.

the lowest portion of the scan. Interestingly, during this pass there was only a very low concentration of small drops and no intermediate size drops. This dearth of smaller drop sizes could be indicative of a “clean” updraft channel, as proposed by Rauber et al. (1991) and Szumowski et al. (1998).

3.4.2 RAPID VERTICAL CROSS SECTION SCANS

During PISTON 2019 operations, focus was placed on capturing the vertical evolution of storms at a high temporal resolution. Toward that end, rapid vertical cross sections were obtained between horizontal scans. With this scanning method, high-resolution vertical cross-sections of storms could be captured as frequently as once every 15-30 seconds. In practice, the rapid formation and decay of isolated cells, along with the motion of the ship, proved to make capturing the evolution of an HZC quite difficult. However, on days where storm motion was very slow and the ship was stationary, this task was feasible. The following section examines the evolution of one HZC cell on which rapid vertical scans were successfully obtained.

On September 22, 2019, rapid successive vertical cross sections were taken of a small, isolated cell near SEA-POL (Figure 3.14). This cell was very small – approximately 1 km wide and only 3 km in height. Despite its diminutive size, at its peak SEA-POL observed a reflectivity of 57 dBZ and Z_{dr} in excess of 10 dB (recorded near the surface where temperatures were approaching

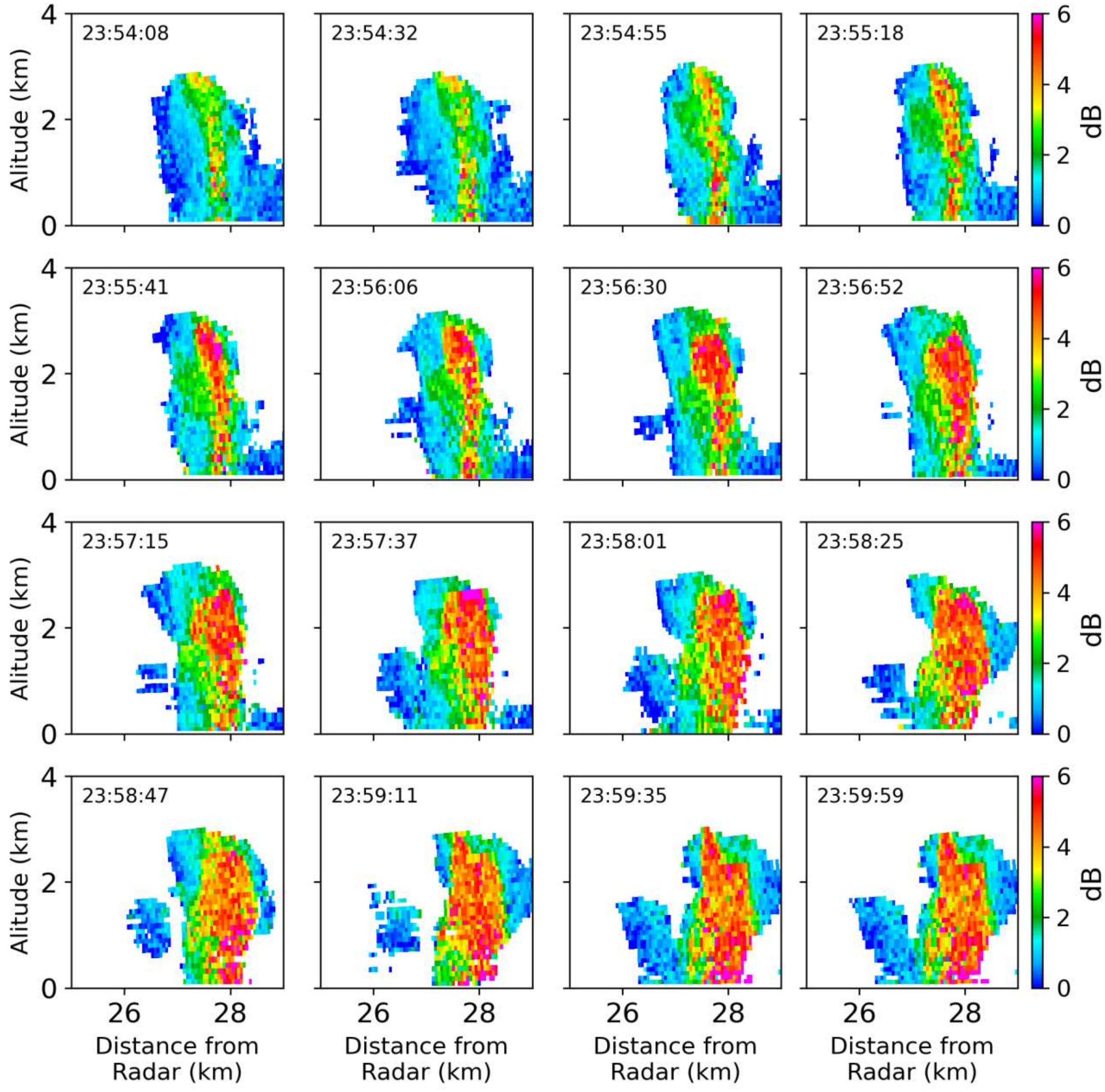

Figure 3.14: Vertical cross sections of Z_{dr} showing the evolution of a HZC cell, captured using rapid vertical cross section scans from the SEA-POL radar. The timestamp in the upper left corner of each plot marks the start time of each scan.

30 °C). It is worth recalling here that the relationship between drop size and Z_{dr} is nonlinear, and that higher Z_{dr} does not necessarily mean larger drops are present. In fact, beyond a drop diameter of around 5.7 mm, Z_{dr} actually begins to decrease (see Figure 3.2). Rather, the Z_{dr} response is greatest in a "resonance zone" between ~4.5-6.75, and an increase in Z_{dr} should be interpreted as an increase in the concentration of drops in this size range, or a decrease in the concentration or smaller drops which would otherwise have a masking effect (Section 3.3.3).

At the time of the first scan (23:54:08 UTC, top left of Figure 3.14), a HZC had already began to form, with a very narrow (~300 m) channel of 2-4 dB Z_{dr}, presumably corresponding to the location of the updraft. As time progressed, Z_{dr} increased, with the largest Z_{dr} values appearing at the top of the cell first. By 23:55:41 UTC, Z_{dr} values up to 6 dB were located at the top of the cell, while Z_{dr} in the remainder of the column was still primarily in the 3-4 dB range. This Z_{dr} maximum at cell top then began to cascade downward, as well as expand horizontally. By 23:58:47 UTC, the large Z_{dr} values reached the surface, including values in excess of 10 dB. Overall, these snapshots demonstrate a scenario in which drops undergo rapid growth at the top of the updraft (Z_{dr} increasing from 3 to 6 dB in ~90 seconds). The large drops could then no longer be supported by the updraft (either due to their increase in mass or a decrease in updraft intensity, or both), and began to fall towards the surface. As they fell, Z_{dr} continue to increase, likely due to some combination of continued coalescence and temperature effects. Near the surface, Z_{dr} exceeded 10 dB at a few localized points, suggesting radar volumes which were composed primarily of very warm (25 ° C, the approximate wet bulb temperature) drops in the Mie resonance range (4.5-6.75 mm), with few or no small drops. We note that in the simple drop growth model presented in Section 3.3.4, drops only obtained a diameter of ~0.8 mm at cloud top. These are much smaller than the drops at cloud top in the RHIs presented here, which are evidently large enough to induce Mie scattering and high Z_{dr} values. Rapid drop growth at cloud top may be a result of rapid collection or small drops suspended above the updraft, or even a recirculation of drops (e.g., Rauber et al. 1991), both of which are not accounted for in the simple collection model.

This vertical evolution of Z_{dr} values is also represented in Figure 3.15, which depicts the 90th percentile of Z_{dr} values at each level for each scan in Figure 3.14. Initially, Z_{dr} is close to uniform throughout the column, with values generally between 2-3 dB. As time progresses, Z_{dr} increases throughout the column, but with the largest increase near cell top, where values up to 5-6 dB begin to appear, and decreasing to 3-4 dB near the surface. At the end of the scanning period, Z_{dr} remains very high at cell top (5 dB), but the largest Z_{dr} values are found near the surface (5-7 dB). Again, this demonstrates a Z_{dr} signal which is influenced multiple factors – drops which grow rapidly aloft and continue to grow as they fall, and increasing resonance/Mie effects as temperature increases with decreasing altitude.

The rate at which large drops formed in this case study (3-5 minutes) is much faster than what was predicted by the continuous collection in Sec. 3.3.4. One potential explanation for this is that while in Sec. 3.3.4 drops were initialized at the size of a condensing sea salt aerosol (20 μm), the radar scans used for this case study (Figure 3.14) begin after substantial drop growth had already occurred. Under the continuous collection model, drop growth rate increases with time – in the 1.5 g m^{-3} LWC, 3 m s^{-1} updraft scenario, the drop diameter increases to 1 mm in the first 25 minutes, and then to 4.2 mm in the next 10 minutes. This latter, rapid drop growth stage is what is observed in the case study in this section. Were the full lifecycle of the storm observed

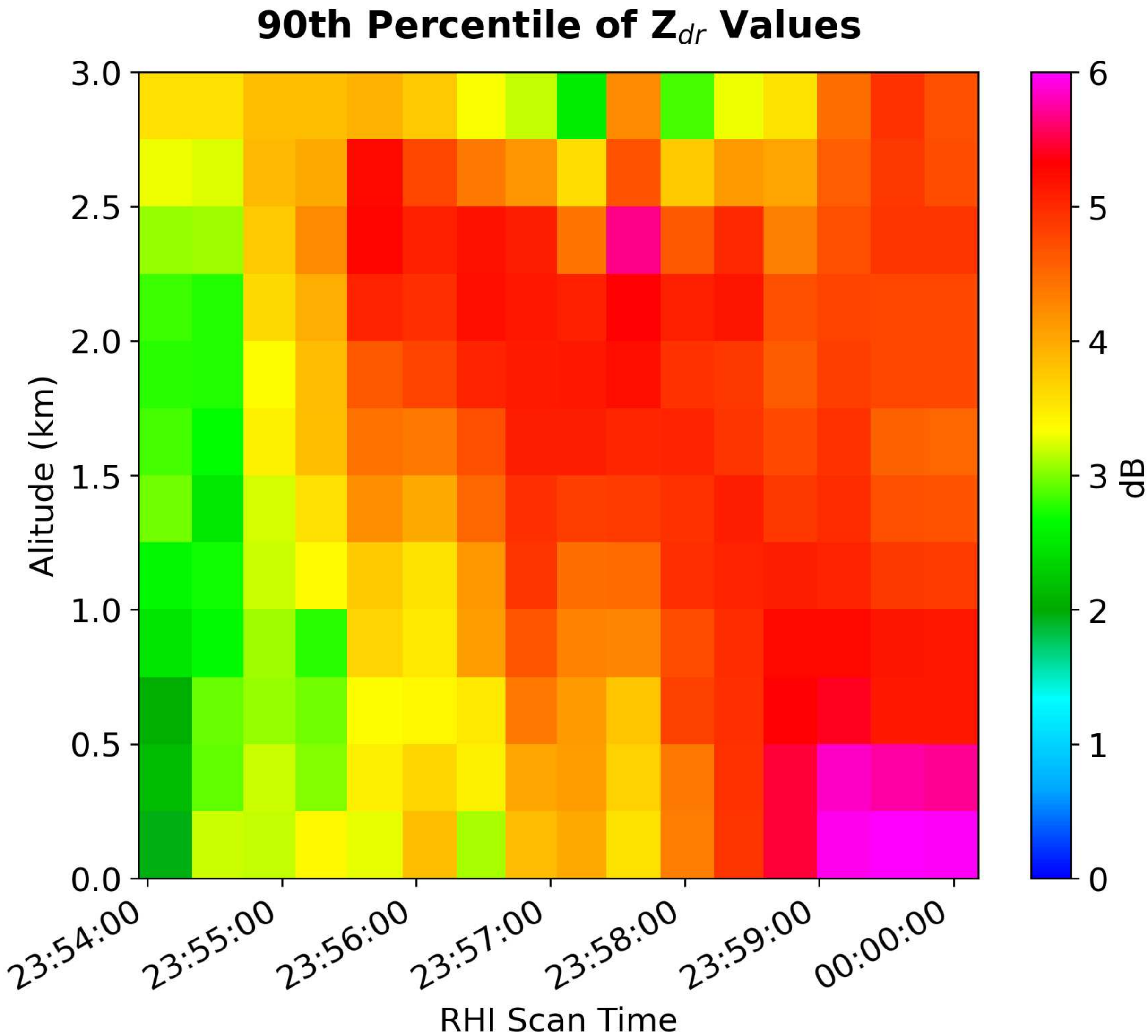

Figure 3.15: Vertical profiles of the 90th percentile of Z_{dr} values from the scans depicted in Figure 3.14. The color at each grid box corresponds to the 90th percentile of Z_{dr} values at a given altitude (y-axis) during a given scan (x-axis).

(including early growth prior to precipitation onset), it is expected that the time to detect large Z_{dr} values would be closer to what is predicted by the continuous collection model. Furthermore, the simple collection model is known to underestimate drop growth (Berry and Reinhardt 1974; Yau and Rogers 1996), so the times predicted by this model are likely over-estimates of how long it would take to form large drops.

3.5 Conclusions

In this study, we discussed isolated convection observed by the SEA-POL radar during the PISTON field campaign, marked by very large Z_{dr} values, denoting the presence of large (>4.5 mm) raindrops. While such drop sizes are commonly observed in the midlatitudes, owing to the melting of large, dense ice particles like hail, the majority of the convective cells examined in this study had echo tops which were near or below the freezing altitude, implying that these large drops were produced through warm rain processes (i.e., collision-coalescence). While large drops in tropical warm rain have been observed and studied previously (Beard et al. 1986; Rauber et al 1991; Takahashi et al. 1995; Szumowski et al. 1997; Szumowski et al. 1998; Szumowski et al. 1999; Hobbs and Rangno 2004; Gatlin et al. 2015), these studies focused primarily on individual case studies. The current study takes advantage of the extensive PISTON dataset and leverages the polarimetric capabilities of SEA-POL to study these large drop producing cells in a more statistical manner, looking at the average structure and characteristics of the HZCs themselves as well as the cells they occur in. Cells were also examined on a case-study level in this research, utilizing rapid vertical cross section scans performed by SEA-POL, as well as in-situ drop size distribution measurements made by aircraft which transected the storms.

The majority of HZC cells were small (mean area of 8 km^2), formed quickly (within 20 minutes of the first detection by SEA-POL of the parent cell), and were short-lived (usually < 10 minutes). Although the high-Z_{dr} regions themselves predominately existed below the 5 km freezing altitude (mean height of 3.7 km, 87% below 5 km), approximately half of HZCs existed within a cell which had echo tops above the freezing level. In deeper cumulus congestus clouds like these, particularly in the tropics where warm cloud depths are large and cloud water content is high, glaciation may be slow to occur (Johnson et al. 1999; Lau and Wu 2003). Therefore, we argue that although some ice/cold-rain processes may be ongoing in these taller cells, they are still predominately warm-rain based, and the high Z_{dr}/large raindrops are due primarily to collision-coalescence. Similarly, HZCs were occasionally found within large MCSs, which certainly have extensive regions of stratiform and cold-rain processes. However, it was found that HZCs within these MCSs were typically located on the outer edges of the leading convective lines, likely triggered by cold pool propagation. The young convection on the edges of these complexes were well-removed from the stratiform regions within the MCSs, and thus the large drops are again expected to have developed through primarily warm rain processes.

The average structure of isolated cells with HZCs were examined by looking at composite polarimetric radar variables in an upwind/downwind-height parameter space. A distinct size-sorting signal was evident, with the highest Z_{dr} values located on the upwind-edge of cells, along with low K_{dp}, suggesting this region is composed of a small concentration of large drops. Closer to the center, Z_{dr} began to decrease as reflectivity and K_{dp} increase, suggesting a mixture of large and small drops. Although the high Z_{dr} signal dissipates near cell-center, scattering simulations indicate that this may be due to a masking of the signal by a high concentration of smaller drops, rather than the large drops themselves vanishing. On the downwind half of HZC cells, Z_{dr}, reflectivity, and K_{dp} all decrease as correlation coefficient increases, suggesting this region is composed of numerous, uniform, spherical small drops (light rain or drizzle), also a result of wind-driven size-sorting. Vertically, Z_{dr} tended to be higher at lower levels of these cells. This is likely due to a combination of three factors continuing growth of drops through coalescence (Figure 3.8, Figure 3.9), and higher temperatures at lower altitudes, leading to increased Mie resonance effects caused by an increasing dielectric constant (Figure 3.7). These findings were supported by theoretical models, in-situ aircraft measurements of drop size distributions in an HZC, as well as a case study which utilized rapid vertical cross section scans of a shallow cell with an HZC.

Using a simple collection model, drop growth was simulated under various LWC and updraft scenarios. With this model, it was found that although all LWC's could theoretically support the formation of large drops provided a moderate 3 m s^{-1} updraft, only the 2 g m^{-3} scenario produced large drops at the timescales observed during PISTON (< 20 minutes). While sampling a HZC cell, the Learjet recorded LWCs in excess of 2 g m^{-3}, so this value is not unreasonable. Still, HZCs which took 60 or more minutes to form were occasionally observed, so extreme LWCs may be a sufficient but not necessary condition for large drop formation, given updrafts are sustained for long enough.

One outstanding question not addressed by this study is the impact of the environment on the abundance of HZCs. Figure 3.16 depicts a timeseries of the areal coverage of both isolated cells and isolated cells which contain an HZC. While isolated cells are always present at a relatively steady level, HZCs show much more variability. Some periods show little HZC activity (i.e., Sep. 11-14, 2019), while others show greatly enhanced HZC coverage (i.e., Sep. 18-20, 2019), despite similar overall isolated cell coverage. While it is tempting to try to use this timeseries to correlate environmental conditions (i.e., sea salt aerosol concentration, instability, moisture levels, vertical wind shear) to large drop presence, this cannot be done with the PISTON dataset alone. The primary limiting factor here is that, due to the masking effect discussed previously, one cannot equate a lack of an HZC signal to the absence of large drops. That is, cells which have large drops embedded within them may not have a high-Z_{dr} signature if these drops are mixed in with

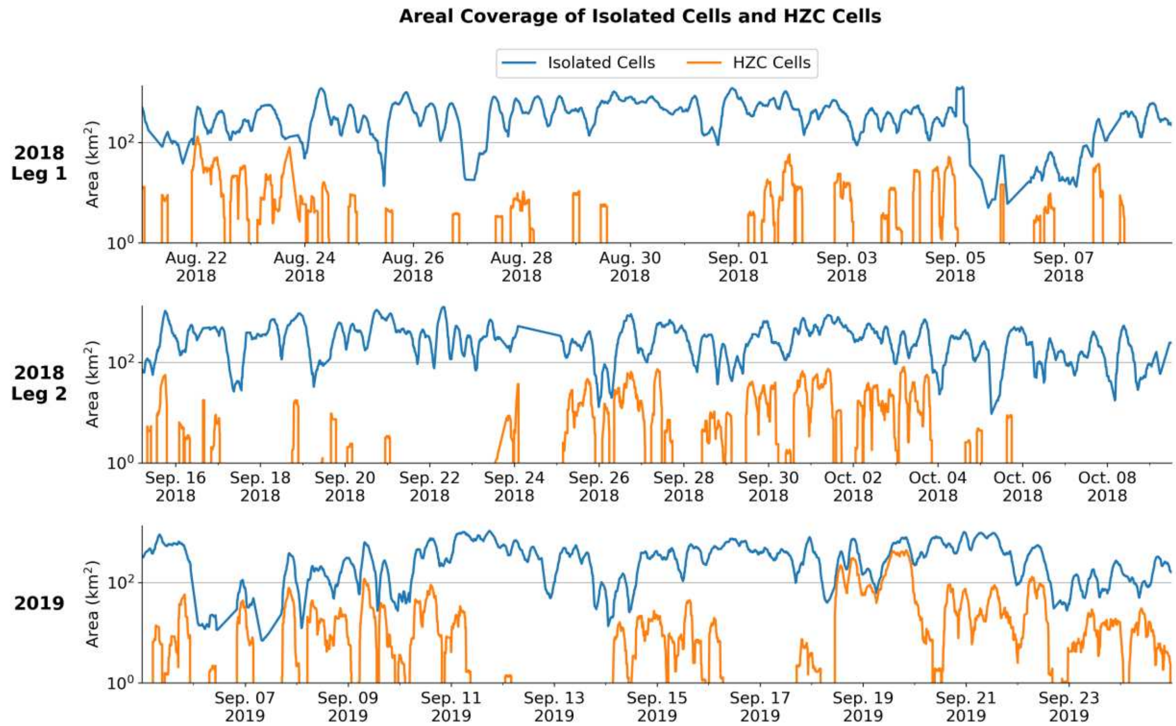

Figure 3.16: Timeseries of total areal coverage of isolated cells and isolated cells with HZCs. Timeseries are calculated as a 3-hour rolling average of the total areal coverage per SEA-POL scan of each cell type. Note that the y-axis scales are different for each of the three rows.

numerous smaller drops. Therefore, a timeseries of some metric which measures *HZC presence* may not be the same as a timeseries which depicts the presence of *large drops*. Therefore, a statistical correlation (or lack thereof) drawn between environmental variables and HZCs does not necessarily represent the relation between those environmental variables and large drops. Unfortunately, with the data collected during PISTON, we are unable to attain a timeseries of the actual drop size distribution within each cell observed.

While tracking HZC cells became a focus of the campaign as it was underway, PISTON was not specifically designed as a project for this topic, and thus there were factors limiting how optimally HZC data could be collected. Isolated cells are small and short lived, and were difficult to capture full lifecycles. Scanning strategies could be developed which are more optimal for capturing the evolution of individual cells at a high spatial and temporal resolution. And while polarimetric radar data can provide some information on the microphysical aspects of storms, the true drop size distribution (and presence/concentration of large drops) cannot be known without in-situ measurements from disdrometer and particle probes, particularly measurements from instruments on aircraft which can make multiple, targeted transects through storms. While aircraft data was used in JHWRP and HaRP to learn about large drops in warm rain, the radar observations in these projects were not dual-polarized. The additional microphysical insights provided by polarimetric radars such as SEA-POL provide exciting new context to place the aircraft observations in. While one HZC was observed simultaneously by SEA-POL and the CAMP^{2}Ex Learjet, these observations were again sub-optimal due to it not being the primary focus of either campaign. A future project which was designed specifically to address many of the topics and questions brought up in this study would be very beneficial in learning about these storms, and may lead to advances in how they are parameterized in models, which itself could have broad implications.

Chapter 4: Comparison of Precipitation Over the Western North Pacific from Space and Ship-based Radar

4.1 Introduction

Spaceborne satellite radars are important tools for measuring global precipitation. This is particularly true for the open ocean, where having permanent surface-based rain measurement networks (i.e., rain gauges or surface radars) is unfeasible. The first orbiting radar to take continuous 3D measurements of precipitation across the globe was the precipitation radar (PR) on board the Tropical Rainfall Measuring Mission (TRMM) satellite (Simpson et al. 1996; Kummerow et al 2000; Kozu et al. 2001). Launched in 1997, the Ku-Band TRMM PR was placed in a low-inclination, non-sun-synchronous orbit, allowing the radar to revisit locations (between 35 °S – 35 °N) at different times of day, which is important for observing diurnal patterns in precipitation (Negri et al. 2002; Chudler and Rutledge 2020). After nearly two decades of precipitation measurements with few interruptions, the TRMM PR went out of service in 2015. It was replaced with the Dual Precipitation Radar (DPR) on board the Global Precipitation Measurement (GPM) mission satellite, which had launched the year prior in 2014 (Hou et al. 2014). DPR improved upon the TRMM PR in several ways including expanded areal coverage (65 °S – 65 °N), improved revisit times, and somewhat better detection of light rain (Hamada and Takayabu 2016). Importantly, DPR consists of both a Ku-Band radar (KuPR) and a Ka-Band radar (KaPR) radar. Among other things, this dual-frequency measurement approach allows for improved measurement of rain rate and drop size distribution. A thorough description of GPM and its capabilities can be found in Hou et al. (2014).

While precipitation measurements from DPR are incredibly useful, satellite radar measurements are susceptible to several sources of error. Such errors include attenuation of the radar beam (Iguchi et al 2000; Meneghini et al 2015), detection/misclassification of non-meteorological ground clutter (Tagawa et al. 2007; Kubota et al. 2016), multiple scattering (Battaglia et al. 2010; 2014); and non-uniform beam filling (NUBF, Takahashi et al. 2006; Tokay et al. 2017). Related to the issue of NUBF is the limited horizontal resolution of DPR. With a horizontal "footprint" of approximately 25 km^2, DPR is unable to detect (or at least fully resolve) precipitating features smaller than this native footprint. Chudler and Rutledge (2021) found that 10% of rainfall in the open ocean is contributed by small, isolated cells. While some of these features would indeed be detected by DPR (isolated features could have a length of up to 20 km in their study), features which were smaller than 5 km in length would be poorly resolved by DPR at best. Furthermore, precipitating features generally have internal spatial variability on scales much smaller than the storm itself. That is to say, while DPR can certainly detect a 100 km^2 feature, smaller intense regions in the feature would not be resolved. This leads to the issue of NUBF, wherein variability of precipitation on scales smaller than the DPR resolution leads to uncertainties in the retrieval of rain rate and drop size distribution parameters.

In order to assess the accuracy of DPR precipitation measurements and the impact of the error sources addressed above, many ground-based validation studies have been performed wherein DPR rainfall retrievals are compared with rain gauge networks and/or ground-based radars. When compared to rain gauge networks, DPR typically tends to underestimate rainfall

(Speirs et al. 2017; Hayden and Liu 2018; Watters et al. 2018; Gao et al. 2021). While surface-validation of rain measurements is difficult over the ocean, Petersen et al. 2020 utilized observations from the S-Band radar on the Kwajalein Atoll to approximate open-ocean conditions. They found that DPR generally met the Level 1 Mission Science accuracy requirements put forth in the GPM mission statement (see Skofronick-Jackson et al. 2017 for details). However, these errors were only calculated over ranges of precipitation rate and at resolutions which are detectable by DPR – precipitation at scales which DPR was not designed to capture were not considered, although they likely contribute significantly. Examining DPR estimates of mass-weighted mean drop diameters, D'Adderio et al. (2018) found that DPR generally performed well over their study region, with the exception being when there was high spatial variability of precipitation within the DPR footprint, which led to significant errors.

During the late-summer and early autumns of 2018 and 2019, the Propagation of Intraseasonal Oscillations (PISTON) Field Campaign (Sobel et al. 2020) took place in the open waters of the western North Pacific. This ship-based field campaign provided measurements of atmospheric and oceanic process in a part of the world with few previous in-situ observations. Of particular interest for the present study is the data obtained by the SEA-POL weather radar, a polarimetric C-Band radar which obtained 3D measurements of precipitation at high resolution for the duration of the combined 70-day field campaign (50 sea days in 2018 and 20 sea days in 2019). This provides a unique opportunity to examine the accuracy of DPR over the open ocean. By utilizing SEA-POL's extensive precipitation measurements, this study seeks to evaluate DPR's performance and investigate possible sources of error, particularly those cause by the satellite's limited resolution.

4.2 Data and Methods

We only use data from the GPM KuPR radar in this study (GPM 2Aku V06, Iguchi and Meneghini 2016). The 13.6 GHz Ku-band radar was chosen over the 35.5 GHz Ka-band due to its larger swath size and better suitability for measuring moderate and heavy precipitation. KuPR has a horizontal resolution of approximately 5km, and a vertical resolution of 125 m. Geolocation of the gridded KuPR data was corrected for parallax error arising from the slanted beam angle relative to the surface. Rain rate for KuPR was taken from the internal DPR algorithm, which has been specifically tuned for the instrument. Note that while this study will utilize reflectivity data from only KuPR, the rain rate is calculated using information from both KuPR and KaPR.

Also used in this study is data from the Colorado State University SEA-POL weather radar (Rutledge et al. 2019 a, b). This C-Band, polarimetric radar operated nearly continuously for the duration of both cruises, taking 360-degree scans of precipitation out to 120 km every 10-15 minutes. To avoid radiating the ship's bridge, the radar transmitter was automatically disabled over a 115° (80°) sector to SEA-POL's aft in 2018 (2019). For this study, the SEA-POL data has been interpolated onto a regular cartesian grid, with a horizontal resolution of 1km and a vertical resolution of 0.5 km. Rain rate for the SEA-POL dataset was calculated using the method outlined in Thompson et al. (2018), which is optimized for tropical precipitation. The radar data was rigorously quality controlled to remove non-meteorological echoes and other erroneous measurements. More information on this quality control process, as well as the method used for gridding and the specific scanning strategy used during PISTON, can be found in Chudler and Rutledge (2021).

During PISTON, there were only 26 instances where the KuPR radar swath was aligned with the SEA-POL coverage area, only 18 of which contained any precipitation. While these overpasses are useful in seeing how the two radars generally compare to one-another, the limited sample size precludes any more rigorous statistical analysis. To overcome this, Section 4.3.2 of this study will compare bulk statistics from KuPR and SEA-POL, regardless of if the scans overlapped or not. All scans which intersected the broader PISTON operations region (defined in this study as a box bounded by 0-30 °N and 125-155 °E) during PISTON operations periods (Aug. 20 – Oct 9, 2018, Sep 5 – 25 2019) were collected for this analysis. Initially, it was noted that due to the much larger areal coverage of a full KuPR swath, KuPR saw very large precipitating systems (> 10^4 km^2) much more frequently than SEA-POL. And as a result, the total rainfall contribution of large systems in the KuPR dataset was much greater than that of SEA-POL. However, this was again due to differences in sampling rate, rather than how the radars are intrinsically representing these systems. To better equate the sampling rate of different-sized precipitation features between SEA-POL and KuPR, a new method was developed to resample the KuPR dataset. Each KuPR radar swath was split into contiguous 120 km radius circles (Figure 4.1), equaling the coverage area of a SEA-POL scan. To better match the SEA-POL data, each of these resampled circles was also given an artificial blanked sector (see discussion in previous paragraph) over which KuPR data was purposely masked. The direction of these blank sectors was chosen randomly. By resampling the KuPR data in this way, the sampling rate of different-sized precipitation features was seen to match more closely what was observed by SEA-POL. The resampled KuPR data is used in Section 4.3.2.

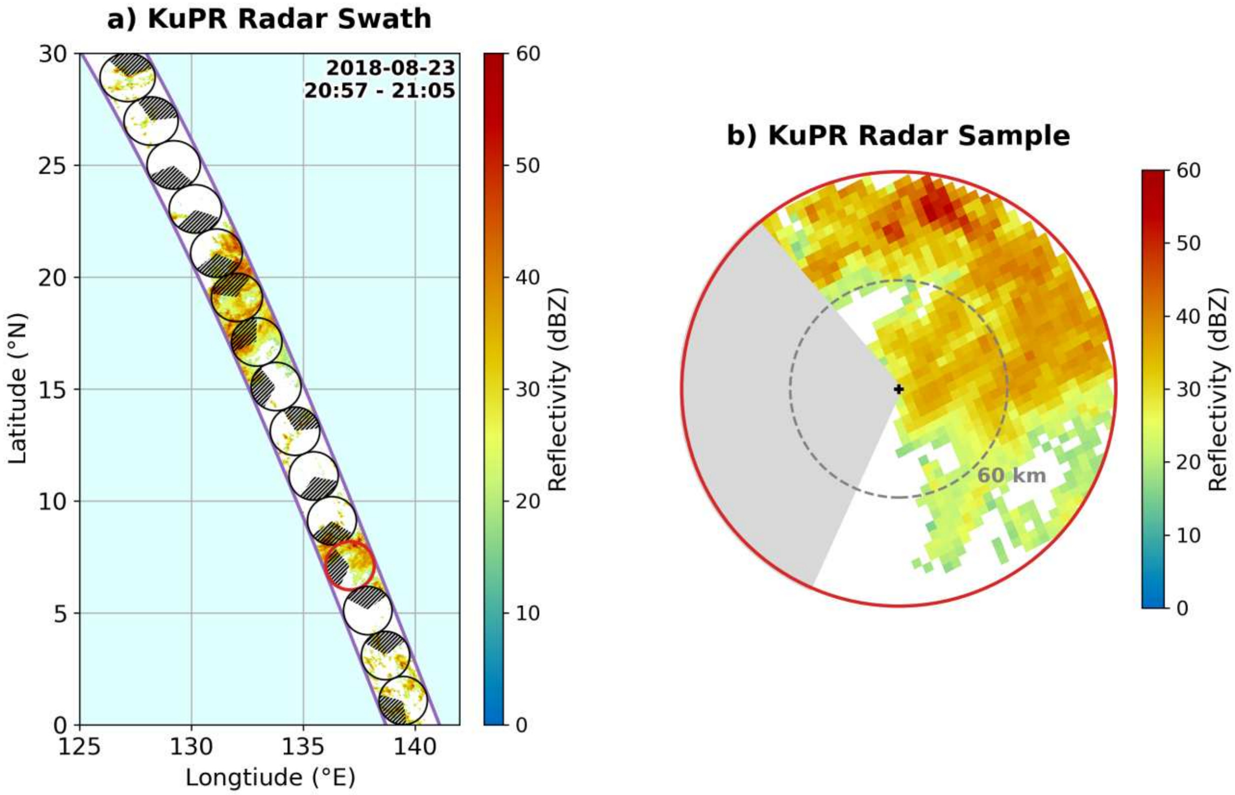

Figure 4.1: Example demonstrating the method used to resample the KuPR radar swaths into circles with radii of 120 km, matching the coverage area of a scan from SEA-POL. Each resampled circle was also given a simulated "blanking sector", denoted with hatched black lines in (a) and the grey wedge in (b). The zoomed-in example shown in (b) corresponds to the red circle in (a).

As in Chudler and Rutledge (2021), "precipitation features" were identified using an algorithm which searches for contiguous pixels with a reflectivity above some threshold. Features were identified at the 2 km grid level for SEA-POL. The KuPR data is provided on an irregular grid with no constant vertical levels, so the range gate which was closest to the 2 km level was used. Due to the high vertical resolution of KuPR (125 m), the difference between the altitude of the range gate used and the actual 2 km level was typically quite small (< 100 m), so this slight discrepancy is not expected to significantly impact results. Features were grouped using a 17 dBZ threshold, as this is the approximate minimum detectable signal from KuPR. All reflectivity lower than this threshold was discarded in both radar datasets.

4.3 Results

4.3.1 DIRECT COMPARISONS

Although direct overpasses of KuPR over SEA-POL were infrequent, there were a total of 26 instances during the two PISTON campaigns where both radars made concurrent (within 5 minutes) measurements over the same area. Of these 26 overpasses, 18 had at least some precipitation within the overlapping area. An example of such a concurrent scan is provided in Figure 4.2. Note that in this section, where direct overpasses are being compared, the KuPR swaths have not been resampled with the method discussed in Section 4.2. Several details stand out immediately in Figure 4.2. First, most of the convection within SEA-POL's range is small, but with intense cores with reflectivities exceeding 40 dBZ. The cells are ~10 km wide in places, with even smaller convective cores. Looking at the KuPR data, the impact of KuPR's limited (5 km) resolution is readily apparent. The peak intensity of the cells in the KuPR view are below that of

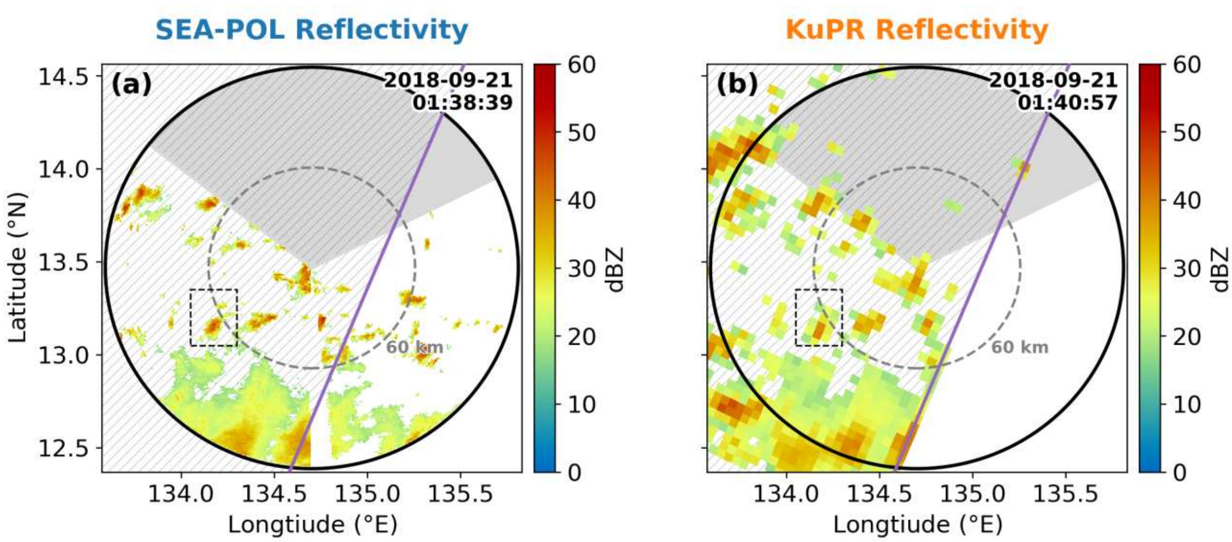

Figure 4.2: An example of precipitation which was observed by both SEA-POL (a) and KuPR (b). The times in the upper-right corner of each plot show the time each scan was taken. The purple line marks the edge of the KuPR radar swath, and the light hatching notes the area contained within the swath. The black dashed box denotes the area which is plotted in Figure 4.3.

SEA-POL with no cells achieving a reflectivity greater than 40 dBZ. The intense convective cores which are smaller than the KuPR footprint cannot be fully resolved. Additionally, the small cells all appear to be slightly larger in the KuPR scan than they are in the SEA-POL scan. This is likely a result of the true cell edge being within a single KuPR pixel. Within a 25 km^2 KuPR gird box, if one half of the box has precipitation and the other does not, KuPR appears to mark that entire grid box as having precipitation. The combined result of these two effects is that KuPR appears to underestimate the intensity of small, isolated cells, but overestimates their areal coverage, at least based on this single comparison. On the other hand, KuPR appears at first glance to do a better job representing the larger feature on the south side of the radar scan.

The isolated feature in the black box in Figure 4.2 is examined in a three-dimensional orthographic projection in Figure 4.3, allowing variability on sub-KuPR-footprint levels to be seen in more detail. The highest reflectivity exists within a single 1-2 km wide column on the north side of the cell, which is not captured by KuPR. The tendency for KuPR to broaden out these small

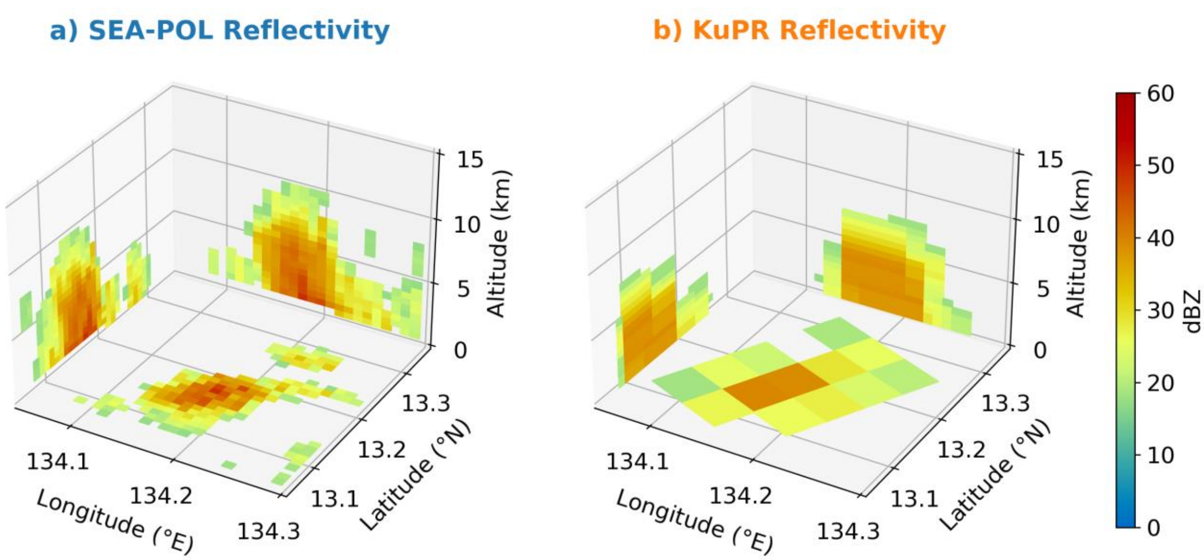

Figure 4.3: Orthographic projections of a small precipitating cell seen by SEA-POL (a) and KuPR (b). This cell is marked with a box in Figure 4.2.

cells is again apparent. KuPR also appears to underestimate the echo top height for this cell. SEA-POL shows reflectivity up to 10 km, while KuPR reflectivity tops out around 7.5 km. This could be a sensitivity issue, as KuPR may struggle to detect weak echoes composed primarily of ice at these levels.

Figure 4.4 shows a scatter plot with the mean rain rate, maximum rain rate, precipitating area and rain volume (defined as the mean rain rate multiplied by the raining area) from each of the 18 matched KuPR/SEA-POL radar scans with precipitation. For each scan, statistics were only calculated for the overlapping portion of each scan. For example, for the match scan plotted in Figure 4.2, only the precipitation which is to the west of the KuPR swath edge (purple line), within the SEA-POL's range (black circle), and outside of the blanked sector (grey wedge) is used. On average, KuPR rain rate is 50% lower than SEA-POL, for both the mean and the maximum rain rate. The difference becomes more dramatic for intense rain, where a maximum rain rate of 48 mm hr^{-1} from SEA-POL is only registered as 10 mm hr^{-1} by KuPR. While rain rate appears to be underestimated by KuPR, precipitating area is overestimated. Across all matched scans, KuPR saw 113% more raining area than KuPR, although most of this excess area was in regions of light rain. The net effect of these two differences (of opposite sign) is seen in the rain volume plot, where the differences between the two radars are smaller. Summing all scans together, the KuPR swaths contained 23% more rain volume than the SEA-POL scans for this data sample.

In addition to looking at the rainfall statistics for entire scans, it is also useful to look at how SEA-POL and KuPR differ in observing specific echo features. Two methods can be used for this direct feature comparison, as demonstrated in Figure 4.5. Essentially, the concept is to outline a geographic area that contains some feature in one radar, and then look at the

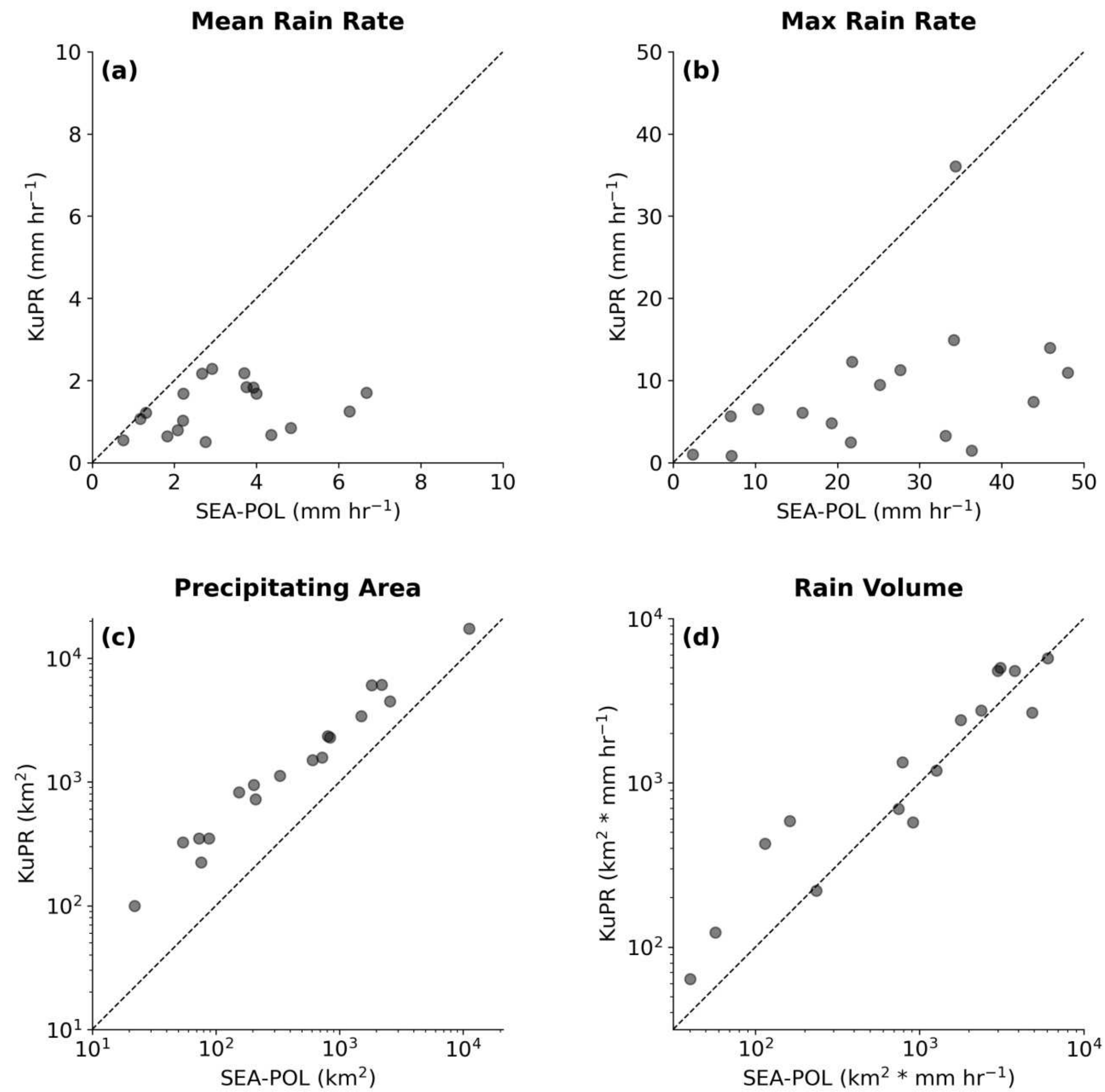

Figure 4.4: Mean rain rate (a), maximum rain rate (b), total precipitating area (c), and total rain volume (d) for each matched SEA-POL and KuPR scan. Each point represents the data from one matched scan. The dashed diagonal line marks the one-to-one line.

precipitation (or lack thereof) contained within this outlined region as seen by the other radar. However, because the two radars may see a single feature differently, this can be done one of two ways – define a feature area based on SEA-POL reflectivity (blue line in Figure 4.5), and then examine that area in KuPR reflectivity, or vice versa (orange line in Figure 4.5). Doing this for

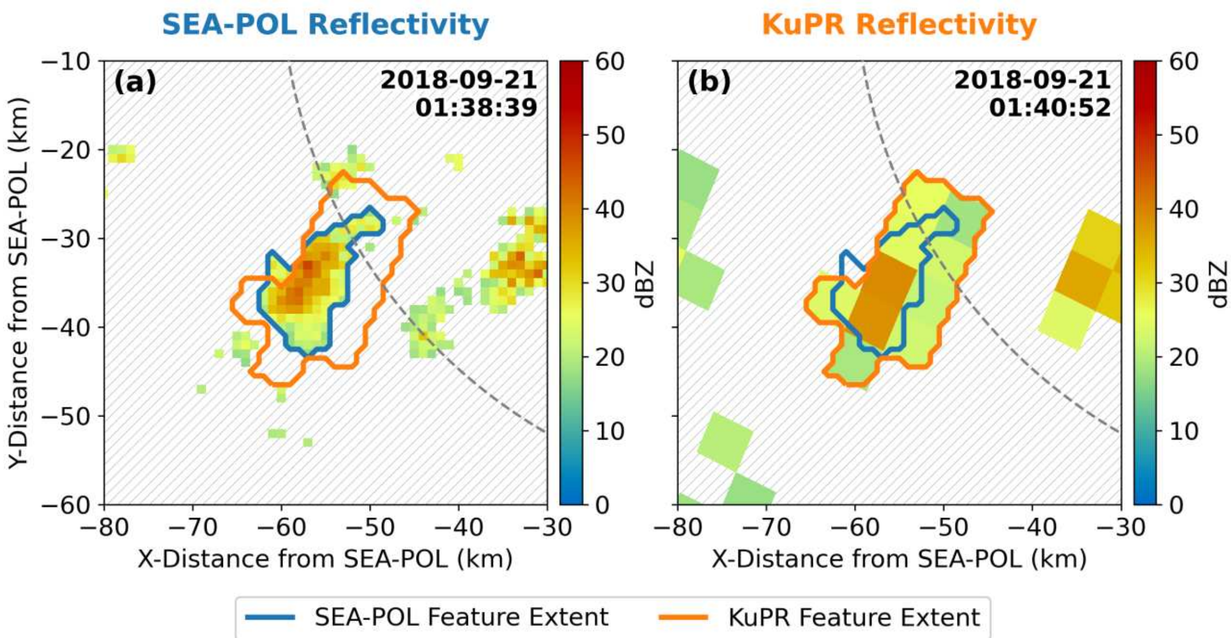

Figure 4.5: Demonstration of the two radar comparison methods used in this study. Both images show the same cell as observed by SEA-POL (a) and KuPR (b). The feature extent, as seen by both radars, is outlined in each image.

every feature results in two complimentary datasets which together provide interesting detail on how SEA-POL and KuPR detect precipitation features differently.

Figure 4.6 shows the same rain statistics as Figure 4.4, but with individual points for every feature (as defined above). The rain rate plots show a familiar picture – no matter the sampling method, KuPR tends to underestimate rain rates, particularly at extreme values. However, an interesting separation between the two methods appears when looking at feature area (Figure 4.4c). First, note that all blue dots fall along or below the one-to-one line, and all orange dots fall above it. This is by design – a blue dot falling above the one-to-one line would mean that KuPR has more precipitating area within a SEA-POL feature region than SEA-POL, which is impossible because, by definition, that region is already 100% filled with SEA-POL precipitation. A similar

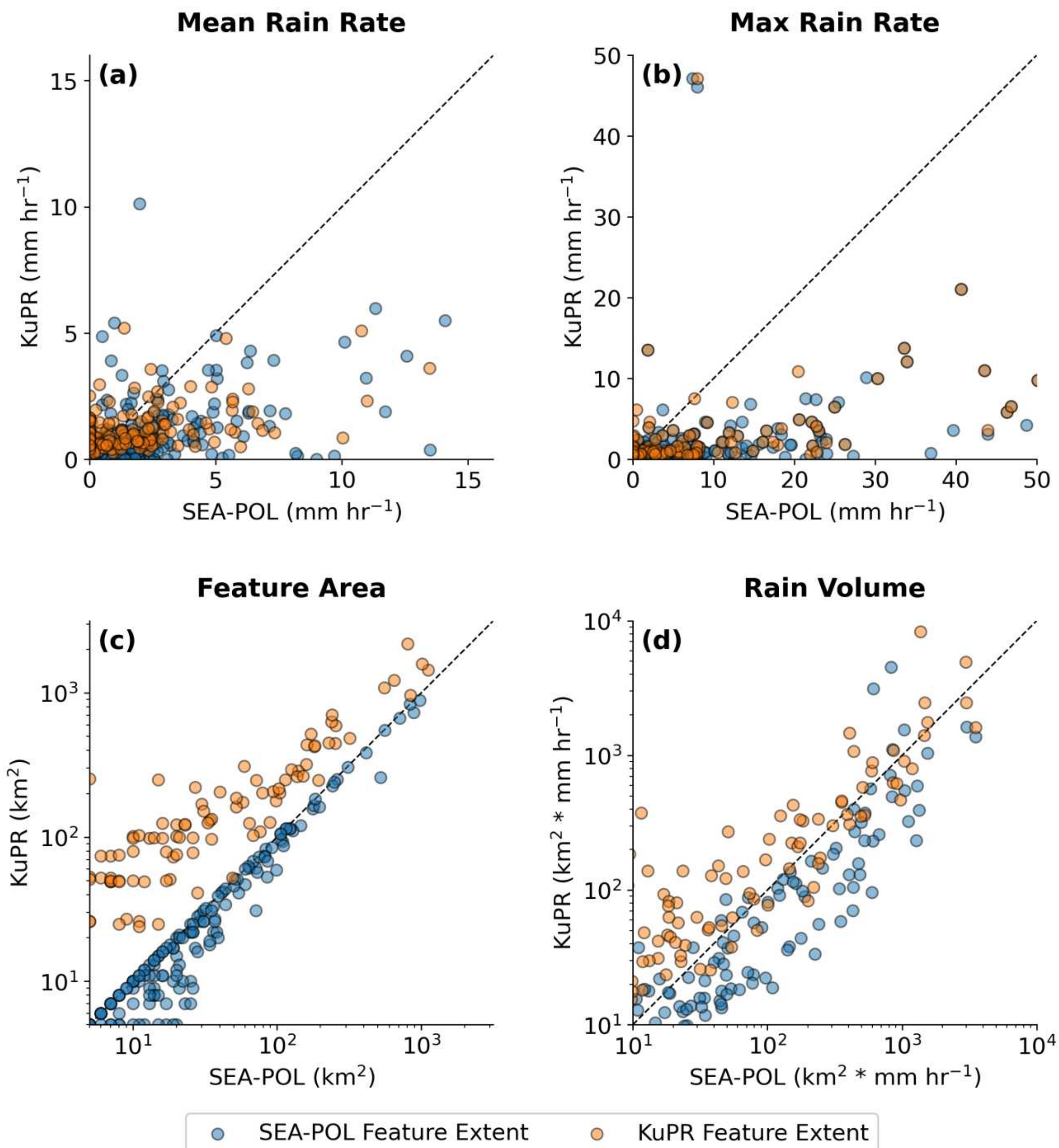

Figure 4.6: As in Figure 4.4, but with a scatter point for each individual feature. Blue dots represent features seen by SEA-POL (and the corresponding area in KuPR), and orange dots represent features seen by KuPR (and the corresponding area in SEA-POL).

argument can be made for why the KuPR features (orange dots) do not fall below the one-to-one line.

What this plot does tell us is how often (and to what degree) a feature area defined by one radar is not "filled in" by the other radar. A blue dot below the one-to-one line means that KuPR does not see all of the precipitating area that SEA-POL sees, and an orange dot above the one-to-one line means SEA-POL does not see all of the precipitating area that KuPR sees. Generally, the blue dots all fall on or close to the one-to-one line. This makes sense – if a SEA-POL feature is large enough, KuPR should be able to fully detect that area. The exception to this is small features (< 35 km^2) where KuPR appears to occasionally have little or no precipitating area because of its limited resolution. On the other hand, for KuPR features (orange dots), SEA-POL almost never completely fills these regions with precipitation. This agrees with the idea of KuPR increasing the areal extent of features, as discussed previously.

The rain volume scatter plot (Figure 4.6d) combines the effects of reduced rain rates and increased area in KuPR features. KuPR underestimates total rain volume within regions defined by SEA-POL features (blue dots). These regions may contain narrow convective cores which cannot be fully resolved by KuPR. Conversely, within regions defined by KuPR features (orange dots), SEA-POL has less rain volume, likely because KuPR is overestimating the size of those regions (meaning that much of the KuPR feature region is echo free for SEA-POL and therefore contributes no rain). Again, this demonstrates that although total KuPR rain volume is generally fairly accurate, it may be in part due to offsetting errors of opposite sign.

Two individual precipitation features which were observed by both radars will now be examined in detail. Figure 4.7 depicts a cluster of small convective cells which were captured by both radars on August 28, 2018. First, the tendency for KuPR to overestimate feature size is again evident. In this case, what SEA-POL shows to be two separate features is actually merged into

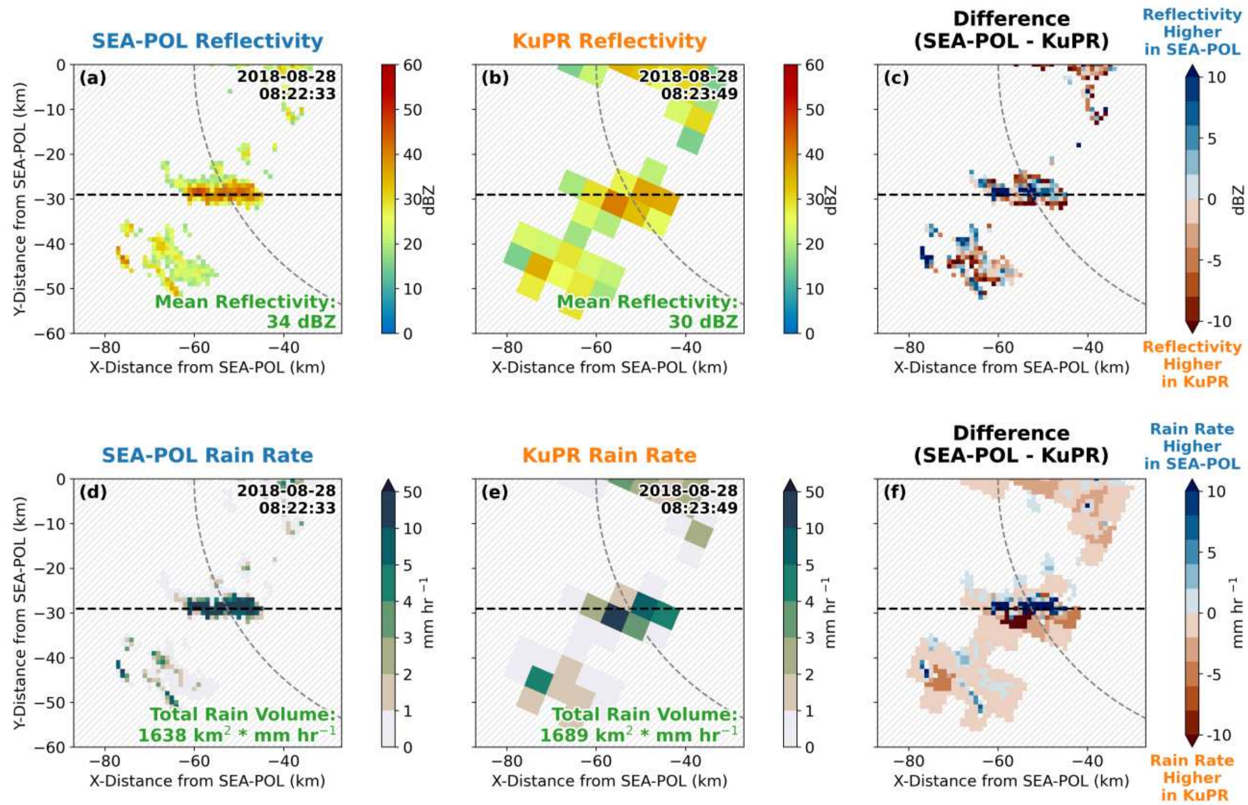

Figure 4.7: Reflectivity (a, b, c) and rain rate (d, e, f) for a small convective cell which was observed simultaneously by both SEA-POL (a, d) and KuPR (b, e). The difference between SEA-POL and KuPR is given in (c) and (f). The horizontal black dashed line at y = -29 km marks where the cross-section of Figure 4.8 is taken.

one larger feature for KuPR. The northern cell is very narrow, with a north-south width of < 10 km, and an even narrower region of intense (40+ dBZ) reflectivity. KuPR is unable to resolve this feature, and as a result, underestimates rain rate by over 10 mm hr^{-1} at locations within the core. Interestingly, the rain rate estimates are generally more accurate for the southern cell, which does not have the same narrow, intense core. Over the entire plotted domain, the KuPR rain volume (printed on the bottom-right corner of the figure) is close to the SEA-POL rain volume (KuPR higher by 3%). However, if calculating for just the northern cell, KuPR has 30% less rain volume than SEA-POL. A vertical cross section of the northern cell is examined in Figure 4.8. KuPR underestimates reflectivity and rain rate over most of the extent of the cell. KuPR does a better

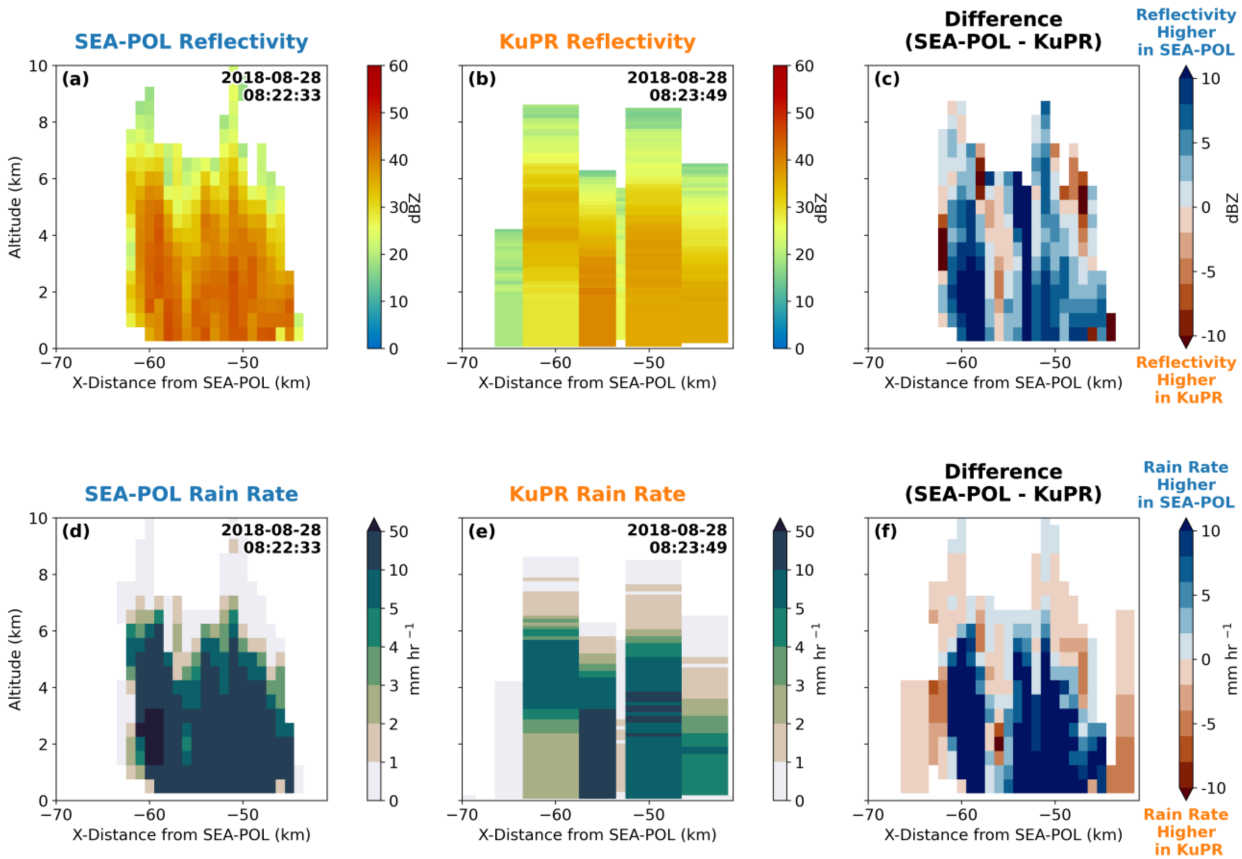

Figure 4.8: As in Figure 4.7, but looking at a vertical cross section of the system. The cross section is taken at y = -29 km, as marked in Figure 4.7. Note that the scales of the x- and y-axes are not the same, and the vertical extent is exaggerated compared to the true aspect ratio.

job at capturing the full vertical extent of this cell than the one examined in Figure 4.3, only underestimating echo top height by about 1 km in this case.

On September 30, 2018, a large precipitating system (associated with an outer rainband of Typhoon Kong-Rey), was observed by both SEA-POL and KuPR (Figure 4.9). Overall, KuPR detected this system well, although it appears to broaden the light rain on the edges of the system beyond the extent of what SEA-POL sees. KuPR reflectivity is higher across most of the rain band. Previous studies have shown that satellite radar algorithms tend to have anomalously high reflectivity below the melting layer in stratiform rain (Wang and Wolff 2009; Louf et al.

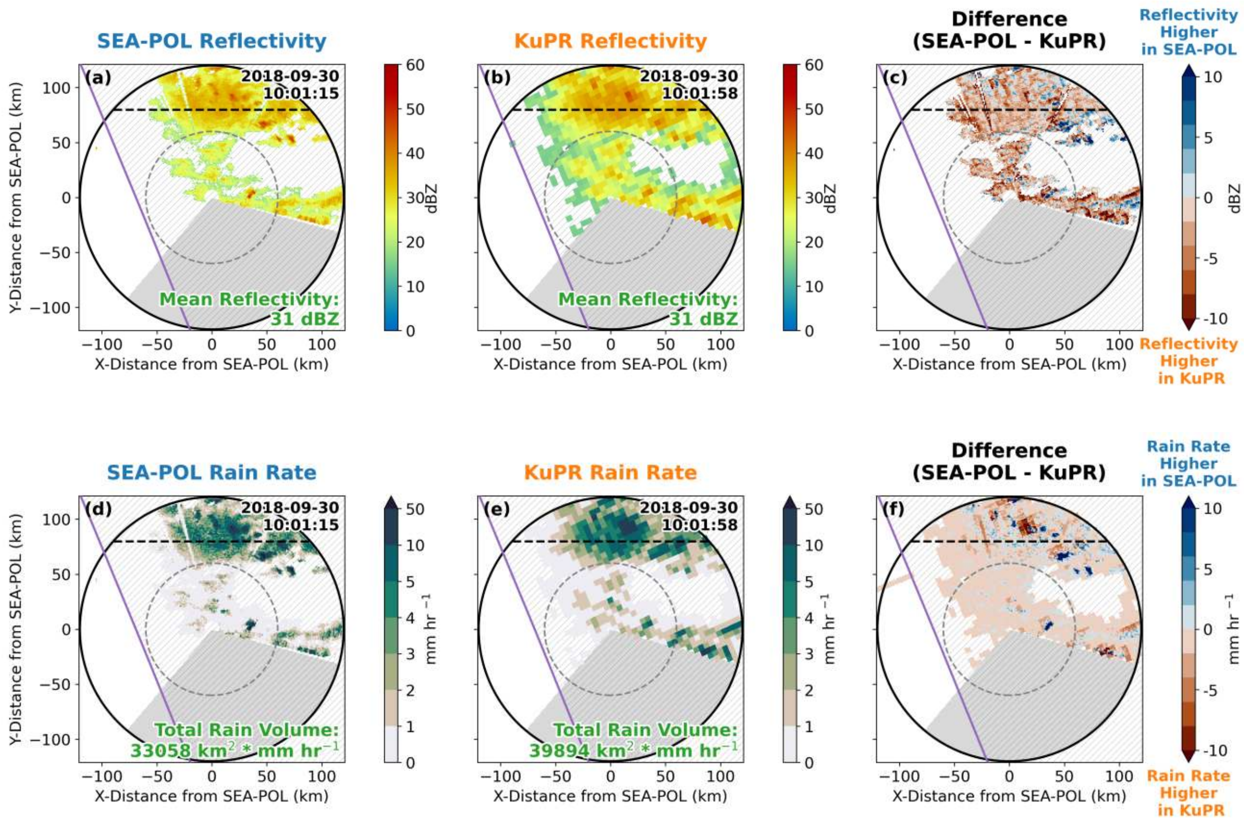

Figure 4.9: As in Figure 4.7, but looking at a large precipitating system. The horizontal black dashed line at y = 80 km marks where the cross-section of Figure 10 is taken.

2019), due to overcorrection of attenuation below the radar bright band (i.e., areas of relatively high reflectivity at the melting level that arise to due melting ice aggregates). As will be shown in the next figure, the extensive region of predominantly stratiform rain examined here has a strong bright band signature, which is apparently leading to the high KuPR reflectivity. However, the rain rate algorithm used by DPR, which has been tuned and calibrated to adjust for attenuation issues (among other things), appears to do appropriately account for this anomalously high reflectivity. While rain rate is slightly higher in KuPR than in SEA-POL throughout the rain band, the difference is not nearly as stark as the reflectivity difference. There are also a few small areas where KuPR underestimates rain rate (blue colors in the difference plots). These areas correspond with small, embedded convective cores within the rain band which KuPR cannot fully resolve. Overall, KuPR rain volume is 21% higher than SEAPOL. Of this excess rain volume, 61% was found to be due to KuPR detecting more precipitating area, and 39% was due to KuPR rain rates being slightly higher in comparison to SEA-POL.

A vertical cross section of the rain band is plotted in Figure 4.10. A striking melting layer signature is noted around 5 km in height, both in reflectivity and in the reflectivity difference plot. This signature is notably clearer in the KuPR scan than in SEA-POL, due to KuPR's higher vertical resolution (~125 m) than SEA-POL (500 m). Above this level, reflectivity is greater in SEA-POL, possibly due to KuPR's limited ability to detect weaker ice echoes. Below this level,

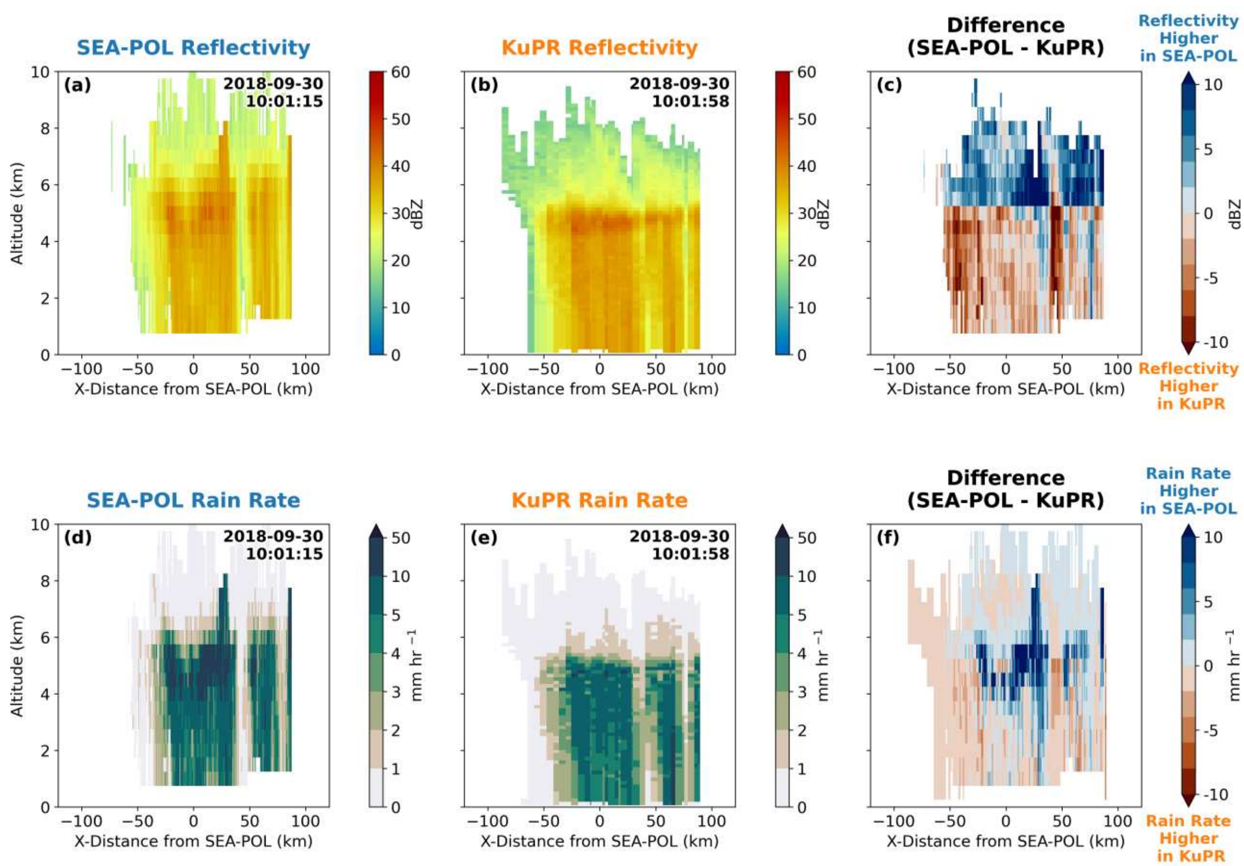

Figure 4.10: As in Figure 4.8, but looking at a cross section of the large mesoscale convective system from Figure 4.9.

however, KuPR reflectivity is almost uniformly higher than SEA-POL. The effect of KuPR reflectivity being over-corrected for attenuation, resulting in artificially high values, is clearly evident here. Despite this, the internal rain rate algorithm again appears mostly correct for this, as rain rates are only slightly higher in KuPR below the melting layer.

4.3.2 STATISTICAL COMPARISON

This section will use the KuPR resampling method discussed in Section 4.2 to compare the attributes of precipitation features observed by SEA-POL and KuPR, composited by feature size. The occurrence frequency of different feature sizes, defined as the percent of scans/resampled swaths which contain least one feature within a given size bin, is plotted in Figure 4.11a, and rain volume contribution (defined as the fraction of the summed rain volume from all scans which

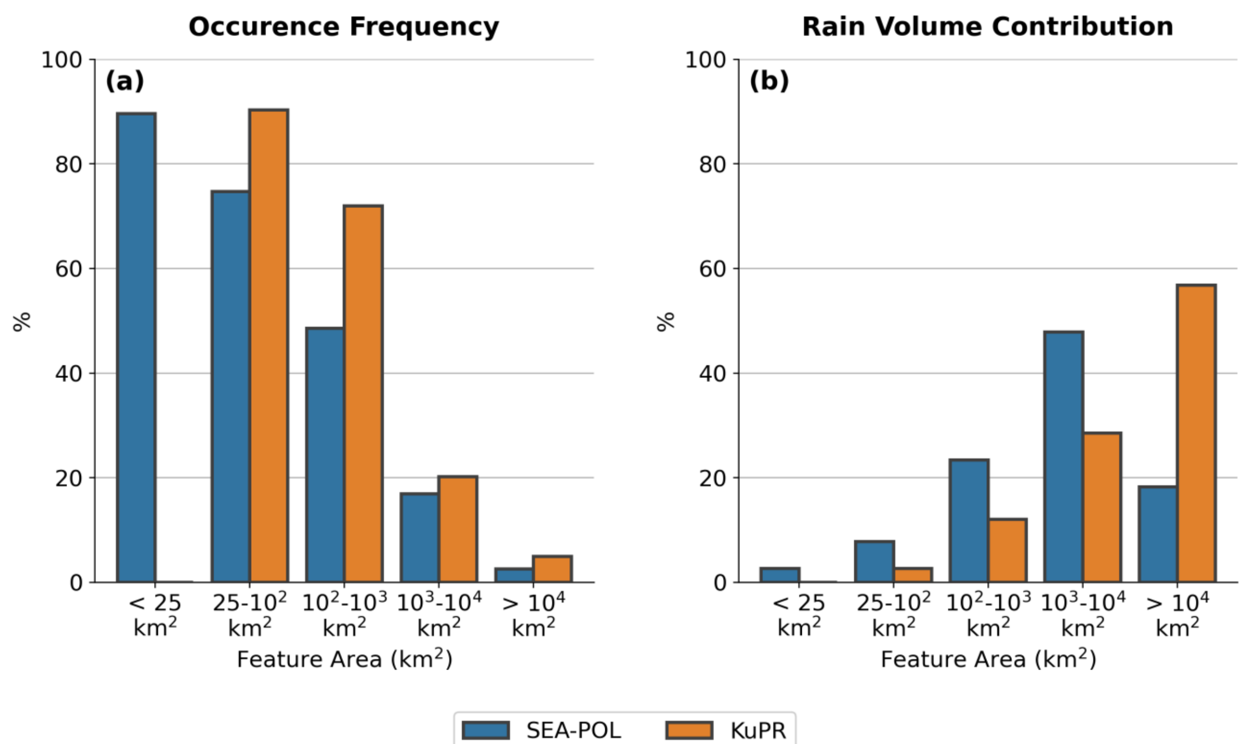

Figure 4.11: Occurrence frequency (a) and rain volume contribution (b) for precipitation features of different sizes, as seen by SEA-POL (blue) and KuPR (orange).

was contributed by features in a given size bin) is plotted in Figure 4.11b. Generally, as feature size increases, occurrence frequency decreases and rain volume contribution increases (consistent with the results of Chudler and Rutledge 2021).

For KuPR, the smallest size bin (< 25 km^2) is empty because this is smaller than the KuPR footprint, and features of this size therefore are not found in the KuPR data. For features larger than 25 km^2, occurrence frequency matches up reasonably well between SEA-POL and the resampled KuPR data, showing the effectiveness of the resampling method. Prior to resampling, the original full KuPR swaths had occurrence frequencies of 98%, 95%, 80% and 40% for the 25-10^2, 10^2-10^3, 10^3-10^4, and > 10^4 km^2 size bins, respectively (not shown), which are drastically different than the SEA-POL numbers.

Even with the resampling, however, KuPR still has higher occurrence frequencies for all size bins. This may be due to the tendency for KuPR to broaden features, as discussed earlier. For example, a feature which has an area of 99 km^2 may be seen by KuPR as having an area of 100+ km^2, placing it in the next size bin up, and thus increasing the occurrence frequency of that size bin. Similarly, the 25-10^2 km size bin for KuPR is likely in part composed of features which are in fact smaller than 25 km^2. KuPR can tell that there is *some* precipitation there, and marks the entire 25 km^2 pixel as having precipitation, even though the actual feature is smaller than that.

For rain volume contribution (Figure 4.11b), SEA-POL appears to have a larger fraction of rain contributed by small and medium-sized features (< 10^4 km^2), while KuPR has a larger portion of rain from the largest features. This may be due to several reasons. First, SEA-POL is better able to resolve small convective cores with intense rain within small features, so a greater amount of rain will come from them. Second, as was seen in Figure 4.11a, KuPR identifies larger features more often, so this will naturally lead to more rain volume from these features. Finally, as was seen in Figure 4.9, there may be a tendency for KuPR to overestimate rain rates in stratiform rain, although this cannot be determined from looking at rain volume alone

Figure 4.12 shows the distributions of mean rain rate and total rain volume for different features sizes seen by SEA-POL and KuPR. For features with areas less than 10^3 km, KuPR has significantly lower mean rain rates than SEA-POL, likely due to its diminished ability to detect heavy rain in small convective cores. For very large features (> 10^4 km^2), however, KuPR has higher rain rates and rain volumes than SEA-POL. As discussed previously, increased rain volume is hypothesized to be due in part to increased feature area in KuPR. However, the increased rain

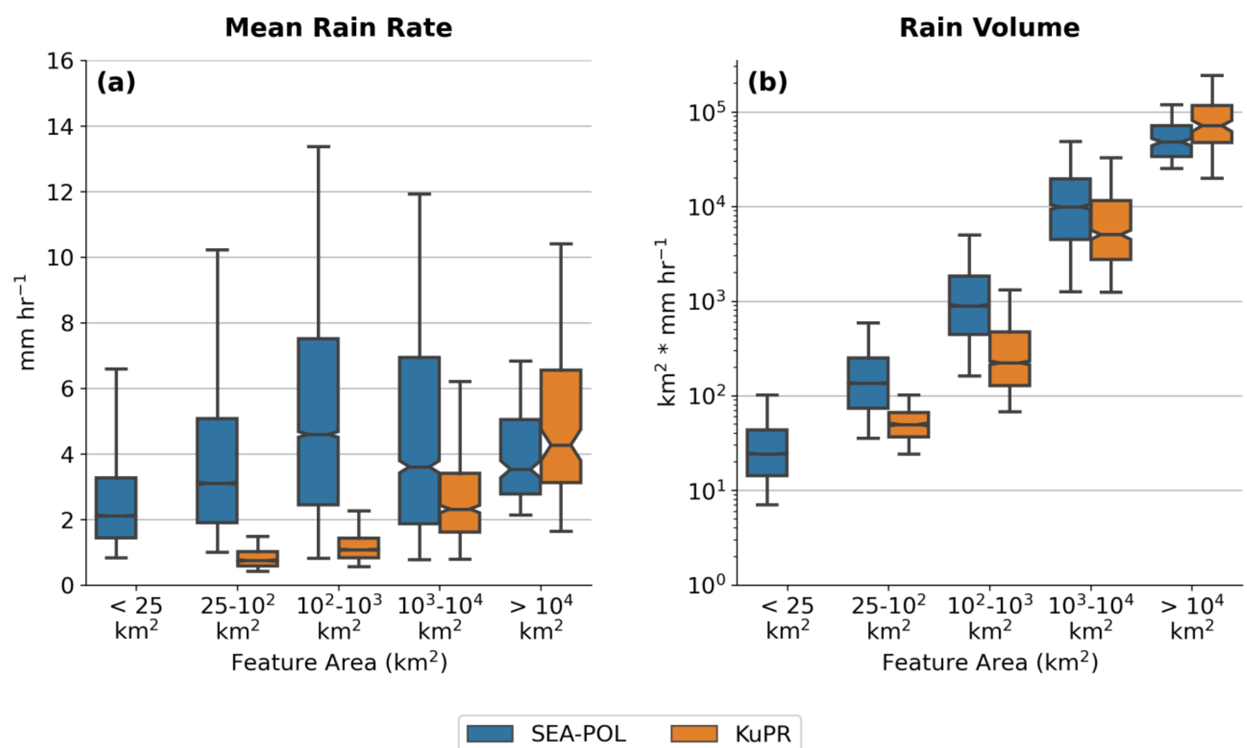

Figure 4.12: Distributions of mean rain rate (a) and total rain volume (b) for different feature sizes from SEA-POL (blue) and KuPR (orange). Boxplot whiskers represent the 5th and 95th percentiles of the data. Notches around the boxplot median values represent the confidence interval around the median, as calculated using a Gaussian-based asymptotic approximation.

rate seen in Figure 4.12a must be due to a separate effect. Large features like these almost certainly have extensive regions of stratiform rain, which has been shown to be associated with erroneously high reflectivity due to overcorrection of attenuation below bright bands (Wang and Wolff 2009; Louf et al. 2019). While the DPR rain rate algorithm mostly corrects for this (as seen in Figure 4.10), these results suggest that KuPR is still systematically seeing higher rain rates in large systems (at least in the PISTON domain).

c) *Simulated KuPR Rain Volume*

Thus far, we have shown that SEA-POL and KuPR differ in several ways in their observations of precipitating systems. The sign and magnitude of these differences depend on the intensity and size of the raining feature KuPR mapped, which in turn may depend on environmental parameters such as instability, wind shear, moisture content, etc. From this, it stands to reason that the difference between SEA-POL and KuPR may vary with such environmental conditions. The PISTON cruises saw a wide variety of precipitating features and weather patterns (Sobel et al. 2020; Chudler and Rutledge 2021). Ideally one could compare a timeseries of SEA-POL rain volume to KuPR rain volume, and examine the differences between the two fields over time. Unfortunately, the very limited number of KuPR overpasses (26) precludes a meaningful analysis. However, using the broader statistics presented in this section so far on how KuPR represents precipitation features of different sizes, it is possible to approximate what KuPR might detect for a given SEA-POL scan. Thus, a timeseries of simulated KuPR rain volume can be obtained and compared to SEA-POL.

The method used for simulated KuPR rain volume is now discussed. First, for every SEA-POL scan, every unique precipitation feature was identified, and their individual mean rain rates calculated. Each precipitating feature was then assigned a percentile based on how its rain rate compared to SEA-POL features of similar size. For example, if a feature had an area of 500 km^2 and a mean rain rate of 7 mm hr^{-1}, this corresponds to approximately the 75^{th} percentile of rain rates in the associated size bin (see Figure 4.12). Next, the rain rate value equal to that percentile of KuPR mean rain rates in the same size bin was selected as the mean rain rate for the simulated KuPR feature. To account for the KuPR's tendency to increase feature area, the SEA-POL feature was then downsampled to the KuPR resolution of 5x5 km. This method for simulating KuPR raining area was subjectively analyzed by comparing downsampled SEA-POL scans to KuPR scans for the direct overpass cases, and was found to be quite effective. The area of the feature in the down sampled SEA-POL data was determined and multiplied by the simulated KuPR rain rate to derive a simulated KuPR rain volume. The procedure was then repeated for every SEA-POL feature in every scan, thus allowing a timeseries of simulated KuPR rain volume to be computed.

A timeseries of the difference between SEA-POL rain volume and the simulated KuPR rain volume is shown in Figure 4.13, along with the total precipitation area seen by SEA-POL at each time. Generally, periods when KuPR rain volume is less than SEA-POL are associated with small precipitating areas, and periods when KuPR is greater occur when the precipitating area is large. In scans where KuPR underestimated (overestimated) SEA-POL rain volume by more than 50%, the average precipitating area was 171 km^2 (3148 km^2). This supports conclusions drawn previously in this study. When precipitating area is low, this may generally be associated with small, isolated convection. This small convection typically has intense, narrow cores of heavy rain, which KuPR cannot resolve. Thus, rain rate is underestimated during these periods. Conversely,

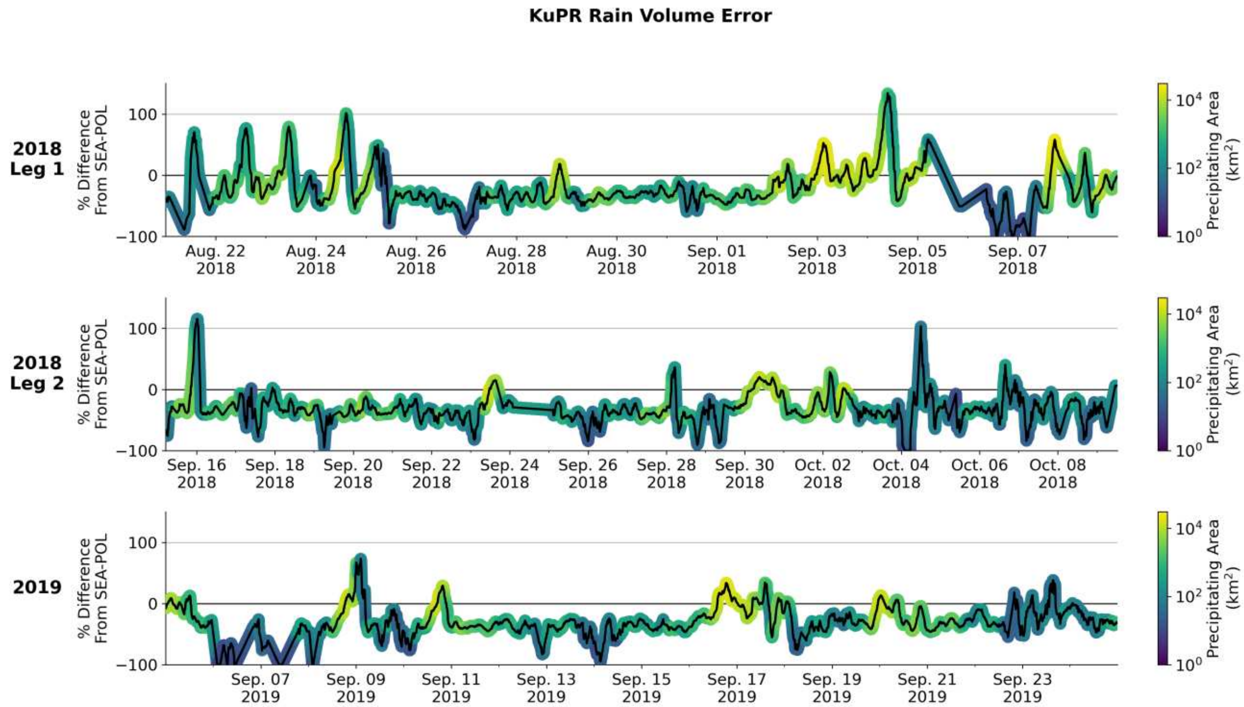

Figure 4.13: Timeseries of the percent difference between SEA-POL rain volume and simulated KuPR rain volume during PISTON. The colors behind the black line show the total precipitating area measured at each SEA-POL scan

when precipitating area is large, there are typically large regions of stratiform rain with bright bands, which may lead to KuPR overestimating rain.

There are many other factors at play other than precipitating area which govern KuPR's rain estimation, so while the above paragraph generally describes the pattern seen in Figure 4.13, there are several notable exceptions. First, during a few periods of KuPR overestimation (e.g., August 24 2018, September 4 2018, September 8-9 2019), an interesting trend is noted where precipitating area is high as KuPR overestimation commences, but then begins to decrease as the overestimation peaks. This may have to do with the coverage of convective and stratiform rain in SEA-POL's field of view during these events. For example, at 10 UTC on August 24, 2018, the leading convective edge of a large mesoscale convective system moved into SEA-POL's range from the east (Figure 4.14a). While precipitating area was large, the leading convective line was visible to SEA-POL, in addition to several scattered isolated cells out to the northwest of the line, both of which KuPR may have trouble representing. However, once the leading convective line moved into the blanked sector, what remained was a broad area of stratiform rain (Figure 4.14b). While total precipitation coverage was less, this was when KuPR overestimation of rainfall peaked. It may be that KuPR rain volume error is more correlated with *stratiform* rain coverage than total precipitation coverage. In stratiform rain, rain fall variability is minimal (which KuPR may miss if present). KuPR also has a tendency to overcorrect for attenuation. Indeed, most of the other periods with modest precipitation coverage but notable KuPR overestimation of rain volume (e.g., September 23-24, 2019) were found to be associated with broad areas of light-to-moderate stratiform rain.

In addition to examining how KuPR accuracy varies with precipitation area, this method can also be used to assess how KuPR performs in different environmental conditions. During PISTON 2018, multiple easterly waves moved through the operations region. Both Petersen et al.

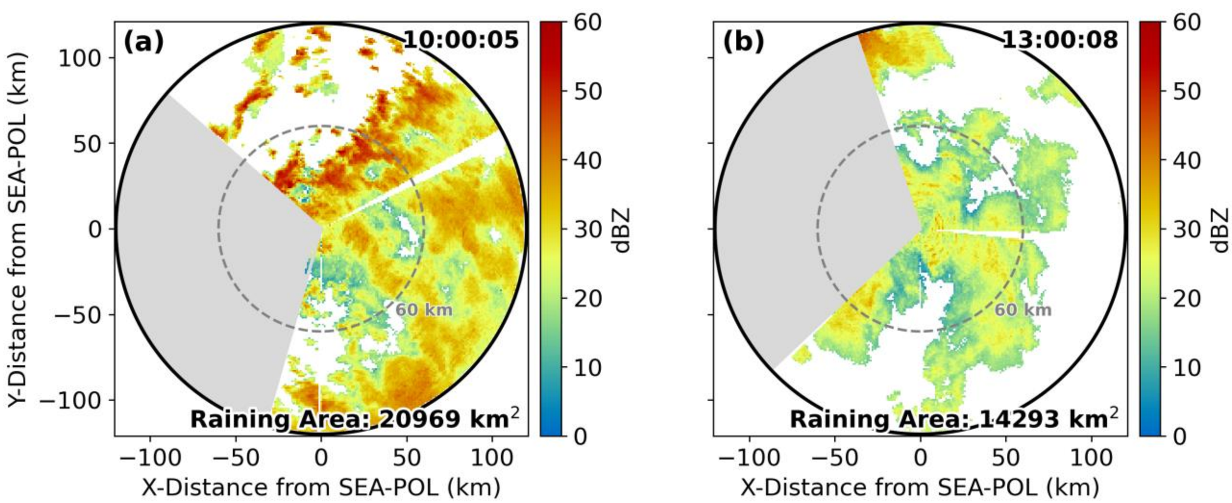

Figure 4.14: A mesoscale convective system observed by SEA-POL during PISTON.

(2003) and Chudler and Rutledge (2021) found that ridges of these waves were associated with small, isolated precipitation features, and troughs were associated with large mesoscale convective systems with broad areas of stratiform precipitation. Using the wave phase classification algorithm outlined in that study, SEA-POL and simulated KuPR rain volume timeseries were composited by phase. It was found that during easterly wave ridges, simulated KuPR rain volume underestimated SEA-POL by 37%, while during ridges, it only underestimated by 9%. These numbers follow previous observed patterns – rain is missed by KuPR when it is contained within small cores, and KuPR rainfall is higher than SEA-POL in large stratiform systems with bright bands. It should be noted that for this analysis, the exact magnitude of the under/overestimation of KuPR is only a rough estimate and may be different from how a true KuPR scan would compare to SEA-POL. Rather, what is more important is the numbers relative to each other under different conditions (i.e., ridge vs. trough, large vs. small precipitating area). The validity of this KuPR-simulating method is indicated by the fact that these comparisons lead to conclusions which are corroborated by other analyses in this study.

4.4 Conclusions

In this study, we have utilized the PISTON SEA-POL dataset to assess the performance of the GPM KuPR over the open tropical waters of the western North Pacific. This assessment was carried out with two distinct methods – direct comparison of the limited number of overpasses of KuPR over the SEA-POL radar, and comparison of the bulk statistics of precipitation features from each radar. Broadly, it was found that KuPR measurements of rain volume agreed reasonably well with those of SEA-POL, but that this apparent accuracy agreement may be in part due to two separate errors of opposite signs. Specifically, we have shown that the limited horizontal resolution of KuPR (5 km x 5 km) causes it to underestimate the rain rate within small convective cores (leading to less rain volume), but also causes precipitation features to be broadened beyond their true areal extent (leading to more rain volume). Additionally, it was found that KuPR has anomalously high reflectivity below radar bright bands, and that while the internal rain rate algorithm appears to mostly correct for this (based on a comparison of SEA-POL/KuPR reflectivity differences and rain rate differences), rain rates in large systems with bright bands were still slightly higher in KuPR than in SEA-POL.

Over the course of all PISTON cruises, there were a total of 18 incidences when the KuPR radar swath intersected with the SEA-POL coverage area and made simultaneous measurements of precipitation. By comparing these matched scans (Figure 4.4), it was found that KuPR typically has lower rain rates than SEA-POL. On average, the scan-average rain rate was 50% lower in KuPR than in SEA-POL, with the discrepancy between the two radars being the largest in situations with heavier rain (KuPR underestimates by 70% when the SEA-POL scan-max rain rate is greater than 2.5 mm h^{-1}). Although KuPR underestimated rain rate, it tended to *over*estimate total precipitating area. Together, the combined effect of underestimation of rain rates and overestimation of raining area led to KuPR having slightly higher total rain volume than SEA-POL. Over all 18 matched scans, KuPR saw 23% more rain volume than SEA-POL.

Precipitation statistics were then compared between individual precipitation features seen by both radars (Figure 4.6). For regions outlined by SEA-POL precipitation features, KuPR typically completely filled in these regions with reflectivity. The exception to this was very small features (< 25 km^2), for which KuPR often did not fully detect or only partially filled in. Mean rain rate from KuPR was also typically lower than SEA-POL within SEA-POL feature regions. As a result, KuPR typically underestimated the rain volume of SEA-POL features. In contrast, when features were defined by their extent on the KuPR scans, KuPR typically saw more rain volume than SEA-POL. This is because regions outlined by KuPR features typically contained a significant amount of non-raining area on the matching SEA-POL scan. KuPR tended to over-broaden features, so a given raining region from KuPR usually had more rain volume within it than the same region in SEA-POL, despite a reduced mean rain rate.

These results were supported when looking in detail at cluster of small isolated cells (Figure 4.7,Figure 4.8) and a large rain band (Figure 4.9Figure 4.10) which were observed by both radars. For the isolated cells, KuPR was able to capture the weaker southern cell fairly well, but struggled to resolve the narrow band of intense rain in the northern cell, where rain volume was 30% lower than SEA-POL. For the large rain band, KuPR rain volume was 21% higher than SEAPOL. 61% of that difference was attributed to KuPR seeing more precipitating area, and 39% was attributed to KuPR rain rates being slightly higher. These increased rain rates are hypothesized to be due to overcorrection of attenuation beneath a bright band (Wang and Wolff 2009; Louf et al. 2019), which was confirmed to be present through examination of vertical cross sections of the radar data.

The findings discussed above were corroborated by a statistical analysis of a large dataset precipitation features observed by both radars. All KuPR scans which passed through the PISTON area during the field campaign were collected (regardless of if they passed over SEA-POL or not). Using a unique resampling method (Figure 4.2), scans were broken down into sub-samples which matched the SEA-POL scanning area, allowing for the sampling rate of different sized features to be approximately equal between radars (Figure 4.11a). Compared to SEA-POL, KuPR was shown to have less rain volume contribution from small features and more contribution from large features (Figure 4.11b). The former is due to KuPR's underestimation of rain rate in small features (due to its resolution), and the latter is due to overestimation of rain rate in large features (due to overcorrection of attenuation), as well as KuPR's tendency to increase feature area.

Finally, a novel method to simulate KuPR rain volume for a provided SEA-POL scan was presented and used estimate KuPR‘s performance compared to SEA-POL and how it varied over the course of PISTON (Figure 4.13). It was found that KuPR rainfall was more likely to overestimate rain volume during trough phases of easterly waves and during times when there was more total precipitating area, and was more likely to underestimate rainfall during ridge phases and when there was less precipitating area.

In summary, the main conclusions of this study are

1. The 5x5 km horizontal resolution of KuPR limits is ability to resolve heavy rain within small convective cores. In some instances, it may underestimate rain rate by up to 70%.
2. This low resolution also causes precipitation features to appear larger to KuPR than they are in reality. If the edge of a feature falls within a KuPR grid box, KuPR tends to mark that entire box as having precipitation, broadening the edges of the feature.
3. KuPR also tends to have higher rain rates than SEA-POL in large precipitation features, likely due to overcorrection of attenuation below bright bands.

It should also be noted that while this study utilized SEA-POL data which had been interpolated onto a 1x1 km horizontal grid, which is at a 25x higher resolution than KuPR (5x5 km), the original polar SEA-POL data is in fact obtained at an even finer resolution (100 m radial, 1 degree azimuthal gate spacing). While it is not examined in this study, it is expected that the difference in ability to resolve small convective cores would be even more noticeable if comparing KuPR to the full resolution SEA-POL data.

While the model used in this study to simulate KuPR rain volume for given SEA-POL scan was useful and provided sensible results, it is rather simple in the sense that it only takes in mean feature rain rate and feature area as inputs. A more complex model which takes in additional variables, such as maximum rain rate, convective/stratiform partitioning, environmental parameters, etc. may be able to produce more accurate results. The primary issue in developing such a model is the very limited training/verification dataset provided by the 26 KuPR overpasses. However, through careful application of the statistics presented in Section 4.3.2, as well as dividing the matched scans in to smaller but more numerous samples, it is possible that a more accurate model could be developed. Such a model would be quite beneficial in assessing KuPR accuracy, and could theoretically be adapted to simulate KuPR rain volume for any radar scan, beyond those taken during PISTON.

Chapter 5: Conclusions

5.1 Summary

In this dissertation, convection in the western North Pacific observed during the PISTON field campaign has been rigorously examined in several ways. Convection and precipitation in the tropics impact the environment by altering latent heating profiles (Cifelli and Rutledge 1998, Schumacher et al. 2007), momentum transport (LeMone 1983, LeMone et al. 1984), air/ocean heat fluxes (Gaynor and Ropelewski 1979, Jabouille et al. 1996, Saxen and Rutledge 1998), and other parameters, and can drive large-scale circulations which impact weather globally. Consequently, tropical convection has been an active area of research for many years, and has motivated numerous field campaigns to operate in oceanic regions where scientific observations are otherwise hard to come by. The present works builds upon previous research in the field by combining the unique PISTON radar dataset with several other data sources to make novel observations and conclusions about convective systems in an important region which has been relatively under-studied by past field campaigns.

In Chapter 2, the different types of precipitation features observed by SEA-POL were analyzed. It was found that despite only being present in 13% of SEA-POL scans, large MCSs (> 2000 km^2) produced over half (56%) of the total rain volume. Larger features had higher mean rain rates and produced these rain rates over a broader region, thus contributing a disproportionate amount of rain relative to their occurrence rate. On the other hand, the smallest features (length < 20 km), contributed 11% of the total rain volume. Despite their small raining areas their high occurrence frequency (91% of scans) and intense convective cores allowed for a significant contribution to the total precipitation. The rain volume contribution of isolated cells is small but certainly not insignificant, which has implications for weather models and satellite radars (see Chapter 4) which may not be able to accurately resolve these small features.

Chapter 2 also examined how precipitation feature morphology related to the large-scale environment. Southwesterly wind regimes, which are associated with high midtropospheric moisture content and significant low-level wind shear, were shown to be associated with a higher occurrence of large MCS precipitation features. Other wind regimes featured all morphologies at approximately equal frequencies. In looking at easterly wave phases, it was determined that wave troughs brought anomalously moist conditions and an increase the number of large MCSs, while ridge periods brought dry conditions and an increase in the number of small, isolated features.

Chapter 3 investigated a unique radar signature seen by SEA-POL during PISTON. During the cruises, it was noted that shallow convection typically had extremely high values of differential reflectivity (Z_{dr}) in their cores (> 3.5 dB), which is associated with large drops (> 4.5 mm in diameter). These observations were regularly made in cells with echo tops below the freezing level, suggesting the drops were formed through warm rain processes. These cells were small (mean area of 8 km^2), and short-lived (usually < 10 minutes). The high Z_{dr} signature preferentially formed on the upwind side of storms suggesting that either large drops were contained to upwind locations, or that the downwind side contained a higher concentration of smaller drops which masked the high Z_{dr} signature. Z_{dr} also tended to be larger at lower levels within these cells, likely due to a combination of drops growing through coalescence as they fall, and higher temperature at lower levels (increasing the dielectric content). These findings were supported by scattering simulations, theoretical drop growth models, in-situ aircraft measurements, and analysis of an individual case study.

Finally, Chapter 3 compared observations of precipitation from SEA-POL and the Global Precipitation Mission (GPM) Ku-Band weather radar (KuPR). During PISTON, there were 18 instances of SEA-POL and KuPR making concurrent measurements of precipitation. Comparison of these matched scans revealed that KuPR rain rate measurements were frequently significantly less than SEA-POL, particularly when SEA-POL measured extreme rain rates in convective cores. This is due to KuPR's limited horizontal resolution (5x5 km) compared to the gridded SEA-POL data (1x1 km). SEA-POL typically sees the highest rain rate in narrow cores < 5 km wide, which KuPR is unable to fully resolve. Interestingly, this resolution difference also likely led KuPR to overestimate feature size. Edges of storms appeared to be expanded beyond their true extent in the KuPR scans, leading KuPR to typically have more precipitating area than SEA-POL in matched scans. The combination of KuPR having lower rain rates than SEA-POL but a higher raining area led to KuPR having slightly more rain volume than SEA-POL. Across all 18 matched scans, KuPR saw 23% more rain volume than SEA-POL. It was also discovered that KuPR has a tendency to slightly overestimate rain rate in large MCS features, due to overcorrection of attenuation below the melting level/radar bright band.

Chapter 3 also compared the broad statistics of precipitation features observed by SEA-POL and KuPR, regardless of if the features were concurrently sampled. It was demonstrated that, compared to SEA-POL, KuPR has less rain volume contribution from small features and more from large features. The former was attributed to KuPR's underestimation of rain rate in small features (due to its resolution), and the latter was attributed to its overestimation of rain rate in large features with bright bands (due to overcorrection of attenuation), as well as KuPR's tendency to increase feature area. Using these statistics, a novel method to simulate KuPR rain volume for a provided SEA-POL scan was presented and used to estimate what a rainfall comparison between the two radars would look like throughout PISTON. It was found that simulated KuPR rainfall was typically higher than SEA-POL when there was more total precipitating area on scope, and lower than SEA-POL when there was less precipitating area.

5.2 Future Work

The work presented in this dissertation lays a foundation for several avenues of future research. For example, although Chapter 2 only examined precipitation features seen by SEA-POL during PISTON, it also linked the morphology of these features to broader environmental conditions and synoptic patterns. Analysis on the frequency at which these conditions and patterns occur in the western North Pacific could lead to insights on the broader-scale impacts of this convection on the atmosphere.

The study of shallow convection with large drops presented in Chapter 3 was somewhat hampered by the fact that PISTON was not specifically designed to study such storms. The scanning strategy using by SEA-POL was sub-optimal for studying these cells, and polarimetric radar data can only provide so much information about drop size distributions. Several questions remain as to how these large drops form, what environmental conditions they form in, and how they in turn impact the environment. A field campaign designed specifically to measure large drops in shallow convection (i.e., one with targeted aircraft penetrations and a more optimal SEA-POL scanning strategy) is required to address these questions.

Finally, the model presented in Chapter 4 for estimating KuPR rain volume for a given SEA-POL scan, while useful, was a relatively simple model which only took in a few parameters for its prediction. The statistical analyses also presented in Chapter 4 could certainly serve as groundwork for developing a more complex model which ingests more prediction variables. Such a model could even be adapted to estimate KuPR rain volume for any given radar scan (not just from SEA-POL), and could be valuable for future KuPR validation studies.

References

A. H. Sobel, S. E. Yuter, C. S. Bretherton, and G. N. Kiladis, 2004: Large-scale meteorology and deep convection during TRMM KWAJEX. *Mon. Wea. Rev.*, **132**, 422–444, https://doi.org/10.1175/1520-0493(2004)132<0422:LMADCD>2.0.CO;2.

A. Thorpe, M. Miller, and M. Moncrieff, 1982: Two-dimensional convection in non-constant shear: A model of mid-latitude squall lines. *Quart. J. Roy. Meteor. Soc.*, **108**, 739–762, https://doi.org/10.1002/qj.49710845802.

B. Wang and X. Xie, 1997: A model for the boreal summer intraseasonal oscillation. *J. Atmos. Sci.*, **54**, 72–86, https://doi.org/10.1175/1520-0469(1997)054<0072:AMFTBS>2.0.CO;2.

Battaglia, A., S. Tanelli, S. Kobayashi, D. Zrnic, R. J. Hogan, and C. Simmer, 2010: Multiple-scattering in radar systems: A review. *Journal of Quantitative Spectroscopy and Radiative Transfer*, **111**, 917–947, https://doi.org/10/cdd9xn.

——, ——, G. M. Heymsfield, and L. Tian, 2014: The Dual Wavelength Ratio Knee: A Signature of Multiple Scattering in Airborne Ku–Ka Observations. *Journal of Applied Meteorology and Climatology*, **53**, 1790–1808, https://doi.org/10/f58xhs.

Beard, K. V., and C. Chuang, 1987: A New Model for the Equilibrium Shape of Raindrops. *J. Atmos. Sci.*, **44**, 1509–1524, https://doi.org/10.1175/1520-0469(1987)044<1509:ANMFTE>2.0.CO;2.

——, D. B. Johnson, and D. Baumgardner, 1986: Aircraft observations of large raindrops in warm, shallow, convective clouds. *Geophys. Res. Lett.*, **13**, 991–994, https://doi.org/10.1029/GL013i010p00991.

Berry, E. X., and R. L. Reinhardt, 1974: An Analysis of Cloud Drop Growth by Collection: Part I. Double Distributions. *J. Atmos. Sci.*, **31**, 1814–1824, https://doi.org/10.1175/1520-0469(1974)031<1814:AAOCDG>2.0.CO;2.

Brandes, E. A., G. Zhang, and J. Vivekanandan, 2002: Experiments in Rainfall Estimation with a Polarimetric Radar in a Subtropical Environment. *J. Appl. Meteor.*, **41**, 674–685, https://doi.org/10/bfxgg2.

Brenguier, J.-L., H. Pawlowska, L. Schüller, R. Preusker, J. Fischer, and Y. Fouquart, 2000: Radiative Properties of Boundary Layer Clouds: Droplet Effective Radius versus Number Concentration. *J. Atmos. Sci.*, **57**, 803–821, https://doi.org/10/cdb83s.

Bringi, V. N., and V. Chandrasekar, 2001: *Polarimetric Doppler Weather Radar: Principles and Applications*. 1st ed. Cambridge University Press,.

Bringi, V. N., V. Chandrasekar, P. Meischner, J. Hubbert, and Y. Golestani, 1991: Polarimetric radar signatures of precipitation at S and C-bands. *IEE Proc. F Radar Signal Process. UK*, **138**, 109, https://doi.org/10/bj62dg.

Bringi, V. N., V. Chandrasekar, J. Hubbert, E. Gorgucci, W. L. Randeu, and M. Schoenhuber, 2003: Raindrop Size Distribution in Different Climatic Regimes from Disdrometer and Dual-Polarized Radar Analysis. *J. Atmos. Sci.*, **60**, 354–365, https://doi.org/10/fm62vd.

——, C. R. Williams, M. Thurai, and P. T. May, 2009: Using Dual-Polarized Radar and Dual-Frequency Profiler for DSD Characterization: A Case Study from Darwin, Australia. *Journal of Atmospheric and Oceanic Technology*, **26**, 2107–2122, https://doi.org/10/dfn364.

C. Chang, 1970: Westward propagating cloud patterns in the tropical Pacific as seen from time-composite satellite photographs. *J. Atmos. Sci.*, **27**, 133–138, https://doi.org/10.1175/1520-0469(1970)027<0133:WPCPIT>2.0.CO;2.

C. D. Thorncroft and B. J. Hoskins, An idealized study of African easterly waves. I: A linear view. *Quart. J. Roy. Meteor. Soc.*, **120**, 953–982, https://doi.org/10.1002/qj.49712051809.

—— and ——, An idealized study of African easterly waves. II: A nonlinear view. *Quart. J. Roy. Meteor. Soc.*, **120**, 983–1015, https://doi.org/10.1002/qj.49712051810.

C. Liu and E. Zipser, 2013: Regional variation of morphology of organized convection in the tropics and subtropics. *J. Geophys. Res.*, **118**, 453–466, https://doi.org/10.1029/2012JD018409.

C. Schumacher and R. A. Houze, 2003: The TRMM Precipitation Radar's view of shallow, isolated rain. *J. Appl. Meteor.*, **42**, 1519–1524, https://doi.org/10.1175/1520-0450(2003)042<1519:TTPRVO>2.0.CO;2.

Carey, L. D., and W. A. Petersen, 2015: Sensitivity of C-Band Polarimetric Radar–Based Drop Size Estimates to Maximum Diameter. *Journal of Applied Meteorology and Climatology*, **54**, 1352–1371, https://doi.org/10/gncz8q.

Chudler, K., and S. A. Rutledge, 2021: THE COUPLING BET WEEN CONVECTIVE VARIABILITY AND LARGE-SCALE FLOW PATTERNS OBSERVED DURING PISTON 2018-2019. *Journal of Climate*, 1–57, https://doi.org/10/gnc2js.

——, W. Xu, and S. A. Rutledge, 2020: Impact of the Boreal Summer Intraseasonal Oscillation on the Diurnal Cycle of Precipitation near and over the Island of Luzon. *Monthly Weather Review*, **148**, 1805–1827, https://doi.org/10/gnc2jt.

Ciesielski, P. E., and Coauthors, 2014: Quality-Controlled Upper-Air Sounding Dataset for DYNAMO/CINDY/AMIE: Development and Corrections. *Journal of Atmospheric and Oceanic Technology*, **31**, 741–764, https://doi.org/10/f5xth9.

D. L. Hartmann, H. H. Hendon, and R. A. Houze, 1984: Some implications of the mesoscale circulations in tropical cloud clusters for large-scale dynamics and climate. *J. Atmos. Sci.*, **41**, 113–121, https://doi.org/10.1175/1520-0469(1984)041<0113:SIOTMC>2.0.CO;2.

D'Adderio, L. P., G. Vulpiani, F. Porcù, A. Tokay, and R. Meneghini, 2018: Comparison of GPM Core Observatory and Ground-Based Radar Retrieval of Mass-Weighted Mean Raindrop Diameter at Midlatitude. *Journal of Hydrometeorology*, **19**, 1583–1598, https://doi.org/10/gfhn7x.

Dixon, M., and G. Wiener, 1993: TITAN: Thunderstorm Identification, Tracking, Analysis, and Nowcasting—A Radar-based Methodology. *J. Atmos. Oceanic Technol.*, **10**, 785–797, https://doi.org/10/dc5g2t.

Dolan, B., B. Fuchs, S. A. Rutledge, E. A. Barnes, and E. J. Thompson, 2018: Primary Modes of Global Drop Size Distributions. *J. Atmos. Sci.*, **75**, 1453–1476, https://doi.org/10/gdqxx3.

E. D. Maloney and M. J. Dickinson, 2003: The intraseasonal oscillation and the energetics of summertime tropical western North Pacific synoptic-scale disturbances. *J. Atmos. Sci.*, **60**, 2153–2168, https://doi.org/10.1175/1520-0469(2003)060<2153:TIOATE>2.0.CO;2.

E. J. Thompson, J. N. Moum, C. W. Fairall, and S. A. Rutledge, 2019: Wind limits on rain layers and diurnal warm layers. *J. Geophys. Res. Oceans*, **124**, 897–924, https://doi.org/10.1029/2018JC014130.

Fridlind, A. M., and Coauthors, 2019: Use of polarimetric radar measurements to constrain simulated convective cell evolution: a pilot study with Lagrangian tracking. *Atmos. Meas. Tech.*, **12**, 2979–3000, https://doi.org/10/gncz8r.

G. Medioni, M. Lee, and C. Tang, 2000: *A Computational Framework for Segmentation and Grouping*. Elsevier, 284 pp.

G. N. Kiladis, C. D. Thorncroft, and N. M. J. Hall, 2006: Three-dimensional structure and dynamics of African easterly waves. Part I: Observations. *J. Atmos. Sci.*, **63**, 2212–2230, https://doi.org/10.1175/JAS3741.1.

Gao, Y., T. Wu, J. Wang, and S. Tang, 2021: Evaluation of GPM Dual-Frequency Precipitation Radar (DPR) Rainfall Products Using the Rain Gauge Network over China. *Journal of Hydrometeorology*, **22**, 547–559, https://doi.org/10/gnc2jv.

Gatlin, P. N., M. Thurai, V. N. Bringi, W. Petersen, D. Wolff, A. Tokay, L. Carey, and M. Wingo, 2015: Searching for Large Raindrops: A Global Summary of Two-Dimensional Video Disdrometer Observations. *Journal of Applied Meteorology and Climatology*, **54**, 1069–1089, https://doi.org/10/f7ccm8.

Geoffroy, O., J.-L. Brenguier, and I. Sandu, 2008: Relationship between drizzle rate, liquid water path and droplet concentration at the scale of a stratocumulus cloud system. *Atmos. Chem. Phys.*, **8**, 4641–4654, https://doi.org/10/fvmsf6.

Gunn, R., and G. D. Kinzer, 1949: THE TERMINAL VELOCITY OF FALL FOR WATER DROPLETS IN STAGNANT AIR. *J. Meteor.*, **6**, 243–248, https://doi.org/10/dp8zt4.

H. Hersbach, 2020: The ERA5 global reanalysis. **146**, 1999–2049, https://doi.org/10.1002/qj.3803.

H. Ramsay, 2017: *The Global Climatology of Tropical Cyclones*. Oxford Research Encyclopedia of Natural Hazard Science,.

H. Yamada, K. Yoneyama, M. Katsumata, and R. Shirooka, 2010: Observations of a super cloud cluster accompanied by synoptic-scale eastward-propagating precipitating systems over the Indian Ocean. *J. Atmos. Sci.*, **67**, 1456–1473, https://doi.org/10.1175/2009JAS3151.1.

Hamada, A., and Y. N. Takayabu, 2016: Improvements in Detection of Light Precipitation with the Global Precipitation Measurement Dual-Frequency Precipitation Radar (GPM DPR). *Journal of Atmospheric and Oceanic Technology*, **33**, 653–667, https://doi.org/10/f8nsht.

Hardin, J., 2014: *Pydisdrometer V1.0*. Zenodo,.

Hartmann, D. L., and D. A. Short, 1980: On the Use of Earth Radiation Budget Statistics for Studies of Clouds and Climate. *J. Atmos. Sci.*, **37**, 1233–1250, https://doi.org/10/csbhw3.

Hayden, L., and C. Liu, 2018: A Multiyear Analysis of Global Precipitation Combining CloudSat and GPM Precipitation Retrievals. *Journal of Hydrometeorology*, **19**, 1935–1952, https://doi.org/10/gfr7g6.

Hobbs, P. V., and A. L. Rangno, 2004: Super-large raindrops: SUPER-LARGE RAINDROPS. *Geophys. Res. Lett.*, **31**, n/a-n/a, https://doi.org/10/dtf2hq.

Hou, A. Y., and Coauthors, 2014: The Global Precipitation Measurement Mission. *Bull. Amer. Meteor. Soc.*, **95**, 701–722, https://doi.org/10/f59753.

Houze, R. A., D. C. Wilton, and B. F. Smull, 2007: Monsoon convection in the Himalayan region as seen by the TRMM Precipitation Radar. *Q.J.R. Meteorol. Soc.*, https://doi.org/10/dv62cb.

I. Bladé and D. L. Hartmann, 1993: Tropical intraseasonal oscillations in a simple nonlinear model. *J. Atmos. Sci.*, **50**, 2922–2939, https://doi.org/10.1175/1520-0469(1993)050<2922:TIOIAS>2.0.CO;2.

Igel, M. R., and S. C. van den Heever, 2015: The relative influence of environmental characteristics on tropical deep convective morphology as observed by CloudSat: MORPHOLOGICAL SENSITIVITY TO ENVIRONMENT. *J. Geophys. Res. Atmos.*, **120**, 4304–4322, https://doi.org/10/gncz8w.

Iguchi, T., T. Kozu, R. Meneghini, J. Awaka, and K. Okamoto, 2000: Rain-Profiling Algorithm for the TRMM Precipitation Radar. *J. Appl. Meteor.*, **39**, 2038–2052, https://doi.org/10/cxjbxr.

J. B. Edson, 2013: On the exchange of momentum over the open ocean. *J. Phys. Oceanogr.*, **43**, 1589–1610, https://doi.org/10.1175/JPO-D-12-0173.1.

J. C. Beattie and R. L. Elsberry, 2012: Western North Pacific monsoon depression formation. *Wea. Forecasting*, **27**, 1413–1432, https://doi.org/10.1175/WAF-D-11-00094.1.

J. Lee, B. Wang, M. C. Wheeler, X. Fu, D. E. Waliser, and I. Kang, 2013: Real-time multivariate indices for the boreal summer intraseasonal oscillation over the Asian summer monsoon region. *Climate Dyn.*, **40**, 493–509, https://doi.org/10.1007/s00382-012-1544-4.

J. Molinari, D. Knight, M. Dickinson, D. Vollaro, and S. Skubis, 1997: Potential vorticity, easterly waves, and eastern Pacific tropical cyclogenesis. *Mon. Wea. Rev.*, **125**, 2699–2708, https://doi.org/10.1175/1520-0493(1997)125<2699:PVEWAE>2.0.CO;2.

J. Moon, B. Wang, K. Ha, and J. Lee, 2013: Teleconnections associated with Northern Hemisphere summer monsoon intraseasonal oscillation. *Climate Dyn.*, **40**, 2761–2774, https://doi.org/10.1007/s00382-012-1394-0.

J. S. Godfrey, R. A. Houze, R. H. Johnson, R. Lukas, J.-L. Redelsperger, A. Sumi, and R. Weller, 1998: Coupled Ocean–Atmosphere Response Experiment (COARE): An interim report. *J. Geophys. Res.*, **103**, 14395–14450, https://doi.org/10.1029/97JC03120.

J. Tan, G. J. Huffman, D. T. Bolvin, and E. J. Nelkin, 2019: IMERG V06: Changes to the morphing algorithm. *J. Atmos. Oceanic Technol.*, **36**, 2471–2482, https://doi.org/10.1175/JTECH-D-19-0114.1.

J. W. Whitaker and E. D. Maloney, 2020: Genesis of an East Pacific easterly wave from a Panama Bight MCS: A case study analysis from June 2012. *J. Atmos. Sci.*, **77**, 3567–3584, https://doi.org/10.1175/JAS-D-20-0032.1.

Johnson, R. H., T. M. Rickenbach, S. A. Rutledge, P. E. Ciesielski, and W. H. Schubert, 1999: Trimodal Characteristics of Tropical Convection. *J. Climate*, **12**, 2397–2418, https://doi.org/10/dp32f5.

K.-H. Lau and N.-C. Lau, 1990: Observed structure and propagation characteristics of tropical summertime synoptic scale disturbances. *Mon. Wea. Rev.*, **118**, 1888–1913, https://doi.org/10.1175/1520-0493(1990)118<1888:OSAPCO>2.0.CO;2.

—— and ——, 1992: The energetics and propagation dynamics of tropical summertime synoptic-scale disturbances. *Mon. Wea. Rev.*, **120**, 2523–2539, https://doi.org/10.1175/1520-0493(1992)120<2523:TEAPDO>2.0.CO;2.

Knapp, K. R., H. J. Diamond, J. P. Kossin, M. C. Kruk, and C. J. Schreck, 2018: International Best Track Archive for Climate Stewardship (IBTrACS) Project, Version 4. https://doi.org/10.25921/82TY-9E16.

Kodama, Y.-M., M. Katsumata, S. Mori, S. Satoh, Y. Hirose, and H. Ueda, 2009: Climatology of Warm Rain and Associated Latent Heating Derived from TRMM PR Observations. *Journal of Climate*, **22**, 4908–4929, https://doi.org/10/dhkmch.

Kozu, T., and Coauthors, 2001: Development of precipitation radar onboard the Tropical Rainfall Measuring Mission (TRMM) satellite. *IEEE Trans. Geosci. Remote Sensing*, **39**, 102–116, https://doi.org/10/bqqpzh.

Kumjian, M. R., and A. V. Ryzhkov, 2012: The Impact of Size Sorting on the Polarimetric Radar Variables. *Journal of the Atmospheric Sciences*, **69**, 2042–2060, https://doi.org/10/f32ncs.

Kummerow, C., and Coauthors, 2000: The Status of the Tropical Rainfall Measuring Mission (TRMM) after Two Years in Orbit. *J. Appl. Meteor.*, **39**, 1965–1982, https://doi.org/10/bprz28.

L. A. Avila and R. J. Pasch, 1992: Atlantic tropical systems of 1991. *Mon. Wea. Rev.*, **120**, 2688–2696, https://doi.org/10.1175/1520-0493(1992)120<2688:ATSO>2.0.CO;2.

L. J. Donner, C. J. Seman, and R. S. Hemler, 1999: Three-dimensional cloud-system modeling of GATE convection. *J. Atmos. Sci.*, **56**, 1885–1912, https://doi.org/10.1175/1520-0469(1999)056<1885:TDCSMO>2.0.CO;2.

Lau, K. M., and H. T. Wu, 2003: Warm rain processes over tropical oceans and climate implications: WARM RAIN PROCESSES OVER TROPICAL OCEANS. *Geophys. Res. Lett.*, **30**, https://doi.org/10/bqb77r.

Lawson, R. P., S. Woods, and H. Morrison, 2015: The Microphysics of Ice and Precipitation Development in Tropical Cumulus Clouds. *Journal of the Atmospheric Sciences*, **72**, 2429–2445, https://doi.org/10/f7c3dk.

Lin, X., and R. H. Johnson, 1996: Heating, Moistening, and Rainfall over the Western Pacific Warm Pool during TOGA COARE. *J. Atmos. Sci.*, **53**, 3367–3383, https://doi.org/10/fd49rp.

Louf, V., A. Protat, R. A. Warren, S. M. Collis, D. B. Wolff, S. Raunyiar, C. Jakob, and W. A. Petersen, 2019: An Integrated Approach to Weather Radar Calibration and Monitoring Using Ground Clutter and Satellite Comparisons. *Journal of Atmospheric and Oceanic Technology*, **36**, 17–39, https://doi.org/10/gnc2jx.

M. A. LeMone, 1983: Momentum transport by a line of cumulonimbus. *J. Atmos. Sci.*, **40**, 1815–1834, https://doi.org/10.1175/1520-0469(1983)040<1815:MTBALO>2.0.CO;2.

——, G. M. Barnes, and E. J. Zipser, 1984: Momentum flux by lines of cumulonimbus over the tropical oceans. *J. Atmos. Sci.*, **41**, 1914–1932, https://doi.org/10.1175/1520-0469(1984)041<1914:MFBLOC>2.0.CO;2.

——, E. J. Zipser, and S. B. Trier, 1998: The role of environmental shear and thermodynamic conditions in determining the structure and evolution of mesoscale convective systems during TOGA COARE. *J. Atmos. Sci.*, **55**, 3493–3518, https://doi.org/10.1175/1520-0469(1998)055<3493:TROESA>2.0.CO;2.

M. Dickinson and J. Molinari, 2002: Mixed Rossby–gravity waves and western Pacific tropical cyclogenesis. Part I: Synoptic evolution. *J. Atmos. Sci.*, **59**, 2183–2196, https://doi.org/10.1175/1520-0469(2002)059<2183:MRGWAW>2.0.CO;2.

M. L. Weisman and R. Rotunno, 2004: “A theory for strong long-lived squall lines” revisited. *J. Atmos. Sci.*, **61**, 361–382, https://doi.org/10.1175/1520-0469(2004)061<0361:ATFSLS>2.0.CO;2.

——, J. B. Klemp, and R. Rotunno, 1988: Structure and evolution of numerically simulated squall lines. *J. Atmos. Sci.*, **45**, 1990–2013, https://doi.org/10.1175/1520-0469(1988)045<1990:SAEONS>2.0.CO;2.

M. Steiner, R. A. Houze, and S. E. Yuter, 1995: Climatological characterization of three-dimensional storm structure from operational radar and rain gauge data. *J. Appl. Meteor.*, **34**, 1978–2007, https://doi.org/10.1175/1520-0450(1995)034<1978:CCOTDS>2.0.CO;2.

McGill, R., J. W. Tukey, and W. A. Larsen, 1978: Variations of Box Plots. *The American Statistician*, **32**, 12, https://doi.org/10/dsvtxr.

Meneghini, R., H. Kim, L. Liao, J. A. Jones, and J. M. Kwiatkowski, 2015: An Initial Assessment of the Surface Reference Technique Applied to Data from the Dual-Frequency Precipitation Radar (DPR) on the GPM Satellite. *Journal of Atmospheric and Oceanic Technology*, **32**, 2281–2296, https://doi.org/10/f743gm.

Mishchenko, M. I., L. D. Travis, and D. W. Mackowski, 1996: T-matrix computations of light scattering by nonspherical particles: A review. *Journal of Quantitative Spectroscopy and Radiative Transfer*, **55**, 535–575, https://doi.org/10/crbs8c.

Mroz, K., A. Battaglia, T. J. Lang, S. Tanelli, and G. F. Sacco, 2018: Global Precipitation Measuring Dual-Frequency Precipitation Radar Observations of Hailstorm Vertical Structure: Current Capabilities and Drawbacks. *Journal of Applied Meteorology and Climatology*, **57**, 2161–2178, https://doi.org/10/gfbgdw.

N. L. Frank, 1969: The “inverted V” cloud pattern—An easterly wave? *Mon. Wea. Rev.*, **97**, 130–140, https://doi.org/10.1175/1520-0493(1969)097<0130:TVCPEW>2.3.CO;2.

Negri, A. J., T. L. Bell, and L. Xu, 2002: Sampling of the Diurnal Cycle of Precipitation Using TRMM. *J. Atmos. Oceanic Technol.*, **19**, 1333–1344, https://doi.org/10/cs22kd.

Petersen, W. A., R. Cifelli, D. J. Boccippio, S. A. Rutledge, and C. Fairall, 2003: Convection and Easterly Wave Structures Observed in the Eastern Pacific Warm Pool during EPIC-2001. *Journal of the Atmospheric Sciences*, **60**, 1754–1773, https://doi.org/10.1175/1520-0469(2003)060<1754:CAEWSO>2.0.CO;2.

——, P.-E. Kirstetter, J. Wang, D. B. Wolff, and A. Tokay, 2020: The GPM Ground Validation Program. *Satellite Precipitation Measurement*, V. Levizzani, C. Kidd, D.B. Kirschbaum, C.D. Kummerow, K. Nakamura, and F.J. Turk, Eds., Vol. 69 of *Advances in Global Change Research*, Springer International Publishing, 471–502.

Petty, G. W., 1999: Prevalence of Precipitation from Warm-Topped Clouds over Eastern Asia and the Western Pacific. *Journal of Climate*, **12**, 220–229, https://doi.org/10/gmq8xm.

Precipitation Processing System (PPS) At NASA GSFC, 2018: GPM DPR Ku Precipitation Profile 2A 1.5 hours 5 km V06. https://doi.org/10.5067/GPM/DPR/KU/2A/06.

Pruppacher, H. R., and J. D. Klett, 2010: Hydrodynamics of Single Cloud and Precipitation Particles. *Microphysics of Clouds and Precipitation*, Vol. 18 of *Atmospheric and Oceanographic Sciences Library*, Springer Netherlands, 361–446.

R. A. Houze, 1989: Observed structure of mesoscale convective systems and implications for large-scale heating. *Quart. J. Roy. Meteor. Soc.*, **115**, 425–461, https://doi.org/10.1002/qj.49711548702.

——, 1997: Stratiform precipitation in regions of convection: A meteorological paradox? *Bull. Amer. Meteor. Soc.*, **78**, 2179–2196, https://doi.org/10.1175/1520-0477(1997)078<2179:SPIROC>2.0.CO;2.

——, 2004: Mesoscale convective systems. *Rev. Geophys.*, **42**, RG4003, https://doi.org/10.1029/2004RG000150.

——, 2014: *Cloud Dynamics*. Academic Press, 432 pp.

—— and C. Cheng, 1977: Radar characteristics of tropical convection observed during GATE: Mean properties and trends over the summer season. *Mon. Wea. Rev.*, **105**, 964–980, https://doi.org/10.1175/1520-0493(1977)105<0964:RCOTCO>2.0.CO;2.

R. Cifelli and S. A. Rutledge, 1998: Vertical motion, diabatic heating, and rainfall characteristics in north Australia convective systems. *Quart. J. Roy. Meteor. Soc.*, **124**, 1133–1162, https://doi.org/10.1002/qj.49712454806.

R. J. Reed and E. E. Recker, 1971: Structure and properties of synoptic-scale wave disturbances in the equatorial western Pacific. *J. Atmos. Sci.*, **28**, 1117–1133, https://doi.org/10.1175/1520-0469(1971)028<1117:SAPOSS>2.0.CO;2.

R. M. Thompson, S. W. Payne, E. E. Recker, and R. J. Reed, 1979: Structure and properties of synoptic-scale wave disturbances in the intertropical convergence zone of the eastern Atlantic. *J. Atmos. Sci.*, **36**, 53–72, https://doi.org/10.1175/1520-0469(1979)036<0053:SAPOSS>2.0.CO;2.

R. Rotunno, J. B. Klemp, and M. L. Weisman, 1988: A theory for strong, long-lived squall lines. *J. Atmos. Sci.*, **45**, 463–485, https://doi.org/10.1175/1520-0469(1988)045<0463:ATFSLL>2.0.CO;2.

R. W. Burpee, 1972: The origin and structure of easterly waves in the lower troposphere of North Africa. *J. Atmos. Sci.*, **29**, 77–90, https://doi.org/10.1175/1520-0469(1972)029<0077:TOASOE>2.0.CO;2.

——, 1974: Characteristics of North African easterly waves during the summers of 1968 and 1969. *J. Atmos. Sci.*, **31**, 1556–1570, https://doi.org/10.1175/1520-0469(1974)031<1556:CONAEW>2.0.CO;2.

——, 1975: Some features of synoptic-scale waves based on a compositing analysis of GATE data. *Mon. Wea. Rev.*, **103**, 921–925, https://doi.org/10.1175/1520-0493(1975)103<0921:SFOSWB>2.0.CO;2.

Rauber, R. M., K. V. Beard, and B. M. Andrews, 1991: A Mechanism for Giant Raindrop Formation in Warm, Shallow Convective Clouds. *J. Atmos. Sci.*, **48**, 1791–1797, https://doi.org/10/cbsm49.

Rickenbach, T. M., and S. A. Rutledge, 1998: Convection in TOGA COARE: Horizontal Scale, Morphology, and Rainfall Production. *J. Atmos. Sci.*, **55**, 2715–2729, https://doi.org/10/dc4dt2.

Rutledge, S., V. Chandrasekar, B. Fuchs, J. George, F. Junyent, P. Kennedy, and B. Dolan, 2019a: Deployment of the SEA-POL C-band Polarimetric Radar to SPURS-2. *Oceanog*, **32**, 50–57, https://doi.org/10/gncz84.

Rutledge, S. A., V. Chandrasekar, B. Fuchs, J. George, F. Junyent, B. Dolan, P. C. Kennedy, and K. Drushka, 2019b: SEA-POL Goes to Sea. *Bulletin of the American Meteorological Society*, **100**, 2285–2301, https://doi.org/10/gncz83.

S. Lee, J. Moon, B. Wang, and H. Kim, 2017: Subseasonal prediction of extreme precipitation over Asia: Boreal summer intraseasonal oscillation perspective. *J. Climate*, **30**, 2849–2865, https://doi.org/10.1175/JCLI-D-16-0206.1.

S. W. Nesbitt, R. Cifelli, and S. A. Rutledge, 2006: Storm morphology and rainfall characteristics of TRMM precipitation features. *Mon. Wea. Rev.*, **134**, 2702–2721, https://doi.org/10.1175/MWR3200.1.

Schumacher, C., and R. A. Houze, 2000: Comparison of Radar Data from the TRMM Satellite and Kwajalein Oceanic Validation Site. *J. Appl. Meteor.*, **39**, 2151–2164, https://doi.org/10/cnwfsb.

——, M. H. Zhang, and P. E. Ciesielski, 2007: Heating Structures of the TRMM Field Campaigns. *Journal of the Atmospheric Sciences*, **64**, 2593–2610, https://doi.org/10/cf27g6.

Seliga, T. A., and V. N. Bringi, 1976: Potential Use of Radar Differential Reflectivity Measurements at Orthogonal Polarizations for Measuring Precipitation. *J. Appl. Meteor.*, **15**, 69–76, https://doi.org/10/d5842v.

——, K. Aydin, and H. Direskeneli, 1986: Disdrometer Measurements during an Intense Rainfall Event in Central Illinois: Implications for Differential Reflectivity Radar Observations. *J. Climate Appl. Meteor.*, **25**, 835–846, https://doi.org/10/fc5hc9.

Simpson, J., C. Kummerow, W.-K. Tao, and R. F. Adler, 1996: On the Tropical Rainfall Measuring Mission (TRMM). *Meteorl. Atmos. Phys.*, **60**, 19–36, https://doi.org/10/cjsp6q.

Skofronick-Jackson, G., and Coauthors, 2017: The Global Precipitation Measurement (GPM) Mission for Science and Society. *Bulletin of the American Meteorological Society*, **98**, 1679–1695, https://doi.org/10/ghzmf2.

Slingo, A., 1990: Sensitivity of the Earth's radiation budget to changes in low clouds. *Nature*, **343**, 49–51, https://doi.org/10/bjkp9p.

Sobel, A. H., J. Sprintall, E. D. Maloney, Z. K. Martin, S. Wang, S. P. de Szoeke, B. C. Trabing, and S. A. Rutledge, 2021: Large-scale state and evolution of the atmosphere and ocean during PISTON 2018. *Journal of Climate*, 1–59, https://doi.org/10/gncz85.

Speirs, P., M. Gabella, and A. Berne, 2017: A Comparison between the GPM Dual-Frequency Precipitation Radar and Ground-Based Radar Precipitation Rate Estimates in the Swiss Alps and Plateau. *Journal of Hydrometeorology*, **18**, 1247–1269, https://doi.org/10/gbqqmm.

Steiner, M., R. A. Houze, and S. E. Yuter, 1995: Climatological Characterization of Three-Dimensional Storm Structure from Operational Radar and Rain Gauge Data. *J. Appl. Meteor.*, **34**, 1978–2007, https://doi.org/10/d96zc8.

Stephens, G. L., and Coauthors, 2002: THE CLOUDSAT MISSION AND THE A-TRAIN: A New Dimension of Space-Based Observations of Clouds and Precipitation. *Bull. Amer. Meteor. Soc.*, **83**, 1771–1790, https://doi.org/10/ff47jf.

Stolz, D. C., S. A. Rutledge, J. R. Pierce, and S. C. Heever, 2017: A global lightning parameterization based on statistical relationships among environmental factors, aerosols, and convective clouds in the TRMM climatology. *J. Geophys. Res. Atmos.*, **122**, 7461–7492, https://doi.org/10/ghtspd.

Szumowski, M. J., R. M. Rauber, H. T. Ochs, and L. J. Miller, 1997: The Microphysical Structure and Evolution of Hawaiian Rainband Clouds. Part I: Radar Observations of Rainbands Containing High Reflectivity Cores. *J. Atmos. Sci.*, **54**, 369–385, https://doi.org/10/bh652s.

——, ——, ——, and K. V. Beard, 1998: The Microphysical Structure and Evolution of Hawaiian Rainband Clouds. Part II: Aircraft Measurements within Rainbands Containing High Reflectivity Cores. *J. Atmos. Sci.*, **55**, 208–226, https://doi.org/10/b5kbfz.

——, ——, and ——, 1999: The Microphysical Structure and Evolution of Hawaiian Rainband Clouds. Part III: A Test of the Ultragiant Nuclei Hypothesis. *J. Atmos. Sci.*, **56**, 1980–2003, https://doi.org/10/c8hxzb.

T. J. Dunkerton, M. Montgomery, and Z. Wang, 2009: Tropical cyclogenesis in a tropical wave critical layer: Easterly waves. *Atmos. Chem. Phys.*, **9**, 5587–5646, https://doi.org/10.5194/acp-9-5587-2009.

T. J. Lang, D. A. Ahijevych, S. W. Nesbitt, R. E. Carbone, S. A. Rutledge, and R. Cifelli, 2007: Radar-observed characteristics of precipitating systems during NAME 2004. *J. Climate*, **20**, 1713–1733, https://doi.org/10.1175/JCLI4082.1.

T. M. Rickenbach and S. A. Rutledge, 1998: Convection in TOGA COARE: Horizontal scale, morphology, and rainfall production. *J. Atmos. Sci.*, **55**, 2715–2729, https://doi.org/10.1175/1520-0469(1998)055<2715:CITCHS>2.0.CO;2.

Tagawa, T., H. Hanado, K. Okamoto, and T. Kozu, 2007: Suppression of Surface Clutter Interference With Precipitation Measurements by Spaceborne Precipitation Radar. *IEEE Trans. Geosci. Remote Sensing*, **45**, 1324–1331, https://doi.org/10/cmn732.

Takahashi, N., H. Hanado, and T. Iguchi, 2006: Estimation of Path-Integrated Attenuation and Its Nonuniformity From TRMM/PR Range Profile Data. *IEEE Trans. Geosci. Remote Sensing*, **44**, 3276–3283, https://doi.org/10/cxn982.

Takahashi, T., K. Suzuki, M. Orita, M. Tokuno, and R. de la Mar, 1995: Videosonde Observations of Precipitation Processes in Equatorial Cloud Clusters. *Journal of the Meteorological Society of Japan*, **73**, 509–534, https://doi.org/10/gnc2f7.

Thompson, E. J., S. A. Rutledge, B. Dolan, and M. Thurai, 2015: Drop Size Distributions and Radar Observations of Convective and Stratiform Rain over the Equatorial Indian and West Pacific Oceans. *Journal of the Atmospheric Sciences*, **72**, 4091–4125, https://doi.org/10/gnc2gq.

——, ——, ——, ——, and V. Chandrasekar, 2018: Dual-Polarization Radar Rainfall Estimation over Tropical Oceans. *Journal of Applied Meteorology and Climatology*, **57**, 755–775, https://doi.org/10/gdbqtk.

Thurai, M., G. J. Huang, V. N. Bringi, W. L. Randeu, and M. Schönhuber, 2007: Drop Shapes, Model Comparisons, and Calculations of Polarimetric Radar Parameters in Rain. *J. Atmos. Oceanic Technol.*, **24**, 1019–1032, https://doi.org/10/cgz9n3.

——, V. N. Bringi, and P. T. May, 2010: CPOL Radar-Derived Drop Size Distribution Statistics of Stratiform and Convective Rain for Two Regimes in Darwin, Australia. *Journal of Atmospheric and Oceanic Technology*, **27**, 932–942, https://doi.org/10/bwbw4g.

Tokay, A., L. P. D'Adderio, F. Porcù, D. B. Wolff, and W. A. Petersen, 2017: A Field Study of Footprint-Scale Variability of Raindrop Size Distribution. *Journal of Hydrometeorology*, **18**, 3165–3179, https://doi.org/10/gdgtd8.

Ulbrich, C. W., and D. Atlas, 2007: Microphysics of Raindrop Size Spectra: Tropical Continental and Maritime Storms. *Journal of Applied Meteorology and Climatology*, **46**, 1777–1791, https://doi.org/10/ftb9dr.

W. Tao, S. Lang, X. Zeng, S. Shige, and Y. Takayabu, 2010: Relating convective and stratiform rain to latent heating. *J. Climate*, **23**, 1874–1893, https://doi.org/10.1175/2009JCLI3278.1.

W. Xu and S. A. Rutledge, 2015: Morphology, intensity, and rainfall production of MJO convection: Observations from DYNAMO shipborne radar and TRMM. *J. Atmos. Sci.*, **72**, 623–640, https://doi.org/10.1175/JAS-D-14-0130.1.

—— and ——, 2016: Time scales of shallow-to-deep convective transition associated with the onset of Madden–Julian oscillations. *Geophys. Res. Lett.*, **43**, 2880–2888, https://doi.org/10.1002/2016GL068269.

—— and ——, 2018: Convective variability associated with the boreal summer intraseasonal oscillation in the South China Sea region. *J. Climate*, **31**, 7363–7383, https://doi.org/10.1175/JCLI-D-18-0091.1.

Wang, J., and D. B. Wolff, 2009: Comparisons of Reflectivities from the TRMM Precipitation Radar and Ground-Based Radars. *Journal of Atmospheric and Oceanic Technology*, **26**, 857–875, https://doi.org/10/bgksjr.

Wang, Y., and V. Chandrasekar, 2009: Algorithm for Estimation of the Specific Differential Phase. *Journal of Atmospheric and Oceanic Technology*, **26**, 2565–2578, https://doi.org/10/bc8dqf.

Watters, D., A. Battaglia, K. Mroz, and F. Tridon, 2018: Validation of the GPM Version-5 Surface Rainfall Products over Great Britain and Ireland. *Journal of Hydrometeorology*, **19**, 1617–1636, https://doi.org/10/gfhv3k.

Woodcock, A. H., 1953: SALT NUCLEI IN MARINE AIR AS A FUNCTION OF ALTITUDE AND WIND FORCE. *J. Meteor.*, **10**, 362–371, https://doi.org/10/bqfqms.

X. Wang and M. Zhang, 2015: The coupling of mixed Rossby-gravity waves with diabatic heating during the TRMM-KWAJEX field campaign. *Geophys. Res. Lett.*, **42**, 8241–8249, https://doi.org/10.1002/2015GL065813.

Xu, W., and S. A. Rutledge, 2015: Morphology, Intensity, and Rainfall Production of MJO Convection: Observations from DYNAMO Shipborne Radar and TRMM. *Journal of the Atmospheric Sciences*, **72**, 623–640, https://doi.org/10/f6zw7k.

Y. L. Serra, G. N. Kiladis, and M. F. Cronin, 2008: Horizontal and vertical structure of easterly waves in the Pacific ITCZ. *J. Atmos. Sci.*, **65**, 1266–1284, https://doi.org/10.1175/2007JAS2341.1.

Y. Wang and V. Chandrasekar, 2009: Algorithm for estimation of the specific differential phase. *J. Atmos. Oceanic Technol.*, **26**, 2565–2578, https://doi.org/10.1175/2009JTECHA1358.1.

Yau, M. K., R. R. Rogers, TotalBoox, and TBX, 1996: *A Short Course in Cloud Physics.* Elsevier Science,.

Zrnić, D. S., T. D. Keenan, L. D. Carey, and P. May, 2000: Sensitivity Analysis of Polarimetric Variables at a 5-cm Wavelength in Rain. *J. Appl. Meteor.*, **39**, 1514–1526, https://doi.org/10/cmrz9g.

Warm rain - Glossary of Meteorology. https://glossary.ametsoc.org/wiki/Warm_rain (Accessed November 9, 2021).